GENTLE PHOTOIONIZATION OF ORGANIC CONSTITUENTS USING VACUUM ULTRAVIOLET AEROSOL MASS SPECTROMETRY

Erin R. Mysak

A dissertation submitted to the University of North Carolina at Chapel Hill in partial fulfillment of the requirements for the degree of Doctor of Philosophy in the Department of Chemistry.

Chapel Hill
2006

Advisor: Tomas Baer

Reader: James Jorgenson

Reader: Gary Glish

ABSTRACT

Erin R. Mysak
Gentle photoionization of organic constituents using vacuum ultraviolet aerosol mass spectrometry
(Under the direction of Tomas Baer)

Aerosol particles have long been a primary focus of the atmospheric community due to their influence on human health, radiative forcing, and participation in atmospheric chemistry. Conventionally, aerosols have been collected on filters and analyzed off-line by GC-MS, LC-MS, and FTIR. These techniques made valuable inroads to particle speciation, however, the inherent physical and chemical artifacts during sampling initiated the development of a succession of on-line aerosol mass spectrometers. Currently, a variety of real-time aerosol mass spectrometers, many with single particle analysis capabilities, have been developed and installed in laboratories as well as in the field. Atmospheric aerosols are complex mixtures of inorganic and organic species, and whereas analysis of inorganics is rather straightforward due to their robust nature, organics are fragile and analysis is challenging. Several researchers have moved specifically towards analysis of organic aerosol particles, attempting to simplify peak assignment by reducing the fragmentation of these delicate molecules.

The initial portion of this project involved design and development of an aerosol mass spectrometer, ideal for analyzing a wide size range of organic aerosol particles. The novel mass spectrometer uses both continuous vaporization with a cartridge heater and quasi-

continuous photoionization by tunable vacuum ultraviolet light produced by synchrotron radiation. Coupling continuous vaporization and ionization techniques with a high brightness photon source allows analysis of ultrafine aerosol particles, which have high toxicity and high number concentration in ambient air. Several atmospherically relevant organic molecules are examined, along with a more complex yet more realistic secondary organic aerosols formed from terpene ozonolysis. Finally, a timing circuit used to analyze single particles (diameter > 200nm) was designed and developed. The versatile electronic circuit can be used to couple multi-laser systems having pre-triggering requirements to single particle arrival in the ionization region of the mass spectrometer. It can also be applied to continuous vaporization and ionization schemes where one wants to pulse ions into a time of flight analyzer as particles arrive in the interaction region.

ACKNOWLEDGEMENTS

I thank Dr. Tomas Baer for being the teacher I would wish to be. I am indebted to many for their knowledge, skill and willingness to share; postdoctoral students Dr. Ephraim Woods, Dr. Geoff Smith, Dr. X. Frank Liu, Dr. Hideya Koizumi, and Dr. Michael Tolocka, visiting scientists Dr. Bálint Sztáray and Juci Sztáray, the Chemical Dynamics Beamline personnel at Lawrence Berkeley National Laboratory Dr. Kevin Wilson, Dr. Musa Ahmed, Dr. Eric Gloaguen, Michael Jimenez-Cruz, Dr. Darcy Peterka, Dr. Christophe Nicholas, and Dr. Steve Leone, and finally to my fellow graduate students, especially Dr. Yury Dessiaterik. I gratefully acknowledge insightful discussions with Dr. Rich Kamens, Dr. Paul Ziemann, and Dr. Roger Miller.

TABLE OF CONTENTS

LIST OF TABLES

LIST OF FIGURES

LIST OF ABBREVIATIONS

AE	Appearance Energy
AMS	Aerosol Mass Spectrometer
APCIMS	Atmospheric Pressure Chemical Ionization Mass Spectrometry
ATOFMS	Aerosol Time-of-Flight Mass Spectrometry
CI	Chemical Ionization
DMA	Differential Mobility Analyzer
D_p	Particle Diameter
ECI	Excited Crigee Intermediate
EI	Electron Impact
eV	Electron Volts
EPA	Environmental Protection Agency
ESI	Electrospray Ionization
FTIR	Fourier Transform Infra Red Spectroscopy
GC-MS	Gas Chromatography-Mass Spectrometry
GMD	Geometric Mean Diamter
HPLC	High Performance Liquid Chromatography
IE	Ionization Energy
MALDI	Matrix Assisted Laser Desorption Ionization
MCP	Multichannel Plates
MS	Mass Spectrometry
MS-MS	Tandem Mass Spectrometer
NAMS	Nano-aerosol Mass Spectrometer

DMA	Differential Mobility Analyzer
NDMA	Nano Differential Mobility Analyzer
Nd:YAG	Neodymium Yttrium Aluminum Garnet
PERCI	Photoelectron Resonance Capture Ionization
PIAMS	Photoionization Aerosol Mass Spectrometer
PIE	Photoionization Efficiency
PM	Particulate Matter
PM_{10}	Particulate Matter under 10mm
$PM_{2.5}$	Particulate Matter under 2.5mm
ppm	Parts per million
ppt	Parts per thousand
QIT	Quadrupole Ion Trap
RETOF	Reflectron Time of Flight
RH	Relative Humidity
SCI	Stabilized Crigee Intermediate
SNR	Signal to Noise Ratio
SOA	Secondary Organic Aerosol
SR	Synchrotron
TgC	Teragrams Carbon
TPTD	Temperature Programmed Thermal Desorption
TOF	Time of Flight
t_{rxn}	Reaction time
VOC	Volatile Organic Compound

VUV	Vacuum Ultraviolet
VUV-AMS	Vacuum Ultraviolet Aerosol Mass Spectrometer

CHAPTER 1:

Introduction

1.1. Motivation for the study of aerosols

Aerosols are increasingly recognized as a crucial area of research as their local, regional, and global impacts become more thoroughly understood. Locally, aerosol particles emitted from such sources as wood burning fires, industrial processes, and vehicular emissions, lead directly to urban air pollution[1,2] and can have negative effects on human health.[3-5] Regional impacts are seen in remote locations that have no significant sources of aerosols since particles can be easily transported over long distances in the atmosphere. Globally, airborne particulate matter are known for affecting climate change and participate in heterogeneous chemistry in both the troposphere and stratosphere, leading to deleterious effects such as destruction of stratospheric ozone.

By definition, an aerosol is any type of particulate matter (PM), either a liquid or solid, suspended in a gas. Aerosols can originate from a variety of anthropogenic as well as biogenic sources and are often in the form of wind-blown sea salt, volcanic ash, dust storms, pollen, fog, smoke, smog or car exhaust. As a means of comparing and measuring aerosol particles, they are often characterized by their physical properties such as their mass concentration, size distribution, and number concentration. Number concentrations of aerosol particles range from 30 particles cm^{-3} in the free troposphere to more than 10^5 particles cm^{-3} in urban regions,[1] while particle diameters range from 2 – 20,000 nm. The

corresponding mass concentrations, which are a function of both diameter and number, can consequently have a significant degree of variation.

Depending on the chemical composition of the particles, they can influence a variety of tangible parameters, such as adverse health symptoms and an increase in acidic precipitation. For these reasons, it is important to accurately measure and consider effects of a variety of aerosol properties. In addition, these chemical and physical measurements yield clues to their origins, which is a crucial factor for effective regulation of anthropogenic sources. Furthermore, these measurements are essential for understanding the processes and factors that lead to biogenic aerosol production. For a multitude of reasons including those discussed above, instruments capable of studying the physical and chemical properties of aerosol particles are fundamentally important for increasing our understanding of aerosol science. This chapter presents the principal motivations for investigating atmospherically relevant chemical species and the fundamental aspects of the real-time instruments that measure them.

1.1.1. Ambient particle sizes

In urban areas, particles are classified into three different size ranges. The smallest particles are termed the nuclei mode, followed by accumulation, and coarse for the largest diameter.[1,2,6] Particles in each of the three modes are formed by very different processes. Thus chemical composition of the particles can be broadly correlated with their size range.

The nuclei mode ranges from approximately 2-50 nm diameter and peaks in number concentration around 10nm (Figure 1.1).[6] Although this mode has by far the highest number concentration of the three modes, it has the lowest volume concentration (Figure 1.1), as

volume is proportional to diameter cubed. These particles are typically formed from combustion (soot) and from gas to particle conversion of SO_x, NO_x, volatile organic compounds (VOC), and

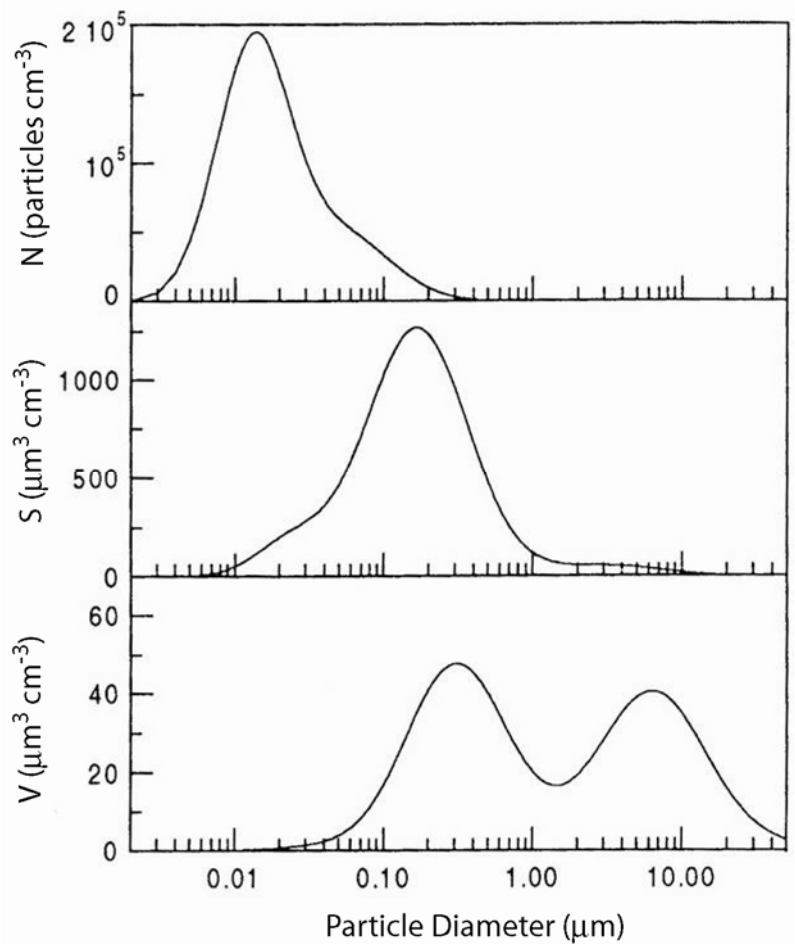

Figure 13.1. A typical urban aerosol profile; (V) volume, (S) surface area, and (N) number concentration as a function of particle diameter. [2]

ammonia emissions. They are found specifically at the site of their origination; usually in urban areas, around highways and power plants. This mode is not typically present in other locations other than immediately surrounding the source because as these particles are generated in high number concentrations they tend to rapidly coagulate with one another or with pre-existing particles in the accumulation mode. Alternatively, nuclei mode particles

can grow in size by the condensation of surrounding vaporous constituents. Regardless of how they evolve, they rapidly transform into accumulation size range particles.

The accumulation mode not only includes nuclei mode particles that have coagulated, but also includes smog particles and particles generated by combustion. Removal mechanisms are slow because accumulation mode particles are too small to settle by gravity and are too large to coagulate by diffusion.[6] As a result, accumulation mode particles persist, or accumulate, over long periods of time. When compared to the other two size modes, this mode not only has a high volume concentration, but is also characterized by a large surface area concentration (Figure 1.1). This size mode extends from 50 nm – 1 μm in diameter but typically has the greatest volume and surface area concentrations around 200 nm.

Coarse particles are comprised mostly of biogenic debris such as soil, windblown dust, and sea salt particles generated by wave action, and anthropogenic dust created by processes such as farming, mining, and driving on dusty roads. Their size range extends from 1 – 20 μm in diameter, peaking in number concentration at around 6 μm and in mass concentration at about 10 μm diameter. The total number of particles in this size range is much lower than in the nuclei and accumulation modes because these larger diameter particles rapidly settle out of the atmosphere due to gravity. The mass concentration of this mode, however, is comparable to that of the accumulation mode.

Together, the nuclei and accumulation modes are referred to as 'fine particles'. Because of the combined large total mass and surface area of fine particles, these particles have a disproportionately large effect on not only atmospheric processes, but also on human health.[1-4,7]

1.1.2. Health effects

Elevated levels of particulate matter have been correlated with respiratory disease,[4,8,9] increased mortality,[3-5,7] and decreased pulmonary function.[8]. Because of their ability to affect human health, fine particulate matter has been regulated since 1987 by the US Environmental Protection Agency (USEPA) when a significant amendment was added to the pre-existing Clean Air Act. This amendment included National Ambient Air Quality Standards, one of its most notable standards being that the maximum exposure of PM_{10}, or PM composed of particles having diameters less than 10 μm, was regulated at 50 μg m^{-3} (maximum annual average exposure concentration). In the decade after 1987, many studies were performed on health related consequences of PM. As a result of the increased awareness that specifically fine particles have an enhanced ability to enter into the human respiratory system and negatively affect health, a second standard was instituted in 1997 for PM with diameters less than 2.5 μm, $PM_{2.5}$(15 μg m^{-3}). The belief is that fine particles are able to pass through the upper respiratory filtration system and deposit directly into the lung's alveoli. Once in the lungs, the chemical content of these particles is absorbed into the blood stream, spreading potentially toxic and carcinogenic chemicals quite effectively through the human body. One highly noted study commonly referred to as 'the six city study', related a 1.5 % increased in mortality rates to 10 μg m^{-3} increase in $PM_{2.5}$ concentration.[5] In Figure 1.2, a clear correlation between fine particle concentration and mortality rates is seen. In addition, particles containing sulfate showed a clear relationship with increased mortality, although the two influences could not be distinguished because sulfate is rather ubiquitous in aerosol particles.[10]

Many new epidemiological and toxicological studies have focused on the health implications of long term exposure to fine PM and found correlations to elevated levels of infant, cardiovascular, and total mortality rates. In addition, links have been established between PM and morbidity including lung development, respiratory symptoms, and immune system function.[3,4,7] Furthermore, there is concern that the current $PM_{2.5}$ regulation does not consider the variability of the chemical contents of the PM on human health. The EPA has made efforts to examine the various epidemiological effects of pulmonary deposition of PM, and has proposed several different possible explanations for the resulting cardiac and respiratory effects. Not only may epithelial cells be damaged and lead to the observed cardiac and respiratory health effects, but sensory nerves and extrapulminary tissues such as the heart, liver, and bone marrow can also potentially contribute to the observed effects. [7,11] As the role of chemical content of PM is still not directly correlated to toxicity, additional studies are necessary not only to understand the role of content on health but also on being able to determine the chemical content of the species in ambient air.

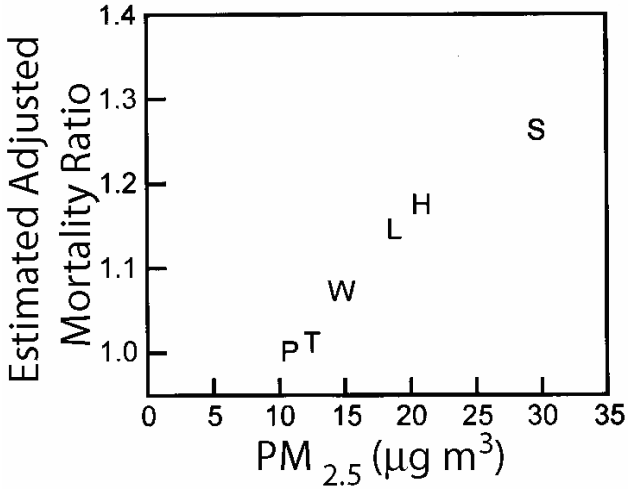

Figure 1.2. A benchmark study commonly referred to as the six city study correlated an increase in PM2.5 to increased mortality ratios. The six cities represented in the above plot are Portage, Wisconsin (P); Topeka, Kansas (T); Watertown, Massachusetts (W); St. Louis, Missouri (L); Kingston/Harriman, Tennessee (H); and Steubenville, Ohio (H).[5]

1.1.3. Radiative forcing of aerosols

Particles in this $PM_{2.5}$ size range not only impact human health,[3,4,7] but also the visibility of local regions[2,12] and global climate change by means of radiative forcing[13] (Figure 1.3). Fine particles are believed to influence the climate directly through earth's radiative balance due to their light scattering properties, known as direct radiative forcing. Additionally, aerosols cause indirect radiative forcing (for example by acting as cloud condensation nuclei) through their chemical or physical morphology.

The direct radiative forcing by aerosols is related to their optical, light scattering, and absorptive properties, which in turn is related to their physical and chemical properties. Since the wavelengths of light incident on the earth's atmosphere are similar in magnitude to the diameter of ambient aerosol particles, Mie scattering is important to the direct radiative forcing by aerosols. As shown by the Mie scattering plot in Figure 1.4, particle size plays an important role in the complex pattern of light scattering of aerosols. The particle scattering coefficients are proportional to particle diameter and indirectly proportional to the wavelength of incident light.

Whereas the effect of greenhouse gases on radiative forcing is relatively well understood, the effects aerosols have on direct radiative forcing are much less known. It is accepted that greenhouse gases such as CO_2 and O_3 have increased since the industrial revolution, and their buildup in the atmosphere has resulted in a net change in the absorbed energy from the sun of +1.25 W m^{-2} (measured net flux at the top of the atmosphere).[1] As early as 1992, it was proposed that aerosols have a net cooling effect on the earth's surface.[12] This phenomenon was later termed the 'whitehouse effect' because of its opposite effect of greenhouse gases. This cooling effect is estimated by Schwartz to be between 20-100%

opposite the magnitude of the greenhouse effect.[14] Research on the radiative forcing of aerosols is increasingly active as scientists continue to quantify and reduce uncertainty in predictions of the affects of aerosols on climate change.[13,15-18] It is crucial that radiative forcing by atmospheric aerosols be incorporated into global models analyzing global climate change, and the exclusion of this factor may lead to over-predictions of global warming.[2]

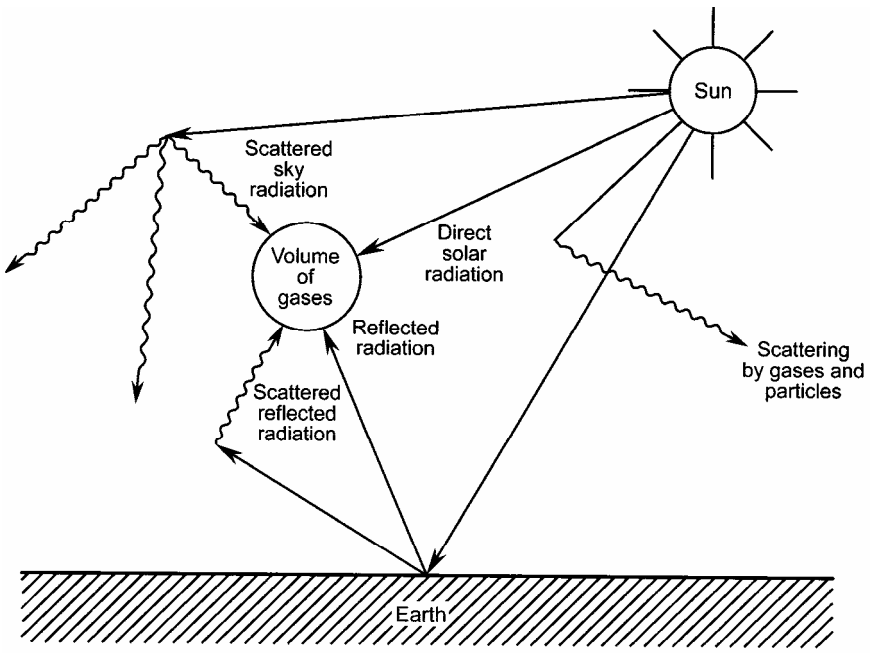

Figure 1.3. Radiative forcing due to various atmospheric pollutants including gases and aerosol particles. Whereas the effect of greenhouse gases on radiative forcing is well understood, the effect of aerosols is still largely uncertain.[1]

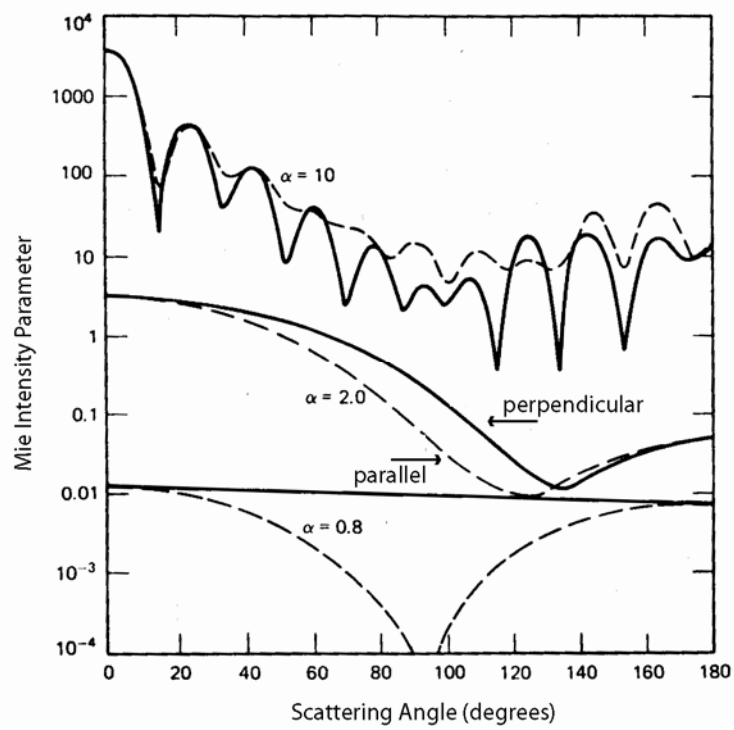

Figure 1.4. As the wavelength of incident light becomes similar in magnitude to particle diameter, the scattering parameter (Mie intensity parameter) varies according to Mie theory. In the above plot, α is directly proportional to particle diameter and indirectly proportional to the wavelength of incident light. This plot illustrates that the particle represented by the largest α scatters orders of magnitude more than a smaller diameter particle. Also, a smaller particle primarily scatters light in the forward direction, and backscatters a smaller amount of light.[6]

Though the warming effect of greenhouse gases is broadly accepted, the values of the both direct and indirect radiative forcing of aerosols are difficult to determine because PM is typically complex in its compositional makeup. The contribution of some pure particles to radiative forcing has been predicted with high confidence. For example, particles composed of sulfate scatter light efficiently and contribute between -0.3 to -1.8 W/m^2 by direct forcing. In contrast, elemental carbon (a common byproduct of fossil fuel burning) is an efficient light absorber and therefore traps energy resulting in between +0.27 and +0.54 W/m^2.[2] Mixed particles pose a far greater challenge. Estimates for organic PM range from -0.04 to -0.4 W/m^2[2] with uncertainties due to the fact that organic particles are usually complex mixtures of unknown quantities of inorganics, elemental carbon, and a variety of organics.

Aerosols affect the climate by indirect forcing as well, most notably by changing cloud properties. Often, aerosols act as cloud condensation nuclei (CCN) thereby increasing cloud reflectivity. It is notable, however, that tropospheric aerosols responsible for the whitehouse effect have lifetimes of about a week whereas greenhouses gases subsist for decades.[6]

1.1.4. Secondary organic aerosols (SOA)

Volatile organic compounds (VOC) are released in quantities of approximately 1250 TgC $year^{-1}$ and originate from both biogenic and anthropogenic sources.[19-22] Biogenic sources alone are responsible for producing around 1150 TgC yr^{-1} of VOCs.[21] It has become evident in recent years that of all the biogenic sources, woods produce ~70 % of the total biogenic VOC's, or about 821 TgC yr^{-1}.[21] These VOC's include isoprene, monoterpenes, and other more or less reactive organic species. Reactions leading to oxidation of VOCs occur readily in the atmosphere, including attack by species such as OH and Cl radicals, O_3, and NO_3. As products form, they become more highly oxygenated, more polar and less volatile than their precursor molecules.[23] As a result, the products of VOC oxidation reactions may partition from the gas to particle phase and can either condense onto available nuclei (heterogeneous nucleation) or can self-nucleate (homogeneous nucleation). These species that partition into the particle phase produce what is known as secondary organic aerosols (SOA) and typically these particles accumulate in the fine particle size range, $PM_{2.5}$. The products of such reactions, for example α-pinene with O_3, are estimated to produce around 30 or more individual products containing many multifunctional groups.[23] Despite the estimation that biogenic SOAs contribute such a large percentage of the global particle load[13] and are a significant contributor to fine particulate matter, neither pathways of nucleation nor product identification are well understood or established. More recently,

information about SOA composition and formation mechanisms have been experimentally investigated with environmental chamber studies of VOC photooxidation reactions.[24-31] Experimental studies such as these have proved crucial to understanding and formulating models that can accurately describe the formation and fate of SOAs.

Initially, theory had been based solely on adsorption mechanisms that assume that the uptake of semi-volatile components was by pre-existing solid aerosol particles or solid-like surfaces. As opposed to SOA models that focused on adsorption, in the mid-1990's Pankow and Odum et al.[32-34]developed theoretical models of SOA formation that depended heavily on gas-particle partitioning theory. This theory recognizes that many atmospheric particles are liquid or have liquid-like surfaces and that the gas-phase species are absorbed or dissolved into the pre-existing particle instead of being simply adsorbed onto the surface. Partitioning theory explained why semi-volatile species could be distributed between gas and liquid phase without reaching the saturation vapor pressure. Many researchers have used the Seinfeld/Pankow theory to explain and model their results.[24,25,35-38] It is also currently believed that heterogeneous chemical reactions may occur between the gas and particle phase or after uptake of the condensing species by the particle.[25,37,39]

Aldehydes, in particular, seem prone to participate in further reactions in the particle phase once they partition into the particle.[25,37] Of these studies examining heterogeneous chemical reactions, notable work has been aimed at examining aldehydes reacting in acidic conditions to produce increased aerosol mass yields due to acid catalysis, and at examining acid catalysis of monomer subunits to form oligomeric species in acidic particles.[25,40-43]

Monoterpenes, cyclic alkenes with the molecular formula $C_{10}H_{16}$, are an important sub-class of biogenic VOCs contributing ~126 TgC yr^{-1} to atmospheric biogenic hydrocarbon

loading.[20] Monoterpenes are readily oxidized by OH and NO_3 radicals as well as by O_3. Although the oxidation rate constant with the OH radical is extremely fast, the ozone concentration is much larger and thus dominates the oxidation reactions. In addition, the products of the monoterpene ozonolysis are of particular interest because they tend to be less volatile and thus more readily partition into particle phase and form SOA.[44]

1.2. Aerosol measurement

Because of the atmospheric significance of organic aerosols (comprising between 10-70% of $PM_{2.5}$), it is of particular interest to measure their concentration and to determine their identity. However, several factors present major difficulties, including their high volatility, fragility, variation from particle to particle, and their potential to transform physically and chemically on a short timescale. Organic aerosols are formed either by homogeneous nucleation or condensation onto small nuclei and are believed to contribute significantly to cloud formation[45,46] and to have significant health effects.[47] Because of the difficulties in speciation of organic molecules, the organic content in aerosols is often reported simply as 'organic carbon'. This general categorization is often the case when organic aerosols are analyzed with mass spectrometry using energetic ionization techniques such as electron impact or laser desorption ionization.[41,48]

1.2.1. Traditional forms of aerosol measurement

Conventional aerosol analysis has generally been performed by off-line techniques in which aerosols are collected and accumulated over a period of time either with filtration, gravitational sedimentation, or inertial impaction.[48] Once collected, the bulk PM is analyzed for elemental and chemical information with a variety of analytical methods including ion chromatography, atomic absorption spectroscopy, atomic emission spectroscopy, and x-ray

fluorescence, etc. Transmission electron spectroscopy, x-ray fluorescence spectroscopy, and scanning electron microscopy, etc., are off-line techniques capable of single particles analysis.[48] By far, the most widely used technique for bulk aerosol analysis has been gas chromatography- mass spectrometry (GC-MS).[49,50] Although it has proved successful in organic speciation, GC-MS has several notable disadvantages.[49] Analysis is restricted to volatile and semi-volatile compounds because the sample must be analyzed in gaseous phase. The particle samples must often be heated at the inlet, causing thermal degradation of delicate organic species. Although conventional techniques such as GC-MS and High Performance Liquid Chromatography (HPLC) have made valuable inroads in organic PM speciation, the major disadvantage of off-line methods is the need for filter collection followed by liquid extraction of the sample. Not only can volatile components of the aerosols evaporate from the filter before analysis,[50] but the particles may also chemically interact with one another during collection. The chemical and physical artifacts inherent in filter collection techniques[50] prompted the design of a variety of real-time aerosol mass spectrometers.

1.2.2. Aerosol mass spectrometers

On-line aerosol mass spectrometers were originally developed in the 1970's as a means to identify the real-time chemical composition of a variety of atmospheric particles. This early research focused mainly on the development of instrumentation, which led to the creation of a real-time single particle mass spectrometry (RTSPMS). [51,52] Over the following 15 years, a maximum of only 5 research groups worldwide per year actively pursued RTSPMS.[48,53] However, interest in the aerosol mass spectrometry field significantly increased in the early 1990's, likely a result of the EPA's increased acknowledgement of the

negative health effects of PM and its increased regulation of PM_{10}. Since then, a variety of instruments have been customized for ionization and analysis of particular types of aerosols (soot, salts, or organics) and are now common both in the laboratory[54-62] and in the field.[41,63-66] Some of these instruments can yield both size and compositional data. In addition, two commercial instruments recently introduced into the market provide evidence for the widespread interest in aerosol measurement; Aerodyne's Aerosol Mass Spectrometer (AMS)[67,68] and TSI, Inc.'s Aerosol Time-of-Flight Mass Spectrometer (ATOFMS).[69] Many instrumentational reviews are available,[48,70-75] which outline the various components of aerosol mass spectrometers, including sample introduction, aerosol sizing scheme, vaporization and ionization method, and mass analysis technique. The variations in the instrumental designs permit optimal performance in several respects such as particle sizing, single particle versus ensemble particle information, quantification abilities, and ability for organic speciation.

1.2.2.1 Particle sizing techniques

Particle sizing methods vary primarily as a function of the size range of interest, the most prominent division being between diameters greater than or less than 100 nm. For particles large enough to scatter light (~200 for real particles and ~95 nm for latex particles),[69] laser light scattering may be used. After a particle passes through a laser beam, scattering photons are detected by a photomultiplier tube. The intensity of scattered light is directly related to the particle diameter.[76] However, several confounding factors are inherent in using this method. Particles of different materials/compositions will scatter light at different intensities because absorptivity varies according to composition. Secondly, the

scattering efficiency varies dramatically over the broad range of particle sizes of interest, the lowest diameter detectable particles being ~ 95 nm with a scattering efficiency of 0.5%.[69,77,78]

More accurate techniques relate particle velocity in vacuum to aerodynamic diameter.[54,79,80] These techniques make use of the fact that as a particle passes from ambient pressure through a commonly used aerodynamic lens system into a vacuum of approximately 10 mTorr, the particle reaches a terminal velocity that is directly related to the particle size.

This velocity is measured in one of two ways. One method, as used by the Aerodyne AMS (Figure 1.5c), utilizes a chopper wheel. A particle bunch passing through the chamber is timed starting as it enters through the chopper and ending as it creates signal at the ion detector.[81] The main advantage of this technique is that it can be applied to a broad range of particle sizes, even to large fluxes of particles too small to be detected with laser light scattering. The main disadvantage of the chopper is the low duty cycle (1.8%).[81]

The second method of determining particle velocity in-situ is by laser light scattering (Figure 1.5a and b). Light scattering from a single continuous laser can be detected with a photomultiplier, permitting the vaporization/ionization laser to be fired at some delay, intercepting the particle as it enters the ionization region.[77,78] This method allows the user to trigger on a single particle based on its flight time and can be used for various sizes of particles. Similarly, two light scattering pulses from a pair of continuous diode lasers can be used to determine particle velocity for low fluxes of large particles.[79,80,82] This velocity measurement can then be used to trigger an ablation/ionization laser as the particle reaches the ionization region. The technique is ideal for triggering lasers on both mono and polydisperse samples, and has the additional advantage of relating particle size and compositional information.

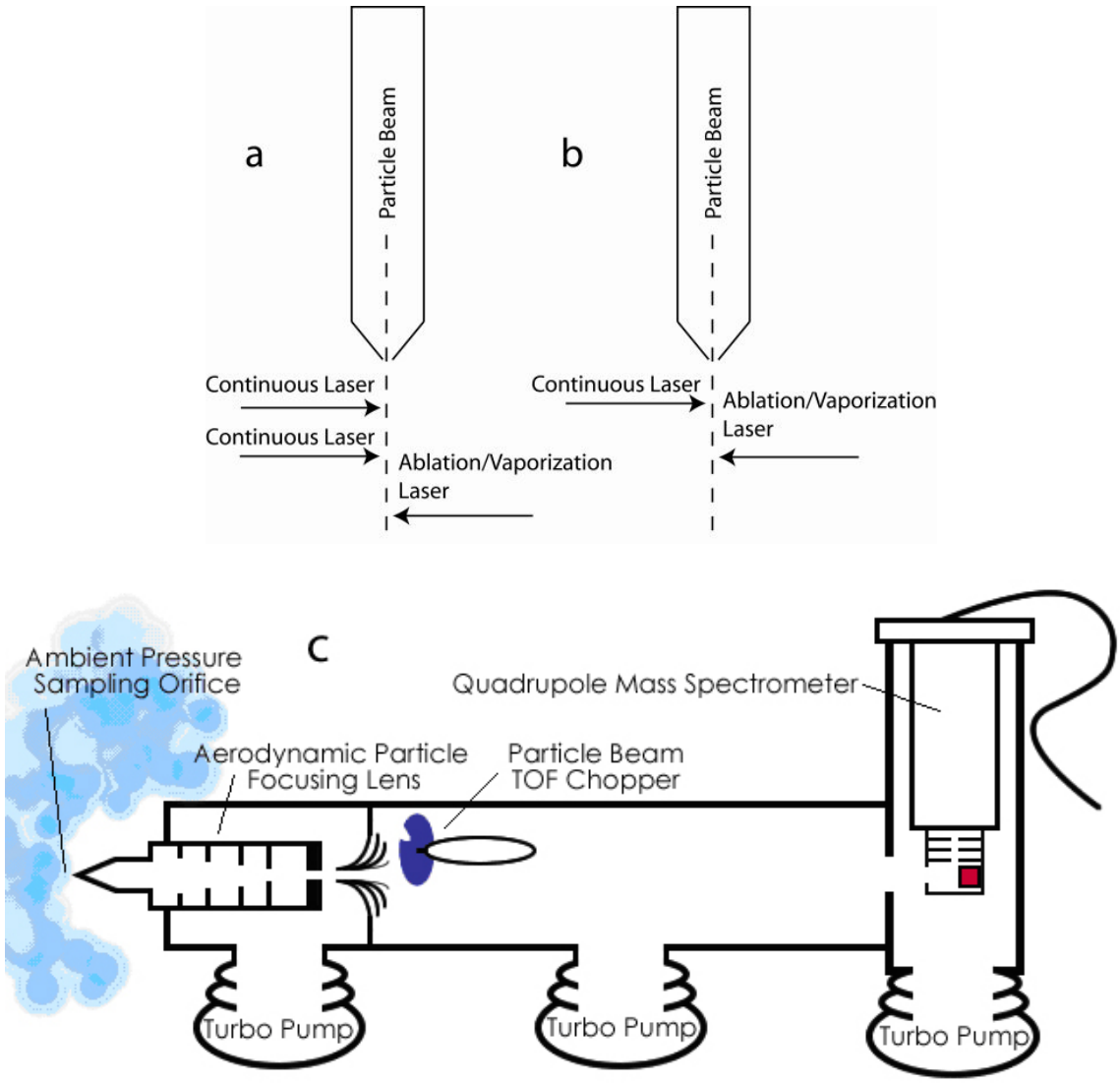

Figure 1.5. Particle sizing techniques of various aerosol mass spectrometers. **a)** Two light scattering measurements are used to determine particle terminal velocity, which is related to particle aerodynamic diameter.[54,79,80] **b)** A single light scattering laser detects particles at a given distance from the ionization region.[77,78] **c)** A chopper allows sizing of particles, using signal from time of flight as stop time.[81]

It is useful to be able to correlate aerosol size and compositional information, but difficult to do with small particles en vacuo. As previously mentioned, it is not feasible to detect small particles with laser light scattering and using the chopper yields too small of a duty cycle. In order to circumvent this problem, particles with diameters exceeding ~2 nm can be size selected with a Nano Differential Mobility Analyzer (NDMA). Those particles

exceeding ~7 nm can be size selected with a Long DMA (LDMA), both from TSI, Inc. In addition, the DMA in combination with a Condensation Particle Counter (CPC) can measure size distributions of polydisperse aerosols either created in laboratory conditions, or in ambient conditions in the field. Particle sizing is also useful to monitor particle growth as a function of reaction time due to condensation or in the case of homogeneous nucleation. [53,54,76,83]

To date, single particle composition in ambient sampling conditions has only been examined in terms of broad categories such as nitrate, sulfates, some heavy metals, and carbonaceous particles. The overwhelming majority of ambient PM in terms of number concentrations and surface area are fine and ultrafine particles. However, if compositional data is desired, the only option is to look at ensemble signal. This is because small particles have so few molecules per particle that, regardless of the detection efficiency, they produce inadequate numbers of ions per particle to be above the detection limits of any aerosol MS. For example, it is routine to analyze 1 μm diameter particles with a pulsed laser ionization scheme such as the one in our laboratory at the University of North Carolina at Chapel Hill. However, by decreasing the diameter to 10 nm, the size of a freshly nucleated particle from SOA reactions, the volume is decreased by six orders of magnitude. Ultrafine particles must either be collected on a cryogenically cooled tip for several minutes of sampling time[55,84] or must be analyzed on-line using a continuous ionization source such as electron impact, chemical ionization, [61,81] or synchrotron photoionization as described in Chapter 2.

1.2.2.2 Vaporization and ionization techniques

A major distinguishing characteristic of vaporization and ionization schemes among aerosol MS is pulsed versus continuous sources. The particle size range of interest usually

determines the best method; pulsed lasers can be used for vaporization and/or ionizations of low fluxes of larger particles (diameters of ~0.1 – 5 μm) whereas continuous sources are necessary for high fluxes of small particles (< 100 nm). The advantage of using pulsed lasers for large particles is that the high intensity and short pulsewidth (~ 5μs) beam can be triggered to fire as the particles fly through the ionization region. The main challenge of laser operation is the anticipation of random particle arrival in the ionization region, and to be able to satisfy the pre-triggering requirement of some lasers, such as the Nd:YAG laser which requires triggering 250 μs prior to laser output. Electronics such as the timing circuit described in Chapter 4 use particle velocity measurements (described previously in Section 1.2.2.1) to predict the arrival time of each particle in the ionization region. Typical operating frequencies of Nd:YAG lasers are 10 or 30 Hz, which is acceptable for low fluxes of particles, but does not combine well with continuous streams of smaller particles. It is revealing to compare the efficiencies of a pulsed 10 Hz Nd:YAG laser versus a continuous photoionization source having the same integrated flux of ~10^{11} photons s^{-1}. During the time that a particle traverses the photon beam (ca 10 μs), the pulsed source delivers 10^{10} photons whereas the continuous lamp produces only 10^6 photons.

Some of the first aerosol analysis methods for single particles used a ultraviolet (UV) laser, which combined ablation and ionization into a single step.[53,76,83] Single step laser desorption and ionization are ideal for analysis of stable ions such as salts, metal containing compounds, elemental carbon, sulfates, and nitrates. However, the high laser intensity required to ablate and ionize the particle unavoidably results in multi-photon absorption, which causes delicate organics to fragment significantly. Typical organic molecules have

ionization potentials in the range of 7-12 eV, which is in the vacuum ultraviolet wavelength range.

In an effort to circumvent the problem of extensive fragmentation of organic species during UV laser ablation/ ionization, Baer and Miller [80]separated the ablation and ionization steps. Prior to irradiating the sample with an ionization laser, they vaporized the particle with an IR laser by using either a CO_2 (fixed wavelength of 10.2 μm) or an Optical Parametric Oscillator laser (tunable around 4 μm).[59] By separating these two steps, the ionization laser required a relatively low intensity and, thus, fragmentation of organic species was reduced due to the elimination of multi-photon processes.

Several years later, the same laboratory improved their analyses of organic species by exchanging their UV ionization laser for a vacuum ultraviolet laser (VUV).[59] VUV is ideal for analysis of organic constituents because typical organics have ionization potentials between 7-12 eV, thereby allowing delicate ionization and reduced fragmentation. Reduced fragmentation allows for easier identification of species, and becomes especially crucial in particles of mixed composition. One of the most straightforward and most frequently used set-ups for VUV is third harmonic generation of the 355 nm output of a Nd:YAG laser.[59,85,86] Another option is the tunable four wave mixing scheme.[87] A more ideal photoionization source for organics would be an easily operable and widely tunable VUV source, a possibility not conceivable with the elaborate set-ups and limited wavelength ranges inherent in laser use. Tunability in the VUV wavelength range would allow the energy to be tuned to values just above the ionization threshold of various organic species in order to achieve a fragment-free spectrum. Furthermore, this ideal source would still maintain the high intensity and high brightness of a laser source. One such source is synchrotron radiation.

Another method for very gentle analysis of organic molecules has recently been explored by Petrucci and coworkers.[62,88,89] This technique, photoelectron resonance capture ionization (PERCI), uses low energy electron capture. A 10Hz UV laser is used to gently remove low energy electrons from Al metal that then extracts a hydrogen atom from the molecule of interest, leaving a relatively stable, closed shell ion.

It is possible to circumvent the large particle requirement of laser systems by looking at deposited particles. Johnston and co-workers[57] have examined non-size selected particles with diameters of less than 300 nm collected on a cooled tip in the ionization region. After sufficient sample mass has accrued, an IR laser such as a CO_2 flash vaporizes the deposited sample and a VUV laser ionizes the plume a few microseconds later.

Small particles have been somewhat elusive to study, owing to the difficulty of their detection by light scattering and to their small volume per particle; for example a single 50nm diameter particle has a volume well below the detection efficiency of any current instrument. Coupling a continuous ionization source such as electron impact or chemical ionization with a continuous ultrafine particle source offers an attractive alternative to aerosol collection or laser utilization. The most widely used continuous ionization source in aerosol mass spectrometry is electron impact (EI). One of the great benefits of EI ionization is that molecules have a predictable ionization cross-section, which is essentially proportional to the number of electrons in the molecule, making it a quantitative technique. The second advantage to this method is that, unlike methods such as photoionization, the fragmentation patterns of molecules are universal at the standardized energy of 70 eV for various instruments using EI. The extensive databases available to all EI users allow for speciation of certain marker molecules or species in ambient air, for example. These several advantages

have lead to the use of EI in the commercialized Aerodyne AMS instrument. Library databases are essential to the interpretation of EI data because the fragmentation is impossible to unravel otherwise. One organic species alone can have 100 peaks, thus a mixture of components is too complicated to interpret. Figure 1.6a shows an example of the fragmentation of an example organic species, octadecanoic acid, with EI (70 eV). EI can be successfully used to examine ultrafine particles, and has been implemented in studies of ambient samples.[41,63,64,68] Furthermore, it has been used in studies of fundamental processes such as changes in particle chemical composition over reaction time and reaction kinetics.[29-31,90-98]

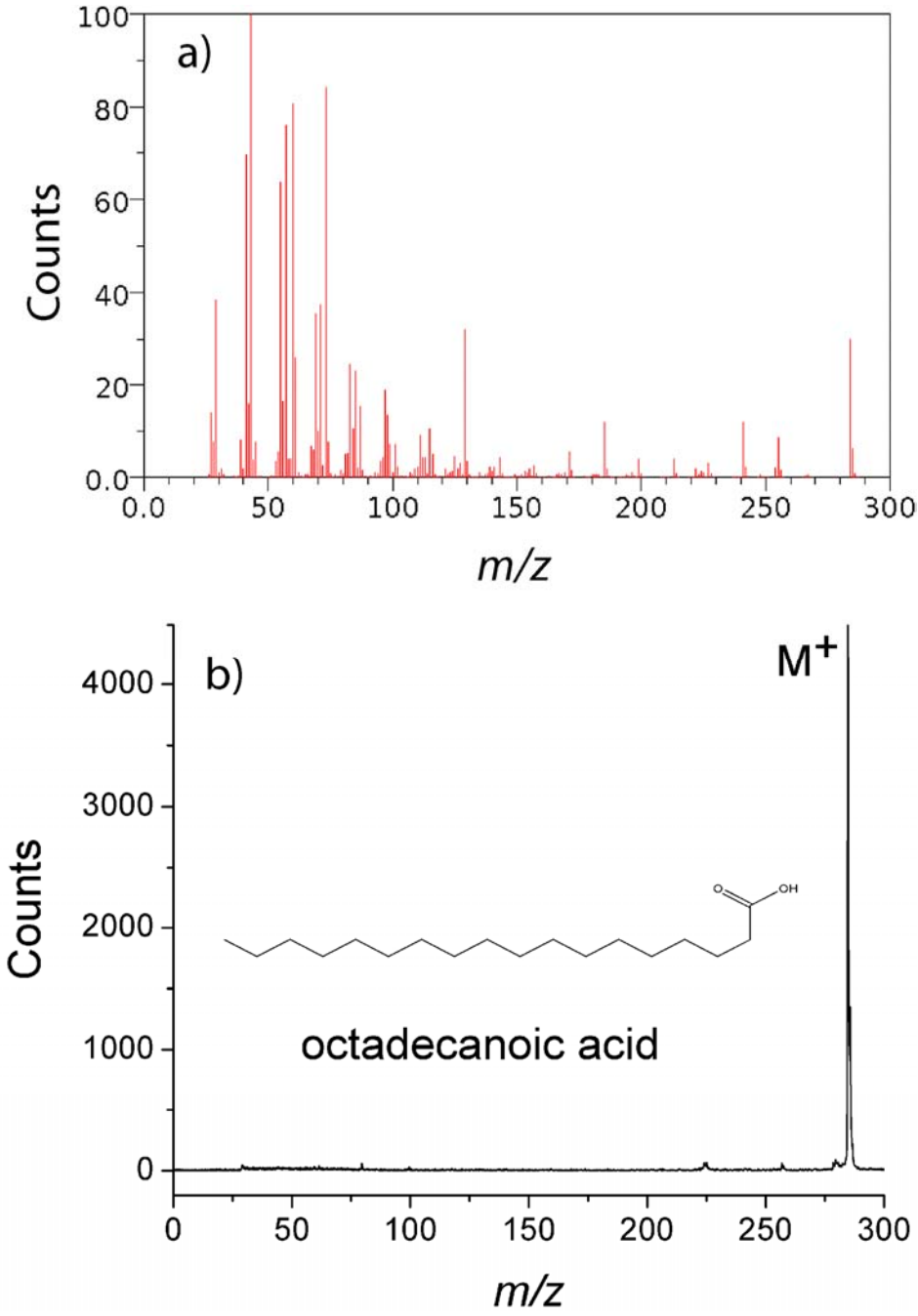

Figure 1.6. **a)** Electron impact (70 eV)[99] versus **b)** photoionization (10.5 eV) mass spectrum of octadecanoic acid, MW = 284 g mol^{-1}.

Chemical ionization (CI) is a gentler continuous technique that has also been successful in laboratory studies.[61,100,101] It has been useful in extracting kinetics and product information on model systems such as oleic acid ozonolysis.[102]

The final example of continuous ionization is by VUV photoionization, and as evidenced in Figure 1.6b (at 10.5 eV), it is a gentler technique than EI. It is not easy however, to achieve the flux necessary from a continuous VUV source for small particle analysis. High flux is a necessity for small particles since volume scales with the diameter cubed, and because VUV photoionization is not a very efficient process (average absorption cross section is 10^{-18} photons cm^{-2}). Chapters 2 and 3 will describe and demonstrate the utility of coupling for the first time, aerosol mass spectrometry of ultrafine particles with a continuous, easily tunable and high intensity VUV ionization source.

1.2.2.3 Mass analysis

The most common methods of mass analysis include time of flight, (TOF)[54,80,83], quadropole,[61,81] and quadropole ion trap (QIT).[58] The advantage of using a QIT is that tandem MS is possible, making it the only on-line aerosol two dimensional analysis tool. Organic species tend to fragment into similar m/z ions, and peak assignment could be simplified by additional molecular information. TOF analysis has been the most popular because it yields an entire mass spectrum with a single particle, whereas both the quadrupole and the QIT require scanning through a range of voltages. The two commercial instruments the ATOFMS and the AMS have employed the TOF and the quadrupole, respectively. A very new and greatly improved feature of the AMS is the use of an orthogonal RETOF, which yields such outstanding resolution that different molecules of the same nominal mass can be differentiated from one another.[67] For example, this ability is crucial to determining oxygen to carbon ratios from atmospheric samples, because it can determine the extent to which the products have been oxidized. The enhanced resolution of the orthogonal RETOF

would greatly improve the existing analysis methods for secondary aerosol analysis, as will be discussed in Chapter 3.

1.3 The current research

The focus of current research is on analysis of ultrafine organic particles. The limitations associated with using a pulsed laser system with small particles have forced us to find a continuous source, and the fragility of organic species has forced us to find a gentle form of ionization. The ideal source for this type of study is synchrotron radiation (SR), a widely tunable, high intensity, high brightness source.

The aerosol instrument featured in this manuscript was designed to be versatile towards various aerosol studies. This instrument was created in collaboration with the Chemical Dynamics Beamline at the Earnest Orlando Lawrence Berkeley National Laboratory (LBNL) and is located there at a user facility. Design considerations were made such that the instrument would be capable of probing various aspects of aerosol chemistry and physics including reaction kinetics, secondary aerosol formation, biologically relevant molecules, VUV light scattering, combustion aerosols, inorganic nanoparticles, and photoelectron imaging.

The numerous advantages of combining SR to ultrafine particle analysis will be discussed further in the flowing chapters. Aerosol MS performed with SR will be applied to studies of both pure organics aerosols (Chapter 2) and SOA systems (Chapter 3). Although we conclude that photoionization may not in fact be a perfect analysis tool for SOA systems, we were able to successfully extract new and hopefully valuable information from these studies. Chapter 4 focuses on an electrical timing circuit useful for single particle analysis.

In the current Chapel Hill laboratory set-up, the complex triggering requirements of the Nd:YAG laser (VUV source) must be coupled to random particle arrival events. In addition, this timing circuit can be used to rapidly pulse extract repeller plates in a TOF ionization region on random particle arrival events so that maximum ion signal is obtained. One such application would be for SR, where a quasi-continuous light source is combined with a high flux particle stream.

REFERENCES

1. Finlayson-Pitts, B. J.; Pitts, J. N. J. *Chemistry of the Upper and Lower Atmosphere*; Academic Press: San Diego, CA, 2000.

2. Seinfeld, J. H. P., Spyros N. *Atmospheric Chemistry and Physics: From Air Pollution to Climate Change*; John Wiley & Sone, Inc.: New York, 1998.

3. Gauderman, W. J. *New England Journal of Medicine* **2006**, *355*, 78-79.

4. Gauderman, W. J.; Avol, E.; Gilliland, F.; Vora, H.; Thomas, D.; Berhane, K.; McConnell, R.; Kuenzli, N.; Lurmann, F.; Rappaport, E.; Margolis, H.; Bates, D.; Peters, J. *New England Journal of Medicine* **2004**, *351*, 1057-1067.

5. Dockery, D. W.; Pope, C. A., 3rd; Xu, X.; Spengler, J. D.; Ware, J. H.; Fay, M. E.; Ferris, B. G., Jr.; Speizer, F. E. *The New England Journal of Medicine* **1993**, *329*, 1753-1759.

6. Hinds, W. C. *Aerosol Technology: Properties, Behavior, and Measurements of Airborne Particles, 2nd Edition*, 1998.

7. Kappos, A. D.; Bruckmann, P.; Eikmann, T.; Englert, N.; Heinrich, U.; Hoeppe, P.; Koch, E.; Krause, G. H. M.; Kreyling, W. G.; Rauchfuss, K.; Rombout, P.; Schulz-Klemp, V.; Thiel, W. R.; Wichmann, H. E. *International Journal of Hygiene and Environmental Health* **2004**, *207*, 399-407.

8. Pope, C. A., 3rd; Dockery, D. W.; Spengler, J. D.; Raizenne, M. E. *The American review of respiratory disease* **1991**, *144*, 668.

9. Dockery, D. W.; Speizer, F. E.; Stram, D. O.; Ware, J. H.; Spengler, J. D.; Ferris, B. G., Jr. *The American review of respiratory disease* **1989**, *139*, 587-594.

10. Xiong, J. Q.; Zhong, M.; Fang, C.; Chen, L. C.; Lippmann, M. *Environmental Science and Technology* **1998**, *32*, 3536-3541.

11. Englert, N. *Toxicology Letters* **2004**, *149*, 235-242.

12. Charlson, R. J.; Schwartz, S. E.; Hales, J. M.; Cess, R. D.; Coakley, J. A., Jr.; Hansen, J. E.; Hofmann, D. J. *Science (Washington, DC, United States)* **1992**, *255*, 423-430.

13. Yu, H.; Kaufman, Y. J.; Chin, M.; Feingold, G.; Remer, L. A.; Anderson, T. L.; Balkanski, Y.; Bellouin, N.; Boucher, O.; Christopher, S.; DeCola, P.; Kahn, R.; Koch, D.; Loeb, N.; Reddy, M. S.; Schulz, M.; Takemura, T.; Zhou, M. *Atmospheric Chemistry and Physics* **2006**, *6*, 613-666.

14. Schwartz, S. E. *Journal of Aerosol Science* **1996**, *27*, 359-382.

15. Remer, L. A.; Kaufman, Y. J. *Atmospheric Chemistry and Physics* **2006**, *6*, 237-253.

16. Pant, P.; Hegde, P.; Dumka, U. C.; Sagar, R.; Satheesh, S. K.; Moorthy, K. K. *Los Alamos National Laboratory, Preprint Archive, Physics* **2006**, 1-32, arXiv:physics/0603046.

17. Huang, Y.; Dickinson, R. E.; Chameides, W. L. *Proceedings of the National Academy of Sciences of the United States of America* **2006**, *103*, 4371-4376.

18. Bates TS, A. T., Baynard T, Bond T, Boucher O, Carmichael G, Clarke A, Erlick C, Guo H, Horowitz L, Howell S, Kulkarni S, Maring H, McComiskey A, Middlebrook A, Noone K, O'Dowd CD, Ogren J, Penner J, Quinn PK, Ravishankara AR, Savoie DL, Schwartz SE, Shinozuka Y, Tang Y, Weber RJ, Wu Y *Atmospheric Chemistry and Physics* **2006**, *6*, 1657-1732.

19. Moukhtar, S.; Couret, C.; Rouil, L.; Simon, V. *Science of the Total Environment* **2006**, *354*, 232-245.

20. Fuentes JD, L. M., Atkinson R, Baldocchi D, Bottenheim JW, Ciccioli P, Lamb B, Geron C, Gu L, Guenther A, Sharkey TD, Stockwell W *Bulletin of the American Meteorological Society* **2000**, *81*, 1537-1575.

21. Guenther, A.; Hewitt, C. N.; Erickson, D.; Fall, R.; Geron, C.; Graedel, T.; Harley, P.; Klinger, L.; Lerdau, M.; et al. *Journal of Geophysical Research, [Atmospheres]* **1995**, *100*, 8873-8892.

22. Guenther, A.; Zimmerman, P.; Wildermuth, M. *Atmospheric Environment* **1994**, *28*, 1197-1210.

23. Atkinson, R.; Arey, J. *Atmospheric Environment* **2003**, *37*, S197-S219.

24. Jaoui, M.; Kamens, R. M. *Journal of Atmospheric Chemistry* **2003**, *44*, 259-297.

25. Kroll, J. H.; Ng, N. L.; Murphy, S. M.; Varutbangkul, V.; Flagan, R. C.; Seinfeld, J. H. *Journal of Geophysical Research, [Atmospheres]* **2005**, *110*, D23207/23201-D23207/23210.

26. Griffin, R. J.; Cocker, D. R., III; Seinfeld, J. H.; Dabdub, D. *Geophysical Research Letters* **1999**, *26*, 2721-2724.

27. Odum, J. R.; Hoffmann, M. R.; Bowman, F. M.; Collins, D.; Flagan, R. C.; Seinfeld, J. H. *Environmental Science and Technology* **1996**, *30*, 2580-2585.

28. Jang, M.; Kamens, R. M. *Atmospheric Environment* **1998**, *33*, 459-474.

29. Docherty, K. S.; Wu, W.; Lim, Y. B.; Ziemann, P. J. *Environ Sci Technol* **2005**, *39*, 4049-4059.

30. Lim, Y. B.; Ziemann, P. J. *Environmental Science and Technology* **2005**, *39*, 9229-9236.

31. Gong, H.; Matsunaga, A.; Ziemann, P. J. *Journal of Physical Chemistry A* **2005**, *109*, 4312-4324.

32. Odum, J. R.; Hoffmann, T.; Bowman, F.; Collins, D.; Flagan, R. C.; Seinfeld, J. H. *Environmental Science and Technology* **1996**, *30*, 2580-2585.

33. Pankow, J. F. *Atmospheric Environment* **1994**, *28*, 185-188.

34. Pankow, J. F. *Atmospheric Environment* **1994**, *28*, 189-193.

35. Limbeck, A.; Kulmala, M.; Puxbaum, H. *Geophysical Research Letters* **2003**, *30*, doi:10.1029/2003GL017738.

36. Kamens, R. M.; Jaoui, M. *Environmental Science and Technology* **2001**, *35*, 1394-1405.

37. Jang, M.; Kamens, R. *Environmental Science and Technology* **2001**, *35*, 3626-3639.

38. Keywood, M. D.; Varutbangkul, V.; Bahreini, R.; Flagan, R. C.; Seinfeld, J. H. *Environ Sci Technol* **2004**, *38*, 4157-4164.

39. Gao, S.; Keywood, M.; Ng, N. L.; Surratt, J.; Varutbangkul, V.; Bahreini, R.; Flagan, R. C.; Seinfeld, J. H. *Journal of Physical Chemistry A* **2004**, *108*, 10147-10164.

40. Czoschke, N. M.; Jang, M.; Kamens, R. M. *Atmospheric Environment* **2003**, *37*, 4287-4299.

41. Middlebrook, A. M.; Murphy, D. M.; Lee, S.-H.; Thomson, D. S.; Prather, K. A.; Wenzel, R. J.; Liu, D. Y.; Phares, D. J.; Rhoads, K. P.; Wexler, A. S.; Johnston, M. V.; Jimenez, J. L.; Jayne, J. T.; Worsnop, D. R.; Yourshaw, I.; Seinfeld, J. H.; Flagan, R. C. *Journal of Geophysical Research* **2003**, *108*, 8424, doi:8410.1029/2001JD0006600.

42. Jang, M.; Kamens, R. *Environ Sci Technol* **2001**.

43. Tolocka, M. P.; Jang, M.; Ginter, J. M.; Cox, F. J.; Kamens, R.; Johnston, M. V. *Environmental Science and Technology* **2004**, *38*, 1428-1434.

44. Griffin, R. J.; Crocker, D. R.; Flagan, R. C.; Seinfeld, J. H. *Journal of Geophysical Research* **1999**, *104*, 355-3567.

45. Blando, J. D.; Turpin, B. J. *Atmospheric Environment* **2000**, *34*, 1623-1632.

46. Novakov, T.; Penner, J. E. *Nature* **1996**, *365*, 823-826.

47. Herr, C. E. W.; zur Nieden, A.; Stilianakis, N. I.; Eikmann, T. F. *American Journal of Industrial Medicine* **2004**, *46*, 381-385.

48. Noble, C. A.; Prather, K. A. *Mass Spectrometry Reviews* **2000**, *19*, 248-274.

49. Rogge, W. F.; Hildemann, L. M.; Mazurek, M. A.; Cass, G. R.; Simoneit, B. R. T. *Atmospheric Environment* **1993**, *27A*, 1309-1330.

50. Turpin, B. J.; Saxena, P.; Andrews, E. *Atmospheric Environment* **2000**, *34*, 2983-3013.

51. Davis, W. D. *Environmental Science and Technology* **1977**, *11*, 587-592.

52. Davis, W. D. *Environmental Science Research* **1978**, *13*, 395-411.

53. McKeown, P. J.; Johnston, M. V.; Murphy, D. M. *Analytical Chemistry* **1991**, *63*, 2069-2073.

54. Prather, K. A.; Nordmeyer, T.; Salt, K. *Analytical Chemistry* **1994**, *66*, 1403-1407.

55. Tobias, H. J.; Ziemann, P. J. *Analytical Chemistry* **1999**, *71*, 3428-2435.

56. Carson, P. G.; Neubauer, K. R.; Johnston, M. V.; Wexler, A. S. *Journal of Aerosol Science* **1995**, *26*, 535-545.

57. Oktem, B.; Tolocka, M. P.; Johnston, M. V. *Analytical Chemistry* **2004**, *76*, 253-261.

58. Reilly, P. T. A.; Gieray, R. A.; Whitten, W. B.; Ramsey, J. M. *Environmental Science and Technology* **1998**, *32*, 2672-2679.

59. Woods, E.; Smith, G. D.; Dessiarterik, Y.; Baer, T.; Miller, R. E. *Analytical Chemistry* **2001**, *73*, 2317-2322.

60. Mysak, E. R.; Wilson, K. R.; Jimenez-Cruz, M.; Ahmed, M.; Baer, T. *Analytical Chemistry* **2005**, *77*, 5953-5960.

61. Hearn, J. D.; Smith, G. D. *Analytical Chemistry* **2004**, *76*, 2820-2826.

62. LaFranchi, B. W.; Petrucci, G. A. *Journal of the American Society for Mass Spectrometry* **2004**, *15*, 424-430.

63. Canagaratna, M. R.; Jayne, J. T.; Ghertner, D. A.; Herndon, S.; Shi, Q.; Jimenez, J. L.; Silva, P. J.; Williams, P.; Lanni, T.; Drewnick, F.; Demerjian, K. L.; Kolb, C. E.; Worsnop, D. R. *Aerosol Science and Technology* **2004**, *38*, 555-573.

64. Zhang, Q.; Stanier, C.; Canagarantna, M. R.; Jayne, J. T.; Worsnop, D. R.; Pandis, S. N.; Jimenez, J. L. *Environ Sci Technol* **2004**, *38*, 4797-4809.

65. Allen, J. O.; Fergenson, D. P.; Gard, E.; Hughes, L. S.; Morrical, B. D.; Kleeman, M. J.; Gross, D. S.; Galli, M. E.; Prather, K. A.; Cass, G. R. *Environ Sci Technol* **2000**, *34*, 211-217.

66. Gross, D. S.; Galli, M. E.; Silva, P. J.; Wood, S. H.; Liu, D.-Y.; Prather, K. A. *Aerosol Science and Technology* **2000**, *32*, 152-163.

67. Drewnick, F.; Hings, S.; DeCarlo, P.; Jayne, J.; Gonin, M.; Fuhrer, K.; Weimer, S.; Jimenez, J.; Demerjian, K.; Borrmann, S.; Worsnop, D. *Aerosol Science and Technology* **2005**, *39*, 637-658.

68. Jimenez, J. L.; Jayne, J. T.; Shi, Q.; Kolb, C. E.; Worsnop, D. R.; Yourshaw, I.; Seinfeld, J. H.; Flagan, R. C.; Zhang, X. F.; Smith, K.; Morris, J. W.; Davidovits, P. *Journal of Geophysical Research* **2003**, *108*, 8425.

69. Su, Y.; Sipin, M.; Furutani, H.; Prather, K. A. *Analytical Chemistry* **2004**, *76*, 712-719.

70. Suess, D. T.; Prather, K. A. *Chem. Rev.* **1999**, *99*, 3007-3035.

71. Hunt, A. L.; Petrucci, G. A. *TrAC, Trends in Analytical Chemistry* **2002**, *21*, 74-81.

72. Johnston, M. V. *Journal of Mass Spectrometry* **2000**, *35*, 585-595.

73. Ziemann, P. J. *TrAC, Trends in Analytical Chemistry* **1998**, *17*, 322-328.

74. Wexler, A.; Prather, K. *Aerosol Science and Technology* **2000**, *33*, 1-2.

75. Sullivan, R. C.; Prather, K. A. *Analytical Chemistry* **2005**, *77*, 3861-3885.

76. Murphy, D. M.; Thomson, D. S. *Aerosol Science and Technology* **1995**, *22*, 237-249.

77. Hinz, K.-P.; Kaufmann, R.; Spengler, B. *Analytical Chemistry* **1994**, *66*, 2071-2076.

78. Kievit, O.; Weiss, M.; Verheijen, P. J. T.; Marijnissen, J. C. M.; Scarlett, B. *Chemical Engineering Communications* **1996**, *151*, 79-100.

79. Yang, M.; Reilly, P. T. A.; Boraas, K. B.; Whitten, W. B.; Ramsey, J. M. *Rapid Communications in Mass Spectrometry* **1996**, *10*, 347-351.

80. Zelenyuk, A.; Cabalo, J.; Baer, T.; Miller, R. E. *Analytical Chemistry* **1999**, *71*, 1802-1808.

81. Jayne, J. T.; Leard, D. C.; Zhang, X.; Davidovits, P.; Smith, K. A.; Kolb, C. E.; Worsnop, D. R. *Aerosol Science and Technology* **2000**, *33*, 49-70.

82. Nordmeyer, T.; Prather, K. A. *Analytical Chemistry* **1994**, *66*, 3540-3542.

83. Carson, P. G.; Johnston, M. V.; Wexler, A. S. *Rapid Communications in Mass Spectrometry* **1997**, *11*, 993-996.

84. Tolocka, M. P.; Heaton, K. J.; Dreyfus, M. A.; Wang, S.; Zordan, C. A.; Saul, T. D.; Johnston, M. V. *Environ Sci Technol* **2006**, *40*, 1843-1848.

85. Van Bramer, S. E.; Johnston, M. V. *Applied Spectroscopy* **1992**, *46*, 255-261.

86. Van Bramer, S. E.; Johnston, M. V. *J. Amer. Soc. Mass Spectrom.* **1990**, *1*, 419-426.

87. Nash, D. G.; Liu, X. F.; Mysak, E. R.; Baer, T. *International Journal of Mass Spectrometry* **2005**, *241*, 89-97.

88. Zahardis, J.; LaFranchi, B. W.; Petrucci, G. A. *Atmospheric Environment* **2006**, *40*, 1661-1670.

89. LaFranchi, B. W.; Zahardis, J.; Petrucci, G. A. *Rapid Communications in Mass Spectrometry* **2004**, *18*, 2517-2521.

90. Slowik, J. G.; Stainken, K.; Davidovits, P.; Williams, L. R.; Jayne, J. T.; Kolb, C. E.; Worsnop, D. R.; Rudich, Y.; DeCarlo, P. F.; Jimenez, J. L. *Aerosol Science and Technology* **2004**, *38*, 1206-1222.

91. Morris, J. W.; Davidovits, P.; Jayne, J. T.; Jimenez, J. L.; Shi, Q.; Kolb, C. E.; Worsnop, D. R.; Barney, W. S.; Cass, G. R. *Geophysical Research Letters* **2002**, *29*, 1-4.

92. Kolb, C. E.; Davidovits, P.; Jayne, J. T.; Shi, Q.; Worsnop, D. R. *Progress in Reaction Kinetics and Mechanism* **2002**, *27*, 1-46.

93. Worsnop, D. R.; Morris, J. W.; Shi, Q.; Davidovits, P.; Kolb, C. E. *Geophysical Research Letters* **2002**, *29*, doi:10.1029/2002GL015542.

94. Worsnop, D. R.; Shi, Q.; Jayne, J. T.; Kolb, C. E.; Swartz, E.; Davidovits, P. *Journal of Aerosol Science* **2001**, *32*, 877-891.

95. Ziemann, P. J. *Journal of Physical Chemistry A* **2003**, *107*, 2048-2060.

96. Sakurai, H.; Park, K.; McMurry, P. H.; Zarling, D.; Kittelson, D. B.; Ziemann, P. J. *Environ Sci Technol* **2003**, *37*, 5487-5495.

97. Tobias, H. J.; Ziemann, P. J. *Environmental Science and Technology* **2000**, *34*, 2105-2115.

98. Tobias, H. J.; Ziemann, P. J. *Journal of Physical Chemistry A* **2001**, *105*, 6129-6135.

99. NIST In; U.S. Secretary of Commerce, 2005.

100. Hearn, J. D.; Smith, G. D. *Physical Chemistry Chemical Physics* **2005**, *7*, 2549-2551.

101. Hearn, J. D.; Smith, G. D. *Journal of Physical Chemistry A* **2004**, *108*, 10019-10029.

102. Hearn, J. D.; Lovett, A. J.; Smith, G. D. *Physical Chemistry Chemical Physics* **2005**, *7*, 501-511.

CHAPTER 2:
Synchrotron Radiation Based Aerosol Time-of-Flight Mass Spectrometry for Organic Constituents

2.1 Introduction

Aerosols, ubiquitous throughout the atmosphere, have varied chemical compositions as well as diverse physical characteristics that affect the chemistry of the atmosphere, the earth's climate, and human health. Aerosol particles range in diameter from approximately 2 nm to 100 μm, and thus vary in particle mass by a factor of 10^{14}. Considering both total mass and surface area, the most important size range consists of ultrafine particles with diameters less than 300 nm.[1] Aerosols in the atmosphere are often mixtures of water, sea salts, acids, elemental carbon, sulfates, nitrates, mineral oxides, and organic matter.[1] Recent measurements indicate that significant amounts of aerosols containing organic compounds are found throughout the troposphere.[2-4] Organic aerosols are of particular concern because of their high mass concentrations[1] and their potentially negative health effects.[5] The need for effective methods for organic aerosol analysis is widely recognized,[6-10] however real-time analysis of these delicate organics is quite challenging.[6]

Since its development in the early 1990's, aerosol mass spectrometry has become an increasingly important analysis tool because of its high sensitivity and its ability to rapidly analyze particles in real time. Instruments are now used routinely in both laboratory[11-15] as

well as field studies.[16-20] Although a variety of spectrometer types are currently in use, they all involve particle injection into the vacuum chamber in the form of a well directed beam followed by vaporization and ionization of their constituent components. Because of the broad range of constituents, no single ionization approach is capable of analyzing all particles quantitatively. Salts are most easily vaporized and ionized by ablation with a single UV laser pulse.[21;22] However, the high laser power results in multiphoton processes that lead to extensive fragmentation of organic constituents thereby preventing speciation of these compounds.

The analysis of organic constituents requires the separation of the vaporization and ionization processes as well as a "soft" ionization method. Vaporization of organic compounds in aerosols has been accomplished either by hitting individual particles with a pulsed IR laser[23-25] or allowing the particles to hit a hot surface.[26;27] The most effective "soft" ionization methods employed are single photon photoionzation,[7;15] chemical ionization,[28] and photoelectron resonance capture ionization.[29]

Most aerosols found in the atmosphere contain complex mixtures of organic species, including alkanes, alkenes, alcohols, fatty acids, and aromatics.[9] Although electron impact ionization is a common mass spectrometric ionization source for mixture analysis, it is generally used in conjunction with a prior separation step such as a gas-liquid chromatograph. This two-dimensional approach is essential because of the extensive fragmentation that inevitably accompanies electron impact ionization. Because such a two-dimensional method is not practical for aerosol particle analysis, the electron impact spectra of urban aerosol particles have exhibited a bewildering number of mass peaks that are extremely difficult to identify.[18;20;30] It is for this reason that "soft" ionization methods such

as single photon photoionization, chemical ionization, or photoelectron capture ionization offer attractive alternative paths for aerosol analysis. Our laboratory in Chapel Hill has reduced ion fragmentation by gently vaporizing the particles, and by utilizing the minimum energy photon required to ionize the molecules. Because the majority of organic compounds have ionization energies (IE) between 8-11 eV, a good choice for a photon energy is 10.5 eV,[15] easily produced by third harmonic generation in Xe. The third harmonic of a pulsed Nd:YAG at 355 nm is focused into a Xe cell which produces about 10^{10} photons per second at 118 nm (10.5 eV). For larger molecular constituents with lower ionization energies, Nash et al.[31] have reported the use of 4-wave mixing in Kr to generate light at 8.75 eV. Photoionization at threshold results in a dominant molecular ion peak, which facilitates molecular identification. The ideal photon source is tunable so that its energy can be adjusted for each molecule.

A major divide between aerosol mass spectrometers is in their ability to detect large and small particles. Particles are deemed large if their diameter exceeds 0.3 μm so that they can be detected by visible laser light scattering. In that case, their arrival in the mass spectrometer can be detected by laser light scattering signal on a photomultiplier. This technique permits the use of pulsed lasers that can be triggered to intercept the particles as they fly through the ionization region.[11;15;32] It is thus possible to obtain a complete mass spectrum of a single particle by time-of-flight mass analysis. The ability to direct a large number of Vacuum UV photons (ca 10^{10}) into the ionization region precisely when the particle is vaporized in a confined space makes this a near ideal match of sample and radiation density.

In contrast to the large particles, a major problem with ultrafine particles (diameters less than 300 nm) is the inefficiency with which pulsed lasers ionize or ablate them. Although the mass concentration of larger particles is comparable to that of the ultrafine fraction, the number concentration of the latter far exceeds that of the larger particles. Ultrafine particles are of concern because they are readily inhaled into the human respiratory system and are highly toxic to human health.[33-36] Because the large number of ultrafine particles enters the mass spectrometer in a quasi continuous stream, the typical 10 Hz laser is capable of ionizing only a small fraction of them. Johnston and coworkers[7] have solved this problem by collecting the particle stream on a cold probe and then vaporizing them with an IR laser so that the 10 Hz Vacuum UV laser can still be used. In the absence of such a "sample concentrator" it is necessary to employ a continuous ionization source with much higher photon flux.

In this study, we turn to synchrotron radiation (SR) as a source of high intensity photons. We illustrate the capability of this source for ultrafine particles by collecting mass spectra of four high molecular weight compounds of considerable relevance in atmospheric chemistry. These are oleic acid, linoleic acid, linolenic acid, and cholesterol (Scheme 2.1). SR is a spatially confined quasi-continuous beam with high photon flux that is ideal for ultrafine particle analysis. In addition, the tunability of SR allows for multi-dimensional peak analysis. That is, a molecule can be identified by its molecular and fragment ion masses as well as by its ionization energy measurable with tunable SR. One of the significant advantages of tunable VUV ionization is that fragment free mass spectra can be obtained by ionizing the molecules at their ionization threshold. The utility of this technique for

examining complex mixtures of fragile compounds is an issue that will arise in a forthcoming chapter involving multi-component aerosol particles.

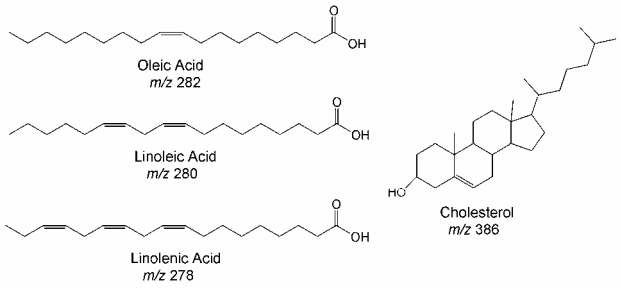

Scheme 2.1. Structures of four compounds.

2.2 Experimental Section

2.2.1 Particle Generation

Particles were created using a Constant Output Atomizer (TSI, Inc. Model 3076), which creates an aerosol by introducing a high velocity gas jet normal to a liquid stream drawn from a reservoir by capillary action. The jet was formed by passing N_2 at a flowrate of 1 L/min at a pressure of 1 atmosphere through a small orifice. Large particles were removed immediately by impaction on the wall opposite the jet stream. Polydispersed, wet, and charged particles were prepared by atomizing a 1000:1 diluted sample in isopropanol. The isopropanol solvent was removed by passing the aerosol through a stainless steel tube wrapped in heating tape, and then dried by a 1 m home-constructed diffusion dryer filled with silica gel. The dry particles were transported with conductive silicon tubing to an inertial impactor with an orifice size of 0.071 cm. Particles small enough to follow the gas stream were directed in one of two ways: either into the experimental chamber for mass

spectral analysis or into a scanning mobility particle sizer (SMPS) (TSI, Inc. Model 3986) for particle number concentration characterization. The SMPS system consists of an Electrostatic Classifier (TSI, Inc. Model 3080) and an Ultrafine Condensation Particle Counter (CPC) (TSI, Inc. Model 3025A). As the aerosol entered the Electrostatic Classifier, it was directed into a Kr-85 neutralizer for charge equilibration and then into a long differential mobility analyzer (DMA). The DMA ramps its voltage in discrete steps so that particles pass through based on their electrostatic mobility. As particles exited the DMA, they were guided into an Ultrafine CPC that counts the number of particles of each size bin. Particles with a mean number diameter of 110 nm (geometric standard deviation = $\sigma_g \sim 1.8$) and a typical particle density of 1.3×10^7 particles per cubic centimeter were generated as determined with the DMA/CPC combination. For mass spectral analysis, the particles were directed through conductive tubing to a t-junction, where excess aerosol was exhausted and 0.25 L/min was drawn into the MS through a flow-limiting orifice.

2.2.2 Aerosol Mass Spectrometer

A schematic of the aerosol TOF-MS instrument designed and constructed at the Chemical Dynamics Beamline at the Advanced Light Source is illustrated in Figure 2.1. Particles were sampled into the mass spectrometer through a 200 μm i.d. flow-limiting orifice located at the inlet of an 18 in. long (1/2 in. o.d., 0.4 in i.d.) stainless steel tube. The flow through this orifice was calculated to be 0.25 L/min (4.17 cc/s), and the inlet pressure was measured to be 7.40 Torr. As particles pass through an aerodynamic lens system modeled after Liu and coworkers,[37;38] they are focused through the final 3.00 mm nozzle, where they exit the aerodynamic lens into vacuum and are accelerated by the gas expansion. The particles passed through two stages of differential pumping; the first stage was evacuated

by a Shimadzu turbomolecular pump (Model TMP-2203LMC; 2050 L/s), and the second stage was pumped by an Osaka Vacuum compound molecular pump (Model TG383M ; 340 L/s). The main chamber was pumped to a pressure with particle load of 1.7×10^{-7} Torr by a Shimadzu turbomolecular pump (TMP-1103LMPC; 1080 L/s).

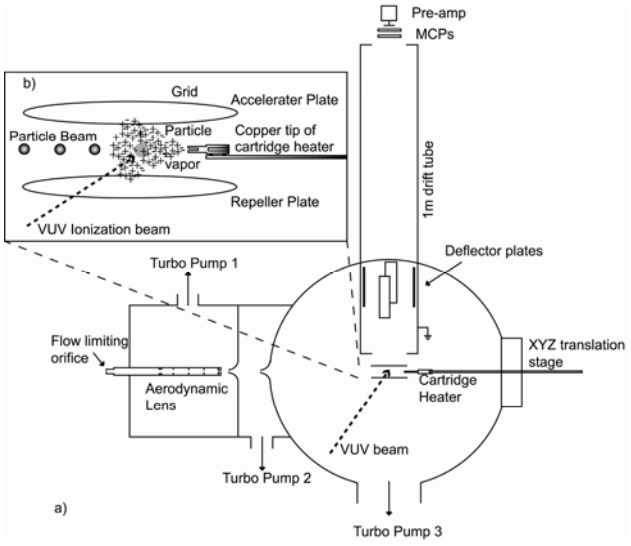

Figure 2.1. a) Schematic of Aerosol TOF-MS. The main components include: (1) a flow limiting aerosol inlet through which particles pass to enter the aerodynamic lens system that collimates the particle beam, (2) a cartridge heater that vaporizes the particles in the ionization region, (3) VUV light produced with the synchrotron source, and (4) linear time of light tube with micro channel plate detection, processed with a fast time of flight card after signal amplification. b) Expanded view of vaporization/ionization region, consisting of a cartridge heater surrounded by a copper tip, and the VUV beam ionizing particle vapor expanding normal to synchrotron's incidence.

As the particles entered the ionization region of the main chamber, they impinged on a cartridge heater with a copper tip as described previously by Sykes and coworkers.[26] The heater tip whose position is controlled by an XYZ translation stage was placed about 1.5 cm from the center of the ionization region. This distance is a compromise between maximizing the vapor density reaching the ionization beam and minimizing the electrical field interference caused by the tip between the extraction plates. The tip was designed with a deep crevice so that as the particles vaporized on the heater, they expanded back into the

ionization region in a somewhat confined plume. A Watlow Series CV temperature controller allowed temperature adjustment. As explained in the Results and Discussion section, the optimal heater temperature for measurements was determined to be about 400 K.

The quasi-continuous plume of vaporized particles was irradiated with a quasi-continuous synchrotron photon beam. Light from the Chemical Dynamics Beamline of the Advanced Light Source (ALS) of Lawrence Berkeley National Laboratory[39] is produced with an undulator that can be tuned to generate photons between 7 and 25 eV. This spatially confined photon beam is directed into the ionization region of the experimental chamber, where approximately 10^{15} photons per second are delivered to the sample. The photon energy is easily tuned by changing the gap between the undulator magnets.

Ions were formed in the middle of a 2 cm acceleration region, and were then further accelerated in a 0.5 cm region before they drifted through a 1 m field-free region. Typically, the repeller plate was biased at 2.06 kV, the accelerator was held constant at 2.06 kV, and the drift tube was held at ground. Because the particle and the photon beam were both quasi-continuous, and the vaporization source was continuous, pulsed extraction was used to initiate time-of-flight MS signal collection. The repeller plate was pulsed from 2.06 kV to 2.72 kV for 3 μs and mass spectra were collected at a rate of 5 kHz. Four ion deflection plates located inside the drift tube were adjusted to optimize ion signal intensity. The deflectors were controlled individually with a variable power supply (Spectrum Solutions, INC.), and values were varied between approximately −100 and +200 V. The ion signal was collected by multichannel plates and amplified by an Ortec VT120 negative mode fast preamplifier. A DEI PVX-4140 high voltage pulse generator simultaneously pulsed the repeller voltage and triggered a digital delay pulse generator (Standford Research Systems

Model DG535) used to convert the TTL pulse to a NIM pulse. This NIM signal initiated TOF collection recorded by a multichannel scaler (FAST Comtec P7886). Typically, spectra were collected in 2496 channels of 16ns width for 16384 (2^{14}) to 1048576 (2^{20}) sweeps (pulsed extraction cycles).

The mass spectrometer operation could be considerably improved by floating the drift region, which would permit operating the ionization region at ground potential. This change would prevent electric field disruption by the grounded heater and thus allow the heater to be moved to within 5-7 mm of the ionization region, which would increase gas density in the ionization region. Operating the ion extraction pulser from ground potential will allow pulsing at a maximum rate of 25 kHz, given the 40 μs ion flight time. Although ions are constantly produced, they probably do not remain in the ionization region for more than about 10 μs. Thus the duty factor for this mode of operation would be 0.25. Each of these changes would increase the signal by a factor of about 5 thus improving the signal by a factor of 25. These changes are addressed in the next chapter.

2.2.3 Chemicals

All chemicals were used without further purification: oleic acid (Mallinckroft, CAS #112-80-1), linoleic acid (Alfa Aesar, CAS #60-33-3), linolenic acid (TCI America, CAS #463-40-1), cholesterol (Alfa Aesar, CAS #57-88-5), and isopropanol (VWR, CAS #67-63-0).

2.3 Results and Discussion

2.3.1 Mass Spectra

Representative mass spectra of several high-molecular weight atmospherically relevant compounds are shown in Figure 2.2. Pure oleic, linoleic, and linolenic acids as well as cholesterol particles are vaporized with a heater and ionized with either 8.8 or 10 eV photons. These spectra are remarkably clean, showing only minimal fragmentation. By comparison, the standard electron impact mass spectrum of oleic acid has a parent peak that is only 0.01% as strong as the dominant fragment ion peak.[40;41] The oleic acid parent ion in Figure 2.2 is also considerably stronger than that reported by Sykes et al.[26] who used 10.5 eV lasers. The difference may be a result of the lower heater temperature and smaller diameter particles used in the present study. Indeed, as shown by Sykes et al.[26] and Nash et al.[31] raising the heater temperature increases the amount of fragmentation.

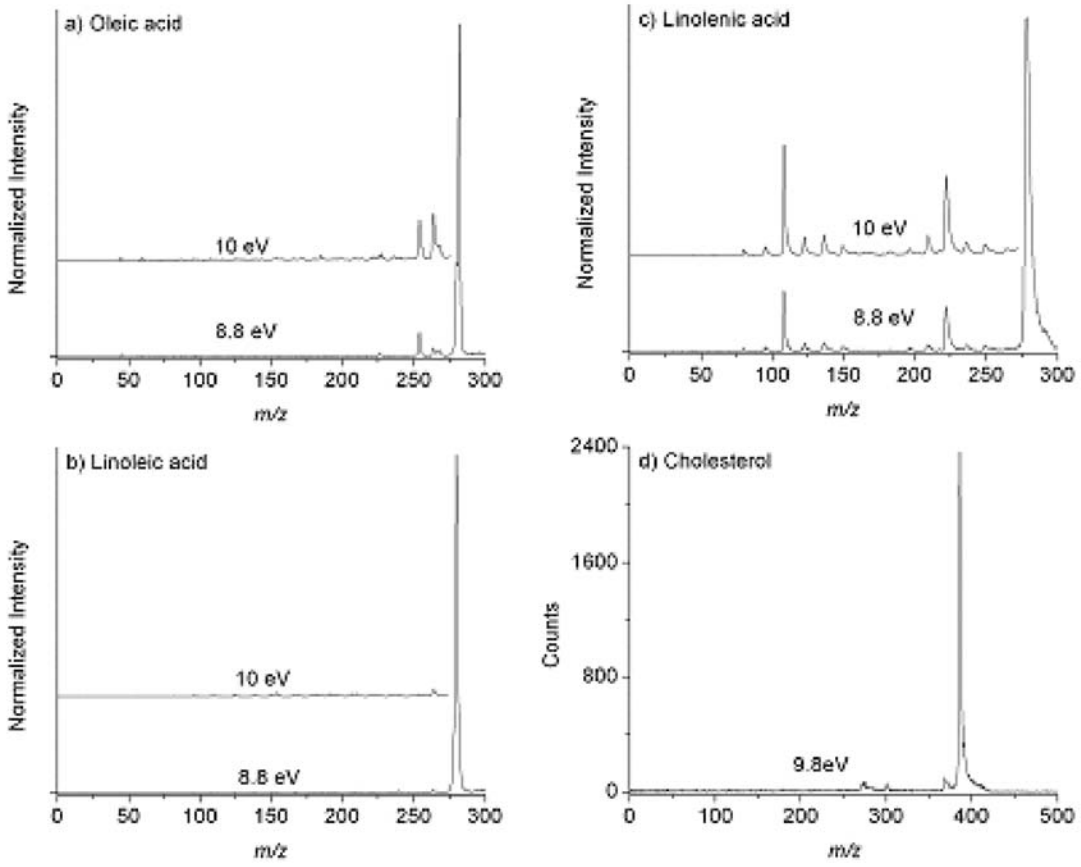

Figure 2.2. Photoionization mass spectra of a) oleic acid signal with photon energy 8.8 and 10 eV b) linoleic acid signal with photon energy 8.8 and 10 eV c) linolenic acid with photon energy 8.8 and 10 eV and d) cholesterol with photon energy 9.8 eV. In graphs a-c, the molecular ion peak is normalized at the two photon energies so that the relative intensities of the fragments can be viewed. The molecular ions are not shown in the 10 eV spectra. As the photon energy is increased, fragmentation of the three unsaturated acids increases.

The mass spectrum of oleic acid contains a water loss peak at 264 *m/z* and an acetylene loss peak at 256 *m/z*. The water loss peak is characteristic of many organic acids.[42] It is however interesting that linoleic and linolenic acids, which contain two and three double bonds, respectively, show no water loss peaks up to 10 eV. The cholesterol mass spectrum shows a large molecular ion peak (386 *m/z*) and less intense fragment ions at 368 *m/z* (water loss) and 301 *m/z*.

An important issue in aerosol particle analysis is the sensitivity or detection limit of the mass spectrometer. In this experiment, an average of 32768 sweeps yields a signal-to-noise ratio (SNR) of ~320 for the three acids, and a SNR of 125 for cholesterol. A particle density of 1.3×10^7 particles per cubic centimeter of 110nm diameter particles, assuming the liquid density is 0.89 g/cm^3, produces a particle mass density of 8060 μg/m^3. By both moving the heater closer to the ionization region and by increasing the pulse rate, we could maintain the current SNR with 25 times less sample mass density, or 323 μg/m^3. By assuming that the detection limit is defined as a SNR = 3, our current detection limit is 76 μg/m^3, and with improvements, would be 3 μg/m^3. Although this instrument is not intended for field measurements, it is useful to compare its detection limit to ambient aerosol concentrations. Typical mass concentrations of $PM_{2.5}$ (particulate matter less than 2.5 μm diameter) in cities worldwide range between 29.1 and 140 μg/m^3,[43-46] although it should be noted that the concentration of individual components in typical aerosols will be on the order of ng/m^3. The detection limit of this instrument based on the suggested improvements is only an order of magnitude higher than that of the Aerodyne field instrument, which is based on EI of ultrafine particles.[47]

Although a continuous ionization source is optimal for the detection of ultrafine particles, experiments implementing pulsed lasers triggered on large particles have a significantly lower detection limit. For comparison purposes, if we assume that the pulsed laser experiment in our laboratory at Chapel Hill[15;31] has a particle flow of 1 particle per second of 1 μm diameter particles, and that the liquid density is 0.89 g/cm^3, we calculate that 4.66×10^{-13} g/s of sample arrives in the ionization region. The flow rate through the flow-limiting orifice is 1.2 cc/s, thus the mass density of the aerosol sampled is 0.39 μg/m^3, which

is an order of magnitude lower than is possible with the continuous synchrotron based experiment. The lower detection limit of the pulsed laser scheme is a result of the efficiency with which the laser's photons (10^{10} photons per pulse) can be used by firing only when a large gas density is generated by the arrival of the micron sized particle. It should be noted that the laser based system can detect ion signal from merely one particle so that there is no effective lower limit in the aerosol number density that can be detected. However, if particles are too small for coincidence laser firing, then the pulsed laser loses its efficiency due to its low photon flux. A much higher photon flux (ca 10^{15}) is essential when using a continuous ionization source.

2.3.2 Signal as a Function of Heater Temperature

The oleic acid molecular ion signal as a function of heater temperature is shown in Figure 2.3. The photon energy of 10.0 eV is a compromise between a lower photon energy that would reduce fragmentation even more, and a higher photon energy that would increase the total signal level. The signal for the three acids leveled off at about 400 K, indicating complete vaporization. The experiments with the three acids were run at that temperature in order to maximize parent signal and minimize internal energy given to the molecules that would cause fragmentation. The cholesterol particles required a temperature of about 500 K for maximum signal. In the case of oleic acid, the amount of fragmentation increased from 16 to 19% when the temperature was increased from 400 K to 650 K. A similar increase was noted when the photon energy was increased from 8.8 to 10 eV.

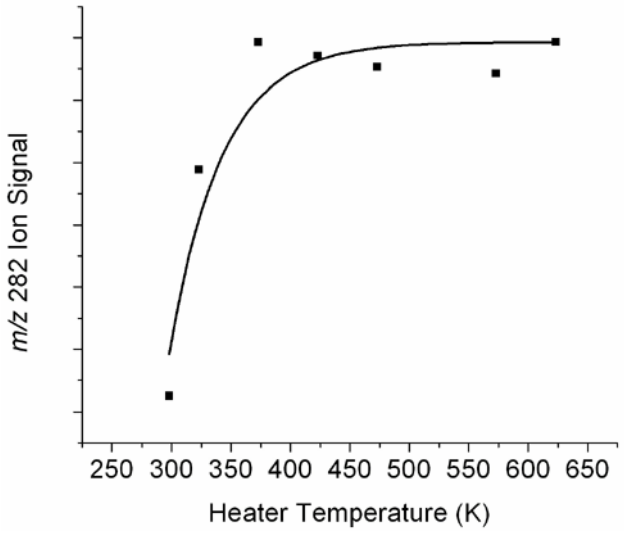

Figure 2.3. Oleic acid molecular ion signal (282 m/z) as a function of heater temperature. The leveling off of the oleic acid molecular ion signal at higher temperatures provides evidence that entire particles are being vaporized.

2.3.3 Photoionization Efficiency Curves

As shown in Figure 2.2, the fragment ions are more prominent at 10 eV photon energy. Photoionization efficiency (PIE) curves, acquired by scanning the photon energy, can be used to measure the ionization energy and the fragment appearance energies for our four compounds. The photon energy was scanned between 7.8 and 12.0 eV and mass spectra collected at 0.1 eV photon energy intervals. Areas under the parent and fragment ion peaks were integrated at each photon energy and the area plotted as a function of photon energy.

Undulator light with its resolution of 0.2 eV at 10 eV photon energy is directed through a gas filter and two MgF_2 windows before entering the experimental chamber. The gas filter, filled with 30 Torr Ar gas, removed higher order harmonics produced by the undulator and the MgF_2 windows added an extra filter for light above 11 eV. Figure 2.4 shows a profile of the light intensity as a function of photon energy as measured with a photodiode inside the experimental chamber. The intensity increase at low energy is a result of the SR characteristics. The decrease after 8.9 eV is a result of the MgF_2 windows. Our

experiment was positioned at Terminal 1 of the Chemical Dynamics Beamline, which does not use a monochrometer thereby maximizing the photon flux.

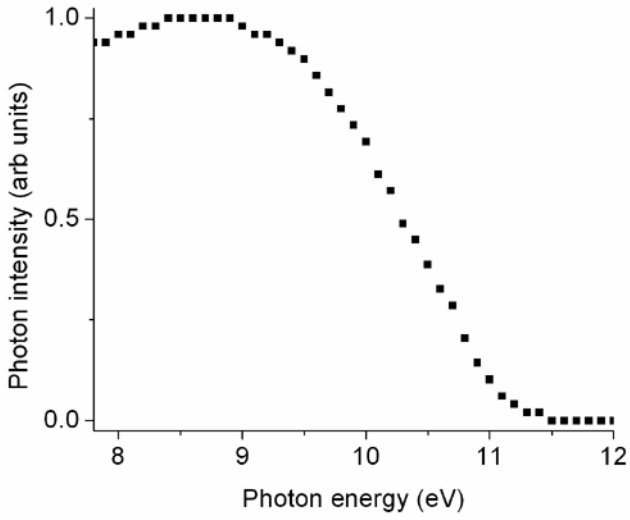

Figure 2.4. Intensity of synchrotron light as a function of photon energy. The decrease between 9.5 and 11 eV is a result of the MgF_2 windows.

The PIE curves in Figure 2.5 for three reference gases with known ionization energies (ClC_6H_5, BrC_6H_5, and IC_6H_5) are used to calibrate the photon energy and to obtain ionization energies with a precision superior to the 0.2 eV photon band pass. We can create a linear fit through the data points and thus determine an appearance energy (AE) for these ions. The measured AE's for chlorobenzene (9.08 ± 0.05 eV) and bromobenzene (9.01 ± 0.06 eV) are very close to the reported ionization energy of 9.07 ± 0.02 eV and 9.00eV ± 0.03 eV, respectively.[40] A combination of experimental and fitting error leads to the 50 and 60 meV uncertainties, as evidenced in Figure 2.6 where two consecutive scans of the same molecule are shown. The IE analysis of IC_6H_5 is more difficult because two widely spaced electronic states result in sharp photoelectron peaks that show up as two inflection points in the PIE scan.[48] Fitting a straight line through only the first portion of the PIE curve does not yield a straight line that intersects the energy axis at the known IE for iodobenzene. In contrast to

iodobenzene, the other two halobenzenes have broader electronic states in these energy ranges,[48] and thus yield PIE curves that rise linearly with the photon energy.

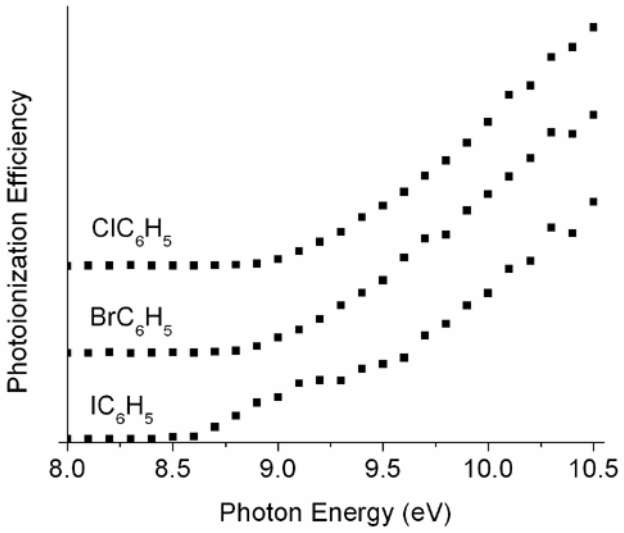

Figure 2.5. PIE curves for ClC_6H_5, BrC_6H_5, and IC_6H_5.

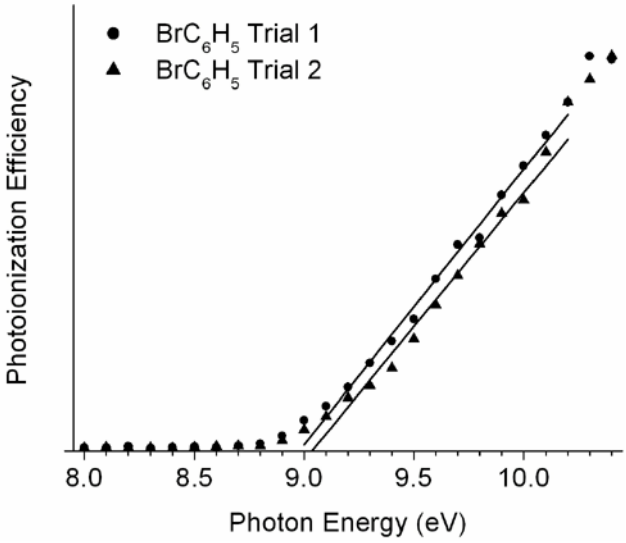

Figure 2.6. Two trials of PIE curves for BrC_6H_5.

Oleic, linoleic, and linolenic acids and cholesterol (Figures 2.7a-d) have linear PIE curves similar to those of ClC_6H_5 and BrC_6H_5 so that we can apply the same procedure to them as the chloro and bromobenzene molecules. The best fit lines through the PIE curves of the four sample molecules are used to obtain the ionization energies of 8.68 eV (oleic acid),

8.52 eV (linoleic acid), 8.49 eV (linolenic acid), and 8.69 eV (cholesterol). The error in the linear regression calculation for these four samples was smaller than the error determined with the reference samples, thus the estimated error for all samples is ± 60 meV. The relatively sharp onsets for oleic and linolenic acids suggest that our derived energies are close to the adiabatic ionization energies. The precise interpretation of PIE onsets for large molecules is made difficult by largely unknown Franck-Condon factors and hot bands. A better approach for the determination of adiabatic IE's would be an electron transfer equilibrium study in which the complicating issues of Franck-Condon factors associated with the ionization process are avoided.[49;50]

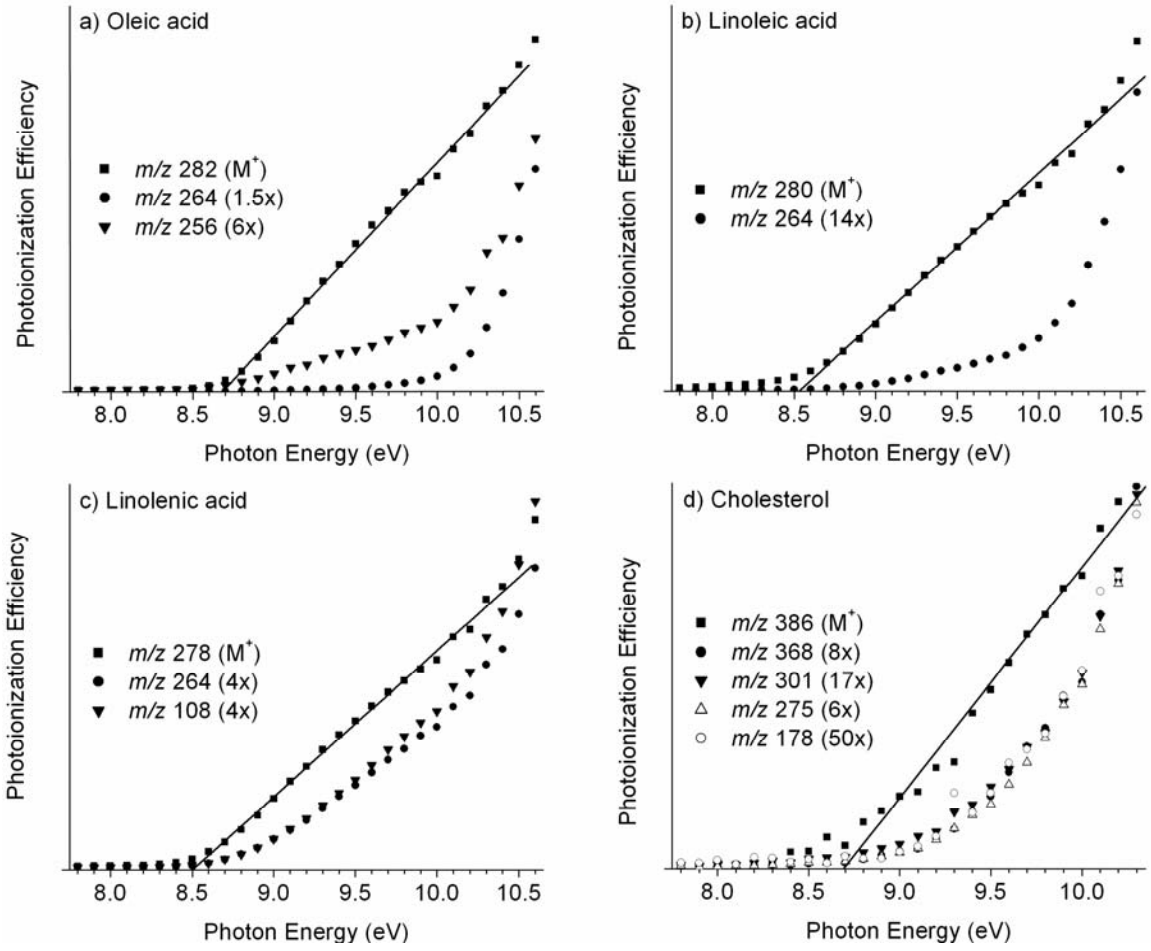

Figure 2.7. PIE curves for a) oleic acid, b) linoleic acid, c) linolenic acid, and d) cholesterol. The multiplier associated with the fragment ion peaks shows the factor by which the signal was multiplied.

Figures 2.7 a-d also display appearance energies for daughter ions. The dissociation onset for the first fragment ion for all four ions is very close to the IE, which indicates that these parent ions are not very stable, a conclusion consistent with the very small parent ion signal in the standard 70 eV electron impact mass spectrum. In fact, for both oleic and linolenic acids, the fragment ions appear at almost the same energy as their parent ions. The fragment ion signal rises with energy in a considerably more gentle manner than their parent ions which is probably a result of a slow dissociation reaction. Evidence for a slow water loss reaction (264 *m/z*) in the case of oleic acid has been reported.[31] As a result, we cannot identify the observed appearance energy with a thermochemical dissociation limit without measuring the dissociation rates and accounting for the kinetic shift.[51;52]

An inevitable question arises when ionizing a low volatility sample that requires heating in order to vaporize. Are the fragments a result of neutral dissociation prior to ionization, or are they a result of dissociative photoionization of a hot neutral molecule? In principle the two processes could be distinguished. If heating dissociates the sample, both fragments can be ionized. In the case of oleic acid, the neutrals would be the water loss product and the water molecule. Unfortunately, removal of the MgF_2 window and increasing the photon energy to 12.6 eV (the H_2O ionization energy) resulted in so much fragmentation of the oleic acid ion that the results were not conclusive. However, in general, the dissociation energies of ions are much lower than those of stable neutral molecules so that it is highly unlikely that any of the four molecules were fragmented by the heater.

The fragmentation of the three closely related acids is remarkably different. Oleic acid dissociates via H_2O and C_2H_2 loss. Water loss is common in the ionization of small organic acids.[42] Both water and acetylene losses involve rearrangements, which are expected

for low energy dissociations. The remarkable finding is that the addition of one double bond to oleic acid completely changes the fragmentation of the ion. Linoleic acid is not only more stable, but it dissociates via loss of 16 *m/z*, which is presumably methane. Methane loss at the hydrocarbon terminus would result in an ion with three double bonds. Why water loss, which takes place at the acid end of the molecule, should be so facile with oleic acid, but not observed at all with linoleic or linolenic acid is surprising. How can the presence of a second or third double bond some 9 carbon atoms away from the acid group, prevent water loss? It suggests that the water loss channel must involve the hydrocarbon chain, which may donate a hydrogen atom in the water loss reaction. Why is this H-atom transfer suppressed in the case of linoleic and linolenic acids? It is known that rapid hydrogen transfer can result in double bond migration.[53] However, in the case of linoleic and linolenic acid, double bond migration via rapid H atom transfers may convert the non-conjugated hydrocarbon chain into a conjugated configuration, which stabilizes the molecule sufficiently to prevent H donation for the water loss fragmentation channel. Finally, the triply double bonded linolenic acid dissociates to 222 and 108 *m/z*, which we assign to C_4H_8 and $C_{10}H_{18}O_2$ loss, respectively. We suspect that linolenic acid loses C_4H_8 from its carbon tail, and that the presence of the double bond facilitates this dissociation.

2.4 Conclusions

This is the first aerosol mass spectrometric study with a tunable ionization source. The continuous and intense light source from the undulator permits the analysis of a continuous stream of ultrafine particles. The observation of mostly parent ion signal for the three fatty acids when using low energy photons demonstrates that the vaporization process

with the heater set to 400 K does not impart sufficient internal energy to the molecules to cause fragmentation.

The notably clean mass spectra obtained for the four molecules in this study suggests that low energy photoionization is ideal for the study of more complex particles, for example gas surface reactions with aerosol particles and homogeneous nucleation studies. It is well known, for instance, that the aerosols generated by the reaction of ozone with α-pinene or isoprene results in the formation of particles that contain complex mixtures of organic species, which are difficult to identify.[54-57] Because the molecular composition of homogeneous nucleation reactions may vary with reaction time and particle size, a rapid analysis tool such as that described here would seem to be ideal for such controlled laboratory studies. Such studies are currently in progress.

The major disadvantage of this instrument is that the ionization source is not portable. This is not a problem for controlled laboratory studies that can be carried out at a synchrotron. However, this instrument clearly cannot be employed in a field portable experiment. On the other hand, small and readily portable rare gas resonance lamps that generate light at selected energies (Kr at 10.0 eV and Xe at 8.4 eV) may satisfy the requirements. They are nearly as intense as the synchrotron's undulator light, although not as coherent.

REFERENCES

1. Finlayson-Pitts, B. J.; Pitts, J. N. *Chemistry of the Upper and Lower Atmosphere: Theory, Experiments and Applications,* Academic Press: New York, 2000.

2. Murphy, D. M.; Thomson, D. S.; Mahoney, M. J. *Science* **1998,** *282*, 1664-69.

3. Rudich, Y. *Chem.Rev.* **2003,** *103*, 5097-124.

4. Sardar, S. B.; Fine, P. M.; Mayo P.R.; Sioutas, C. *Environ.Sci.Technol.* **2005**.

5. National Research Council. **Research Priorities for Airborne Particulate Matter**. 1998. Washington, D.C., National Academies Press.

6. Turpin, B. J.; Saxena, P.; Andrews, E. *Atmos.Environ.* **2000,** *34*, 2983-3013.

7. Oktem, B.; Tolocka, M. P.; Johnston, M. V. *Anal.Chem.* **2004,** *76*, 253-61.

8. Maria, S. F.; Russell, L. M.; Gilles, M. K.; Myneni, S. C. B. *Science* **2004,** *306*, 1921-24.

9. Seinfeld, J. H.; Pandis, S. N. *Atmospheric Chemistry and Physics,* Wiley Interscience: New York, 1998.

10. Turpin, B. J. *Environ.Sci.Technol.* **1999,** *33*, 76A-9A.

11. Prather, K. A.; Nordmeyer, T.; Salt, K. *Anal.Chem.* **1994,** *66*, 1403-07.

12. Tobias, H. J.; Ziemann, P. J. *Anal.Chem.* **1999,** *71*, 3428-35.

13. Johnston, M. V.; Wexler, A. S. *Anal.Chem.* **1995,** *67*, 721A-6A.

14. Reilly, P. T. A.; Lazar, A. C.; Gieray, R. A.; Whitten, W. B.; Ramsey, J. M. *Aerosol Sci.Technol.* **2000,** *33*, 135-52.

15. Woods III, E.; Smith, G. D.; Dessiaterik, Y.; Baer, T.; Miller, R. E. *Anal.Chem.* **2001,** *73*, 2317-22.

16. Gross, D. S.; Galli, M. E.; Silva, P. J.; Wood, S. H.; Liu, D. Y.; Prather, K. A. *Aerosol Sci.Technol.* **2000,** *32*, 152-63.

17. Middlebrook, A. M.; Murphy, D. M.; Lee, S-H.; Thompson, D. S.; Prather, K. A.; Wenzel, R. J.; Liu, D-Y.; Phares, D. J.; Rhoads, K. P.; Wexler, A. S.; Johnston, M. V.; Jimenez, J. L.; Jayne, J. T.; Worsnop, D. R.; Yourshaw, I.; Seinfeld, J. H.; Flagan, R. C. *J.Geophys.Res.* **2003,** *108*, SOS 12-1-SOS 12/13.

18. Canagaratna, M. R.; Jayne, J. T.; Ghertner, D. A.; Scott, S.; Shi, Q.; Jimenez, J. L.; Silva, P. J.; Williams, P.; Lanni, T.; Drewnik, F.; Demerjian, K. L.; Kolb, C. E.; Worsnop, D. R. *Aerosol Sci.Technol.* **2004,** *38*, 555-73.

19. Zhang, Q.; Stanier, C. O.; Canagaratna, M. R.; Jayne, J. T.; Worsnop, D. R.; Pandis, S. N.; Jimenez, J. L. *Environ.Sci.Technol.* **2004,** *38*, 4797-809.

20. Alfara, M. R.; Coe, H.; Allan, J. D.; Bower, K. N.; Boudries, H.; Canagaratna, M. R.; Jimenez, J. L.; Jayne, J. T.; Garforth, A. A.; Li, S. M.; Worsnop, D. R. *Atmos.Environ.* **2004,** *38*, 5745-58.

21. Mansoori, B. A.; Johnston, M. V.; Wexler, A. S. *Anal.Chem.* **1994,** *66*, 3681-87.

22. Gard, E.; Mayer, J. E.; Morrical, B. D.; Dienes, T.; Fergenson, D. P.; Prather, K. A. *Anal.Chem.* **1997,** *69*, 4083-91.

23. Zelenyuk, A.; Cabalo, J.; Baer, T.; Miller, R. E. *Anal.Chem.* **1999,** *71*, 1802-08.

24. Cabalo, J.; Zelenyuk, A.; Baer, T.; Miller, R. E. *Aerosol Sci.Technol.* **2000,** *33*, 3-19.

25. Morrical, B. D.; Fergenson, D. P.; Prather, K. A. *J.Am.Soc.Mass Spectrom.* **1998,** *9*, 1068-73.

26. Sykes, C.; Woods III, E.; Smith, G. D.; Baer, T.; Miller, R. E. *Anal.Chem.* **2001,** *73*, 2048-52.

27. Jayne, J. T.; Leard, D. C.; Zhang, X.; Davidovits, P.; Smith, K. A.; Kolb, C. E.; Worsnop, D. R. *Aerosol Sci.Technol.* **2000,** *33*, 49-70.

28. Hearn, J. D.; Smith, G. D. *Anal.Chem.* **2004,** *76*, 2820-26.

29. LaFranchi, B. W.; Zahardis, J.; Petrucci, G. A. *Rapid Comm.Mass.Spectr.* **2004,** *18*, 2517-21.

30. Jimenez, J. L.; Jayne, J. T.; Shi, Q.; Kolb, C. E.; Worsnop, D. R.; Yourshaw, I.; Seinfeld, J. H.; Flagan, R. C.; Zhang, X.; Smith, K. A.; Morris, J. W.; Davidovits, P. *J.Geophys.Res.* **2003,** *108*, SOS 13-1-SOS 13/13.

31. Nash, D. G.; Liu, X. F.; Mysak, E. R.; Baer, T. *Int.J.Mass Spectrom.* **2005,** *241*, 89-97.

32. Thompson, D. S.; Schein, M. E.; Murphy, D. M. *J.Aerosol Sci.* **2000,** *33*, 153-69.

33. Schwartz, J.; Dockery, D. W.; Neas, L. M. *J.Air Waste Manage.Assoc.* **1996,** *46*, 927-39.

34. Dockery, D. W.; Pope, C. A. I. *Ann.Rev.Public Health* **1994,** *15*, 107-32.

35. Dockery, D. W.; Pope, C. A. I.; Xu, X; Spengler, J. D.; Ware, J. H.; Fay, M. E.; Ferris, B. G.; Speizer, F. E. *New Engl.J.Med.* **1993,** *329*, 1753-59.

36. *Ultrafine Particles in the Atmosphere,* Imperial College Press: London, 2003.

37. Liu, P.; Ziemann, P. J.; Kittelson, D. B.; McMurry, P. H. *Aerosol Sci.Technol.* **1995,** *22*, 293-313.

38. Liu, P.; Ziemann, P. J.; Kittelson, D. B.; McMurry, P. H. *Aerosol Sci.Technol.* **1995,** *22*, 314-24.

39. Heimann, P.; Koike, K.; Hsu, C-W.; Blank, D.; Yang, X. M.; Lu, K. T.; Ng, C. Y.; Evans, M.; Suits, A. G.; Flaim, C.; Lee, Y. T.; Padmore, H. A. *Rev.Sci.Instrum.* **1997,** *68*, 1945-55.

40. *NIST Chemistry WebBook, NIST Standard Reference Database Number 69,* February 2000 ed.; National Institute of Standards and Technology: 2003.

41. Morris, J. W.; Davidovits, P.; Jayne, J. T.; Shi, Q.; Kolb, C. E.; Worsnop, D. R.; Barney, W. S.; Jimenez, J.; Cass, G. R. *Geophys.Res.Lett.* **2002,** *29* , 71-1-71/4.

42. McLafferty, F. W.; Turecek, F. *Interpretation of Mass Spectra,* 4 ed.; University Science Books: Sausalito, CA, 1993.

43. Zhang, Y.; Zhu, X.; Slanina, S.; Shao, M.; Zeng, L.; Hu, M.; Bergin, M.; Salmon, A. L. *Pure Appl.Chem.* **2004,** *76*, 1227-39.

44. Lee, J. H.; Kim, Y. P. Moon K.; Kim, H.; Lee C.B. *Atmos.Environ.* **2001,** *35*, 635-43.

45. Castanho, A. D. A; Artaxo, P. *Atmos.Environ.* **2001,** *35*, 4889-902.

46. Tolocka, M. P.; Solomon, P. A.; Mitchell, W.; Norris, G. A.; Gemmill, D. B.; Wiener, R. W.; Vanderpool, R. W.; Homolya, J. B.; Rice, J. *Aerosol Sci.Technol.* **2001,** *34*, 88-96.

47. Zhang, Q.; Canagaratna, M. R.; Jayne, J. T.; Worsnop, D. R.; Jimenez, J. *J.Geophys.Res.* **2005,** *110*, D07S09.

48. Kimura, K.; Katsumata, S.; Achiba, Y.; Yamazaki, T.; Iwata, S. *Handbook of He(I) Photoelectron Spectra of Fundamental Organic Molecules,* Halsted Press: New York, 1981.

49. Mautner, M.; Sieck, L. W. *Int.J.Mass Spectrom.Ion.Proc.* **1991,** *109*, 187-208.

50. Lias, S. G.; Ausloos, P. *J.Am.Chem.Soc.* **1978,** *100*, 6027-34.

51. Chupka, W. A. *J.Chem.Phys.* **1959,** *30*, 191-211.

52. Lifshitz, C. *Mass Spectrom.Rev.* **1982,** *1*, 309-48.

53. Wolff, B. E.; Wolff, G.; McCloskey, J. A. *Tetrahedron* **1966,** *22*, 3093-101.

54. Jang, M.; Kamens, R. M. *Atmos.Environ.* **1999,** *33*, 459-74.

55. Jaoui, M.; Kamens, R. M. *J.Atmos.Chem.* **2003,** *44*, 259-97.

56. Kuckelmann, U.; Warscheid, B.; Hoffmann, T. *Anal.Chem.* **2000,** *72*, 1905-12.

57. Yu, J.; Jeffries, H. E.; LeLacheur, R. M. *Environ.Sci.Technol.* **1995,** *29*, 1923-32.

CHAPTER 3:
Flowtube studies of α-pinene ozonolysis

3.1. Introduction

Volatile organic compounds (VOC) are emitted into the atmosphere from a variety of anthropogenic as well as biogenic sources. Anthropogenic sources include fossil fuel combustion, solvent use in industry and chemical processing, and have an estimated hydrocarbon flux of 100 TgC $year^{-1}$.[1] Biogenic emissions are estimated to be 1150 TgC $year^{-1}$, with their primary source being vegetation.[2,3] In regions such as the eastern portion of North America, estimates of biogenic hydrocarbon emissions can even surpass those of anthropogenic sources.[4] Increases in anthropogenic processes have been shown to increase tropospheric ozone levels,[5] which in turn oxidize many VOC's to generate low-volatility products.[3] These compounds partition from the gas phase into particle phase resulting in secondary organic aerosol (SOA) formation.

Approximately 11% of the global VOC budget is due to monoterpenes alone,[2] an important class of cyclic alkenes with a $C_{10}H_{16}$ molecular formula. Although monoterpene degradation by OH radical oxidation is more predominant than other pathways, the oxidation reaction with O_3[6] generates the lowest volatility products that contribute to SOA formation.[7,8] Although there is a wide variety of monoterpenes that contribute to SOA, significant emphasis has been placed on reactions involving α- and β-pinene. Monoterpene speciation

measurements indicate that these enantiomeric compounds make up a considerable portion of total global monoterpene emissions.[9]

Studies of pinene oxidation reactions have been performed with an array of various techniques, such as Fourier transform infrared spectroscopy (FTIR),[10] gas chromatography mass spectrometry (GC-MS) of either gas[11] or derivatized particle phase products,[12-16] liquid chromatography mass spectrometry (LC-MS),[17-19] atmospheric pressure chemical ionization mass spectrometry (APCIMS),[20] and electron impact (EI) mass spectrometry.[21] Modeling systems have also been effective.[22-25]

Despite extensive research efforts, however, the chemistry of monoterpene analysis remains rather unclear. It has been argued that the primary products of α-pinene ozonolysis, which were initially suspected of causing nucleation based on their low volatility, are insufficient explanations for nucleation.[13] Recent measurements aimed at elucidating information of potentially fragile secondary species have focused on the less destructive techniques of ESI and MALDI.[26-28] These results have suggested that a significant fraction of the SOA are composed of oligomers,[26,27] which perhaps facilitated nucleation and then persist in the particle through its lifetime.

Currently, a key subject of debate in α-pinene ozonolysis is the reaction mechanism. Work is now focused on identifying the oligomeric species observed in electrospray ionization (ESI) and matrix assisted laser desorption ionization (MALDI) studies, but by employing real-time techniques such as temperature controlled thermal desorption MS (TPTDMS),[29] photoionization aerosol MS (PIAMS) and nano-aerosol MS (NAMS).[30] Although these time-resolved on-line analytical techniques offer mechanistic information, they also cause fragmentation of the fragile organic products, thus complicating mass

spectrometric interpretation and obscuring definitive product assignment. The NAMS study has suggested that during the nucleation process, the molecules in the particle phase have progressively lower oxygen to carbon ratios and that the composition of particles may change rapidly during the nucleation process.[30]

Mechanistic studies have revealed that, after the initial oxidation of α-pinene by ozone, the primary ozonide rapidly decomposes into two excited Crigee intermediates (ECI). These ECI can then either decompose or stabilize to form a stabilized Crigee intermediate (SCI). After this initial degradation, two pathways are generally considered as potential channels for SOA formation. It has been suggested that particle formation occurs due to formation of secondary ozonides from SCI reaction with aldehydes or hydroperoxy esters through SCI-acid reactions.[13,24,31] Evidence of this pathway includes decreased particle formation by adding water and other low molecular weight SCI scavengers. On the contrary, formation of low volatility peroxidic oligomers through the hydroperoxide channel has also been suggested.[29] Studies using TPTDMS have shown that peroxyhemiacetals can be formed by heterogeneous reaction between aldehydes and hydroperoxides,[32,33] reactions which are suggested to be paramount in pinene ozonolysis as well.[29]

Because of the persistent problems with the analysis of fragile ions, we have undertaken this study of the α-pinene ozonolysis with our photoionization mass spectrometric experiment in which the photon energy from the synchrotron can be tuned to minimize ion fragmentation.[34,35] The use of fixed energy vacuum UV light at both 10.5 eV[36,37] and at 8.8 eV[38] have shown that ion fragmentation can be minimized. The unique aspect of this instrument is that it uses undulator radiation from a synchrotron, which is easily

tunable, quasi-coherent, extremely bright and intense, and which is in the energy range of the ionization potential of most atmospherically relevant organic species.

The three main focuses of this time-resolved flow tube study of the α-pinene - ozone study are the examination of the effect of relative humidity (RH), OH scavenger concentration, and reaction time on the aerosol production rate and composition. By varying the amount of H_2O available in the system, it was possible to probe the effect of scavenging the SCI by H_2O. Such SCI scavenging prevents reaction between SCI and any other species. Secondly, using an OH radical scavenger that also scavenges the SCI disrupts both oxidative pathways for α-pinene. The combination of these two experiments yielded information on nucleation and SOA mass formation.

3.2. Experimental

3.2.1. Flowtube setup

Reactions between a-pinene and O_3 were carried out at atmospheric pressure and room temperature (298 $\pm$1 K) in a 1.1 m Pyrex flowtube system with an inner diameter of 25.4 mm. A 4.3 mm inner diameter moveable Pyrex injector could be translated along the axis of the flowtube (Figure 3.1). The reaction time was controlled by the volumetric flowrate of the gases in the flowtube and the position of the moveable injector. The flowrates were chosen to ensure laminar flow with Reynolds numbers in the range of 48 to 127. On the other hand, rapid mixing of the gases was essential for investigating the initial stages of the reaction. A mixing "turbulizer" was designed (inset Figure 3.1) to ensure rapid mixing (0.2 – 0.5 s) of the two flows while minimizing gas residence times inside the device. Despite efforts, turbulence at very short distances could not be completely eliminated,

therefore data obtained within the first 4 cm was not included in the analysis. Particle formation and growth were monitored at the exit of the flowtube, which had an overall volumetric flow ranging between 0.8 - 2.1 L min^{-1} corresponding to linear flowrates ranging between 2.7 – 7.0 cm s^{-1}. The flowtube was sampled at its exit by both the VUV-AMS (0.27 L min^{-1}) and the Scanning Mobility Particle Sizer (SMPS) (0.24 L min^{-1}) systems, and the excess flow was continuously monitored by a flowmeter (model 4140 TSI) and exhausted.

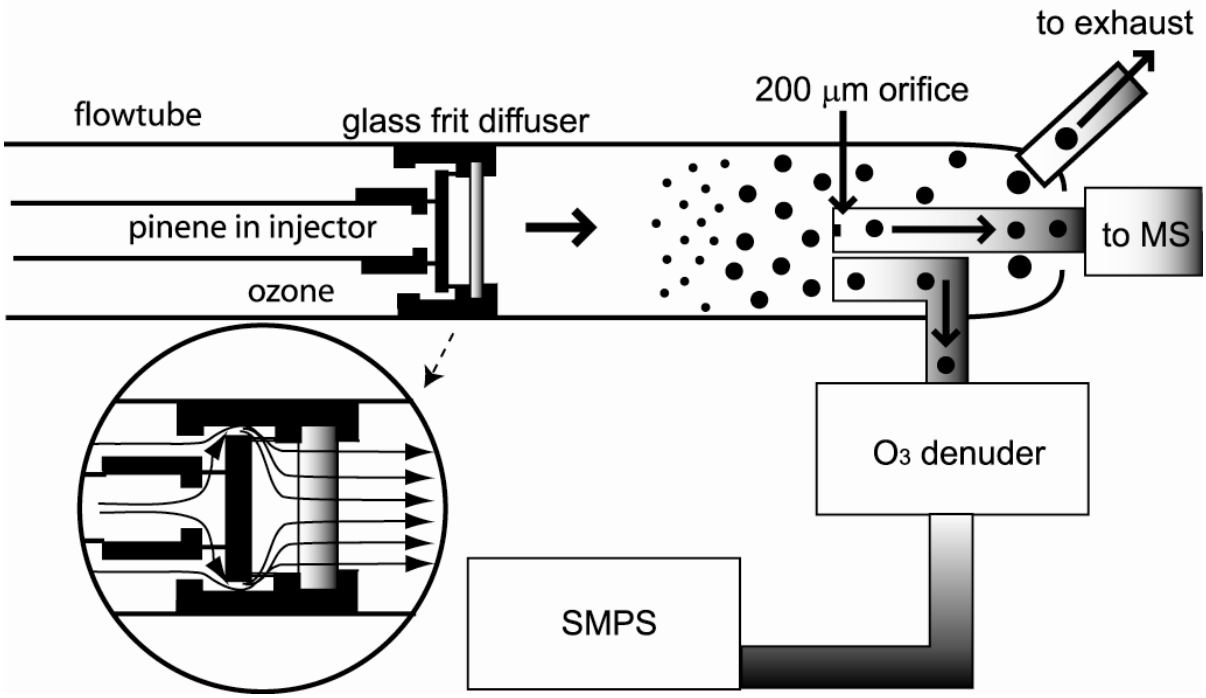

Figure 3.114. Flowtube schematic **Inset.** Diffuser

Reaction was stopped when the flow entered both the sampling lines (Figure 3.1) of the VUV-AMS because the pressure dropped from 760 to 3 Torr, and the SMPS because the ozone denuder was located sufficiently close to quench the reaction after 0.8 s.

3.2.2. Ozonolysis experiments

The dry nitrogen (RH < 5%) used as the carrier gas had no detectable particles as measured with the SMPS system. The equally dry oxygen used for making O_3 and the nitrogen flows were controlled by eight Mass-Flo Controllers (type 1179A MKS Instruments,

Inc.) programmed through a Multichannel Gas Flow and Pressure Controller (model 647C 8R1N MKS Instruments, Inc.).

For the case of high flows rates, ozone was produced by sending a 39:1 mixture of dry nitrogen and oxygen into a commercial O_3 generator (model OL80 Ozone Services, Yanco Industries Ltd.) that uses a corona discharge to generate O_3. For lower O_3 concentrations, the 254 nm light from a mercury lamp (model SCT-1 Ultraviolet Products, Inc.) illuminated a 10:1 mixture of dry nitrogen and oxygen. The $O_3/N_2/O_2$ mixture, further diluted as necessary, was sent into the sheath flow of the flowtube through Teflon tubing. The O_3 concentration was measured through the flow tube via Teflon tubing in the absence of α-pinene by a commercial O_3 monitor (model 202M Version 6.1 2B Technologies, Inc.). The O_3 concentrations ranged from 51.6 - 2682 ppb. However, concentrations below about 180 ppb resulted in such slow nucleation rates that the particle concentrations were not detectable with the VUV-AMS.

(±) α-Pinene (TCI America) vapor was produced by bubbling 83 cm^3 min^{-1} of dry nitrogen through liquid α-pinene. The vapor exiting the α-pinene bubbler was assumed to be saturated, giving a mixing ratio of 5.7 parts per thousand, which was further diluted with additional nitrogen in the ratio of 1:6.22, and mixed in a 30 ft Polyflo® coil. This α-pinene/nitrogen mixture was sent via flow controllers into the flow tube where the final concentration in the flow tube ranged between 38 – 93 ppm. There was no independent method of measuring α-pinene concentration in the flowtube, thus the values reported here are upper limits assuming that the dry nitrogen bubbled through the α-pinene liquid was fully saturated. Concentrations of both reactants are in the range of values used by other studies of the same reaction [13,30,31,39].

In experiments exploring RH effects on α-pinene ozonolysis, the water vapor content in the flowtube was controlled by mixing dry and wet nitrogen at various ratios. Wet nitrogen was made by flowing dry nitrogen through a bubbler of water. RH amounts in the range of < 5 % - 45% were measured at the exit of the flow tube in the absence of O_3.

The effect of the radical scavenger isopropanol on α-pinene ozonolysis was also examined by bubbling nitrogen through the isopropanol liquid. Concentrations of isopropanol ranged between $0 – 10^3$ ppm.

SOA mass at various residence times and under various reaction conditions (initial O_3 concentrations, RH, etc.) can be determined by using two different analysis tools; particle mass concentration as measured with the SMPS and total ion current as measured with the VUV-AMS. A range of initial conditions are summarized in Table 3.1. Depending on the combination of injector and sheath flows used, the range of gas residence time in the flowtube was 1 – 30 s.

a-pinene concentration (ppm) (upper limit)	O_3 concentration (ppb)	RH Dry < %5 Wet ~ 45 %	t_{rxn} total (s)
38.2	2682	dry	12.3
38.2	2682	wet	12.3
43.6	2682	dry	12.3
43.6	2682	wet	12.3
89.1	178.5	dry	28.7
93.1	220.0	dry	28.7
93.1	193.9	dry	28.7

Table 3.1. Initial reaction conditions.

All connections leading to the flowtube were either Teflon or Polyflo®, and the connection from the flowtube to the SMPS was made with conductive silicone tubing (TSI).

3.2.3. Particle analysis methods

3.2.3.1. Apparatus

A detailed description of the synchrotron based vacuum ultraviolet aerosol mass spectrometer (VUV-AMS) has been provided elsewhere [34,35]. Briefly, particles are sampled into the VUV-AMS through a 200 μm i.d. flow-limiting aperture at 0.27L min^{-1}. Particles of various diameters are focused into a narrow, low divergence beam by a 30 cm long aerodynamic lens system[40,41] terminated by a 3 mm aperture, which accelerates them into the first differentially pumped chamber. The particle beam enters a second stage of differential pumping through a 2 mm diameter skimmer and into the final detection chamber through a 4mm skimmer. The particles reaching the experimental chamber impinge on a 3 mm copper heater tip located equidistant between the repeller and accelerator grids. Although the heater temperatures could be adjusted between 373 – 723 K, all experiments in this study were in the range of 398 – 423 K. The optimal ion signal was achieved when the tip was approximately 3 mm from the ionization axis where tunable and quasi-continuous VUV light ionized the gas plume expanding back from the heater tip. The 3 mm distance is a compromise between maximizing the vapor density being ionized and minimizing the electrical field interference caused by the tip between the high voltage extraction plates.

The photon beam is produced by an undulator at the Chemical Dynamics Beamline at the Advanced Light Source (ALS, Lawrence Berkeley National Laboratory), which delivers 10^{16} photons s^{-1} VUV light in the wavelength range of 7 - 25 eV (2.5% spectral bandwidth). Although many photon energies were used during the course of these experiments, most of the useful data were collected at 10.5 eV, where the amount of fragmentation was not excessive and the signal was high.

Ions are extracted by ion time-of-flight (TOF) optics (Figure 3.2), consisting of three equally spaced grids; a repeller, accelerator, and the entrance to the grounded flight tube separated by 1.6 cm each. A 3.55 kV bias is applied to the repeller, accelerator, and heater. Ion TOF collection is initiated by a 4.7 μs pulse of 0.57 kV and 0.25 kV applied to the repeller and heater respectively. Ions are collected at 30 kHz by dual chevron microchannel plates (MCP) held at -1.86 kV and located 5 cm beyond the end of the drift region of the MS. Ion signal from the MCPs are amplified by a negative mode fast preamplifier and TOF mass spectra are recorded by a multichannel scaler with a 4 ns bin width and averaged over 262144 (2^{18}) to 2097152 (2^{21}) sweeps. A typical collection time was 30 s. In this configuration, the mass resolution at *m/z* 169 is $m/\Delta m = 494$.

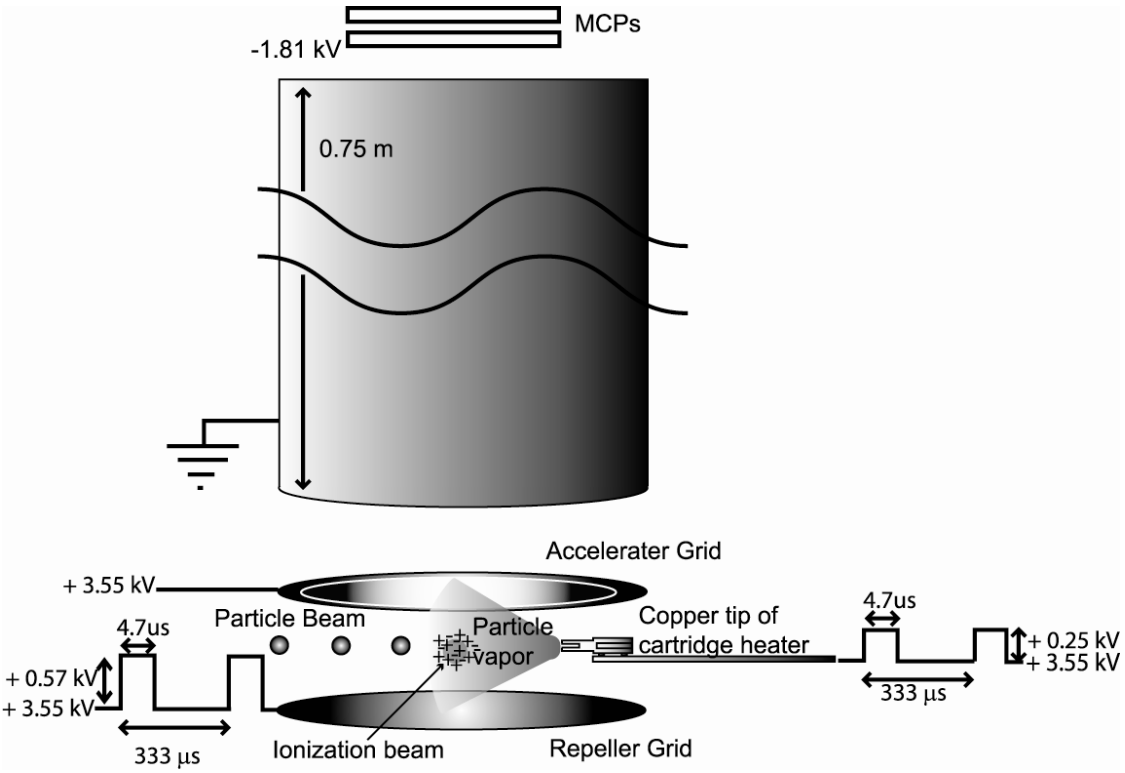

Figure 3.2. The ionization region of the time of flight mass spectrometer. The ions were extracted by a 30 kHz pulsed field.

3.2.3.2. Scanning Mobility Particle Sizer (SMPS)

The SMPS (model 3986 TSI, Inc.) was used to measure the particle number concentration and mobility diameters. The aerosol was first directed into an Electrostatic Classifier (model 3080 TSI, Inc.) containing an impactor to remove large particles (0.071cm orifice), a ^{85}Kr neutralizer for charge equilibration of the particles, and a Nano Differential Mobility Analyzer (NDMA) (model 3085 TSI, Inc.) to analyze electrostatic mobility diameters. The aerosol then went directly into an Ultrafine Condensation Particle Counter (CPC) (model 3025A TSI, Inc.) that reported particle number concentrations as a function of particle mobility diameter. The lower and upper size limits of the SMPS are 2nm and 500 nm, respectively.

3.2.4. Standards

Two known products of α-pinene ozonolysis, pinic acid (Sigma Aldrich Library of Rare Chemicals) and *cis*-pinonic acid (Aldrich), were analyzed with the VUV-AMS so that fragmentation patterns as a function of photon energy and heater temperature could be examined. For both compounds, the solids were dissolved in a 10:1 water isopropanol mixture and atomized by a Constant Output Atomizer (TSI, Inc. Model 3076**.** Polydispersed, wet, and charged particles exit the atomizer and are carried by a 1 L min^{-1} nitrogen flow to a heated stainless steel rod (383 K). The aerosol was then dried by a 1 m home-constructed diffusion dryer filled with color indicating silica gel (EMD Chemicals, Inc.) and sent to the VUV-AMS.

3.3. Results and discussion

3.3.1. Mass spectrometric analysis of aerosol products

Figure 3.3 shows a typical VUV-AMS mass spectrum of the aerosol products of α-pinene ozonolysis with a total mass concentration of 5020 μg m^{-3}. We estimate that the detection limit of our mass spectrometer is about 10.4 μg m^{-3}. In real-time analysis, the VUV-AMS total ion current varies linearly with the total particle mass concentration as measured by the SMPS (Figure 3.4). The VUV-AMS is unbiased with respect to different particle sizes above mean particle diameter of approximately 25 nm, so that we can be confident that the instrument is linear with respect to the aerosol mass concentration.

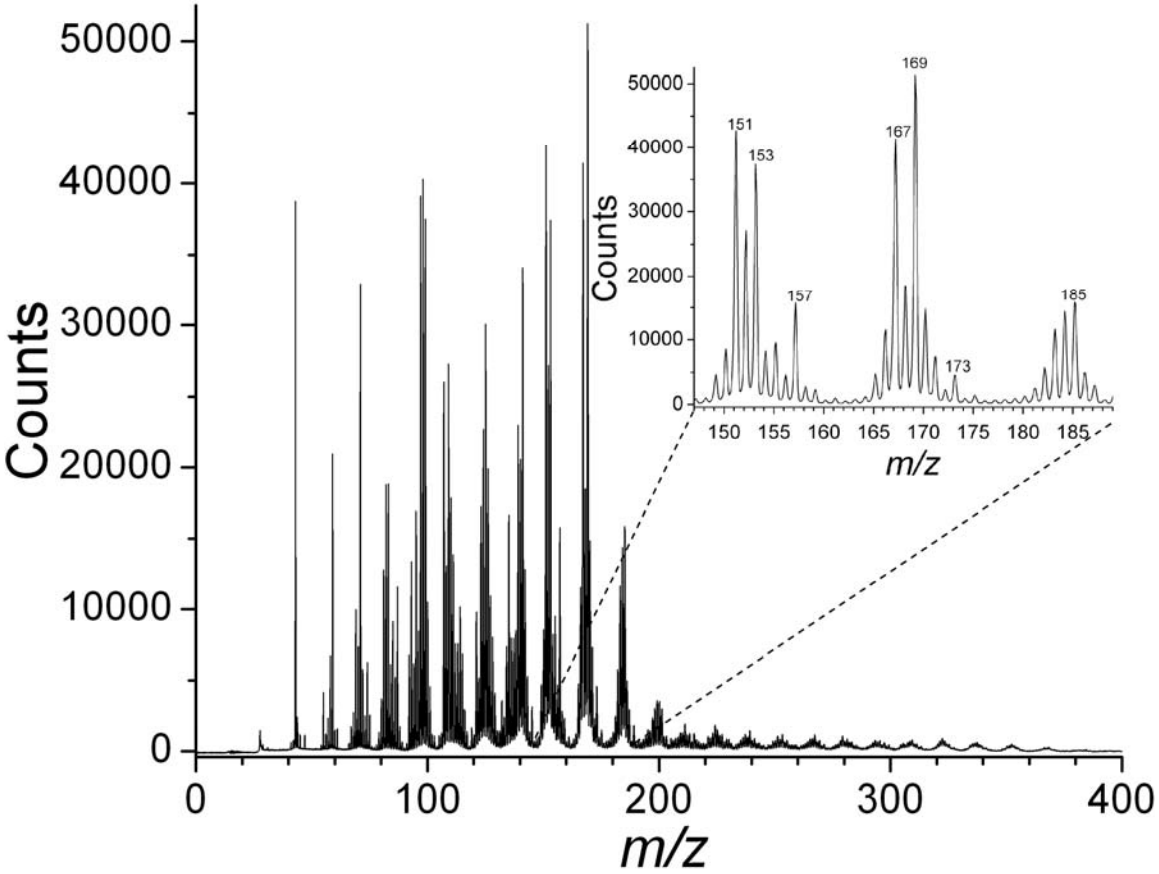

Figure 3.3.a) A typical spectrum of a-pinene ozonolysis products. The higher intensity ions are < 200 m/z and are predominately odd numbered, whereas above m/z 200, ions are predominately even. **b)** There is a mass resolved at every m/z. As an example, the region between *m/z* ~150-190 is blown up.

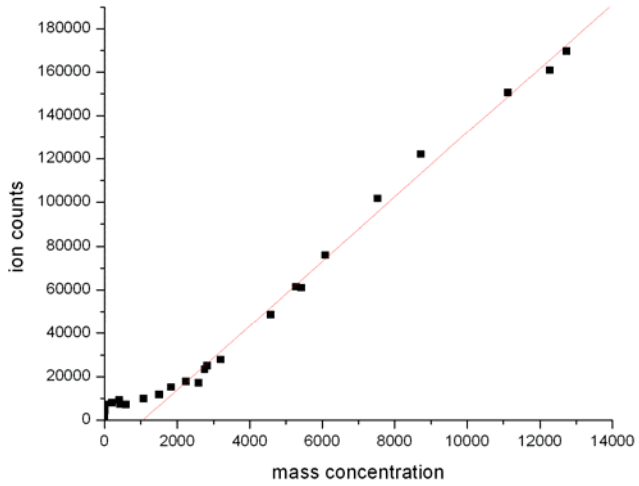

Figure 3.4. Linear correlation between total ion current and mass concentration of α-pinene ozonolysis products.

3.3.1.1. Photoionization efficiency (PIE)

A notable feature in the α-pinene ozonolysis product spectra (Figure 3.3) is that mass peaks below *m/z* 200 are dominated by odd *m/z* ions. Furthermore, the intensity drops precipitously past the *m/z* 185 region of the mass spectrum. This mass also corresponds to the adduct of α-pinene and ozone (*m/z* 184). The *m/z* 43 - 200 region of the mass spectrum is dominated by odd *m/z* ions, whereas above *m/z* 200 more even *m/z* ions begin to appear, and the dominant ions greater than *m/z* 300 are almost exclusively even *m/z* ions.

The overwhelming number of product peaks in Figure 3.3 prompts the question; why are there so many product peaks? Could these detected peaks simply be molecular ion species or are they a combination of parent and daughter ions of α-pinene ozonolysis products? Because all stable compounds consisting of C, H, and O atoms have even masses, and because no nitrogen containing compounds are expected among these α-pinene ozonolysis products, we can associate all odd mass peaks with fragment ions produced in the

photoionization process. The even mass ions could be molecular ions or fragment ions created as a result of the ionization process. Molecular decomposition typically occurs in a higher temperature environment (likely in the aerosol plume) and results in stable even electron products. Upon ionization, these even electron products yield odd electron, even *m/z* ions. In contrast, dissociative ionization occurs in environments with greater mean free paths and generally leads to even electron, odd *m/z* ions.

The heater temperature (generally close to 400 K) used to vaporize the samples has very little effect on the fragmentation patterns, thus demonstrating that the fragment ion peaks originate by dissociative photoionization rather than at the heater by pyrolysis into neutral fragments. This conclusion is different from that of Ziemann and coworkers,[29] who used temperature programmed thermal desorption (TPTD) of terpene ozonolysis products in order to selectively vaporize fractions according to their volatility. Apparently, the sudden impact of our aerosol particles on the hot heater imparts less thermal energy than the prolonged heating in the TPTD experiment.

Clues to the content of our mass spectrum can be obtained by analyzing the photoionization mass spectra of two known products of α-pinene ozonolysis, *cis*-pinonic acid and pinic acid.[14] Figure 3.5 shows the photoionization efficiency (PIE) scan of the three dominant mass peaks of *cis*-pinonic acid as a function of the ionization energy up to hν = 10.5 eV. We can determine an ionization energy, IE, of 8.97 $\pm$ 0.06 eV and appearance energies close to 9 eV for daughter ions, *m/z* 166, 125, 114, and 98. As the insert in Figure 3.5 demonstrates, the MS of *cis*-pinonic acid at 10.5 eV exhibits significant fragmentation of

ions of *m/z* 166 (H_2O loss), *m/z* 125 ($C_2H_3O_2$ loss), *m/z* 114(C_4H_6O loss) and *m/z* 98 ($C_4H_6O_2$ loss).

A second established product of a-pinene ozonolysis, pinic acid (*m/z* 186), was analyzed in the same way and the same behavior of the parent and daughter ions was observed from its PIE curve. All of the high intensity fragments were even *m/z* ions, a characteristic common for organic acid photoionization as described in our previous work;[35] *m/z* 168 (H_2O loss), *m/z* 140 (CH_2O_2 loss), *m/z* 114 ($C_3H_4O_2$ loss), and 100 ($C_4H_6O_2$ loss). These two examples demonstrate that in the α-pinene ozonolysis product spectra not only are all of the odd mass ions a result of fragmentation, but that a large fraction of ions in the product spectra is a result of dissociative photoionization. It furthermore suggests that aldehydes, which yield odd massed ions upon ionization[42] are perhaps more abundant than acid products.

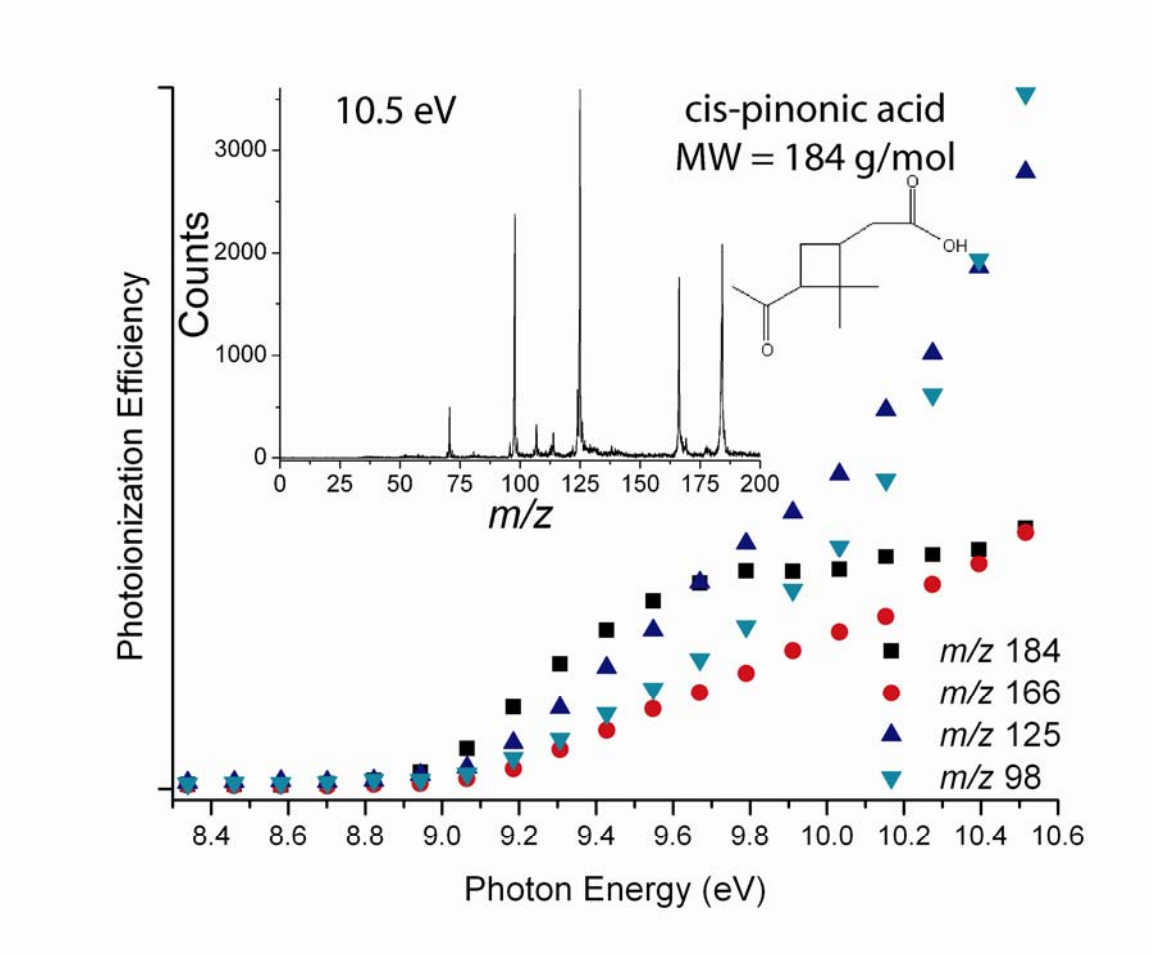

Figure 3.5. PIE scans of *cis*-pinonic acid at a heater temperature of 398 K. The parent ion (*m/z* 184) as well as the experimentally determined IP of *cis*-pinonic acid is ~ 9.0 eV and the three daughter ions have AEs between ~ 9.0 and 9.1 eV. Once the molecular ion is visible in the MS, all three daughter ions are as well. Dissociation of *cis*-pinonic acid is facile presumably because of the ring structure. I**nset.** Structure of *cis*-pinonic acid MW 184 g mol^{-1} and *cis*-pinonic acid at 10.5 eV (photon energy used for most analyses).

An attempt was made to choose a photon energy that would minimize the fragmentation. However, the ion peaks over the entire range of masses from *m/z* 43-400 begin to appear almost simultaneously at 9.1 eV. As in the case of *cis*-pinonic acid and pinic acid, the daughter ions of almost all of the SOA reaction products have appearance energies very similar to the ionization energies of their parent ions. This property is quite different from the PIE spectra of molecules such as α-pinene, oleic acid, and cholesterol, which have stable parent ions, and whose photoionization mass spectra at low photon energies exhibit

only the parent mass peak. Apparently, the ozonolysis products have corresponding ions that are very unstable.

Even if we accept that there are several fragment peaks per product molecule in the α-pinene ozonolysis, the number of peaks is still overwhelming. The mass resolution of our VUV-AMS allows us to detect one resolved peak at every *m/z* between 43 and 402 (Figure 3.3). In addition, it is nearly certain that any given peak, such as *m/z* 182, is a combination of several ions such as $C_{13}H_{26}^+$, $C_{12}H_{22}O^+$, $C_{11}H_{18}O_2^+$, and $C_{10}H_{14}O_3^+$, …, which have the same nominal mass, but different exact masses. Clearly, much higher resolution mass spectra would reveal three or four times as many peaks, and would perhaps be achievable with either an orthogonal reflectron TOF (RETOF) or a Fourier transform ion cyclotron resonance mass spectrometer (FT-ICR). If we conservatively estimate that each product has 4 fragments and that each peak represents 3 fragments (see for example Ziemann et al.[29] who detect 4-6 maxima per single *m/z* ion with TPTD), the quantity of our peaks suggests ~ 100 different products in the particle phase resulting from α-pinene ozonolysis. In addition, the complex fragmentation patterns of 'clumps' found even in the high mass ranges (*m/z* > 300) suggest that a wide variety of precursors combine in various combinations to yield a wide array of complex, multifunctional products.

3.3.1.2. Time resolved experiments

Experimental conditions for the various runs are summarized in Table 3.1. Some reaction conditions differ only in the initial concentrations of α-pinene or O_3. As expected, decreasing either of the initial reactant concentrations yields a proportional decrease in total ion signal, geometric mean diameter (GMD), as well as number and mass concentration (see for example, inset of Figure 3.6). In addition, the induction time for particle generation also

varies with reactant concentration. Illustrated in Figure 3.6 are examples of product signals as a function of time where the limiting species, ozone, has an initial concentration of 4.75 * 10^{12} molecules cm^{-3}. This time resolved experiment shows that initially, nucleation dominates as gas-phase products continue to build up. Once the particle number has reached some maximum concentration at a reaction time of about 12 s (Figure 3.6), the system has become limited by the two simultaneous processes of accumulation (condensation of gas-phase products onto pre-existing particles) and coagulation (particles collide with one another to form larger particles). Coagulation, which begins to occur after the initial nucleation, becomes a more important process after the initial number concentration decreases by half ($\tau_{1/2}$). Under these experimental conditions, $\tau_{1/2}$ is calculated to be ~70 s. Furthermore, the coagulation of particles causes an increase in the GMD of the particles, as does the accumulation process (Figure 3.6). The corresponding mass concentration increases linearly (inset of Figure 3.6), and assuming particle density of 1 g cm^{-3}, reaches approximately 6 mg m^{-3} in 28 s of reaction time.

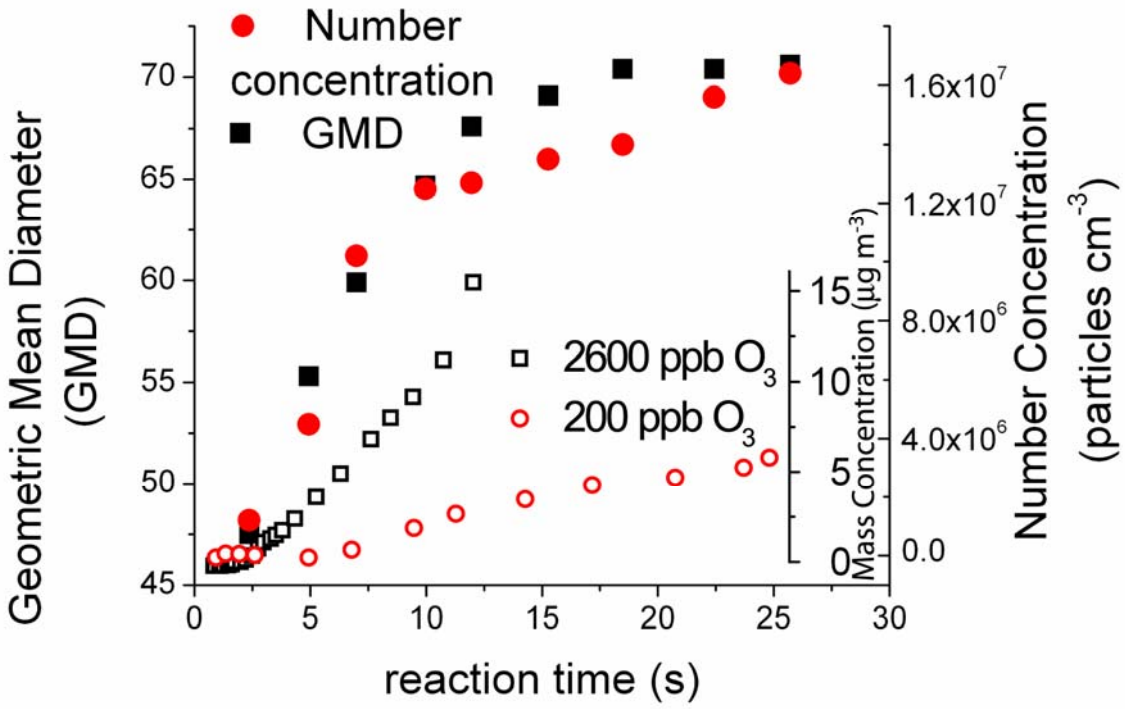

Figure 3.15. a) Geometric mean diameter (GMD) and number concentration as a function of reaction time for initial reaction condition 200 ppb O_3. Number concentration shows an initial burst at the nucleation event and then levels off at around 1.5 * 10^7 particles cm^{-3}. I**nset.** Mass concentration as a function of reaction time for different initial O_3 concentrations.

Although the gross features of the mass spectra did not change significantly with reaction time, clear variations were observed when particular mass peaks were monitored in terms of their relative rate of production. Figure 3.7 illustrates the time evolution up to16 s for the 200 ppb O_3 concentration run. The variations were quantified as fractional relative rates of production:

$$\text{Relative Rate of Production} = \frac{(\text{Fractional Area of Peak A})_t - (\text{Fractional Area of Peak A})_{t-1}}{\Delta t}$$

where 'Fractional Area of Peak A' represents the area of a specified peak normalized by the total ion current at reaction time, *t*.

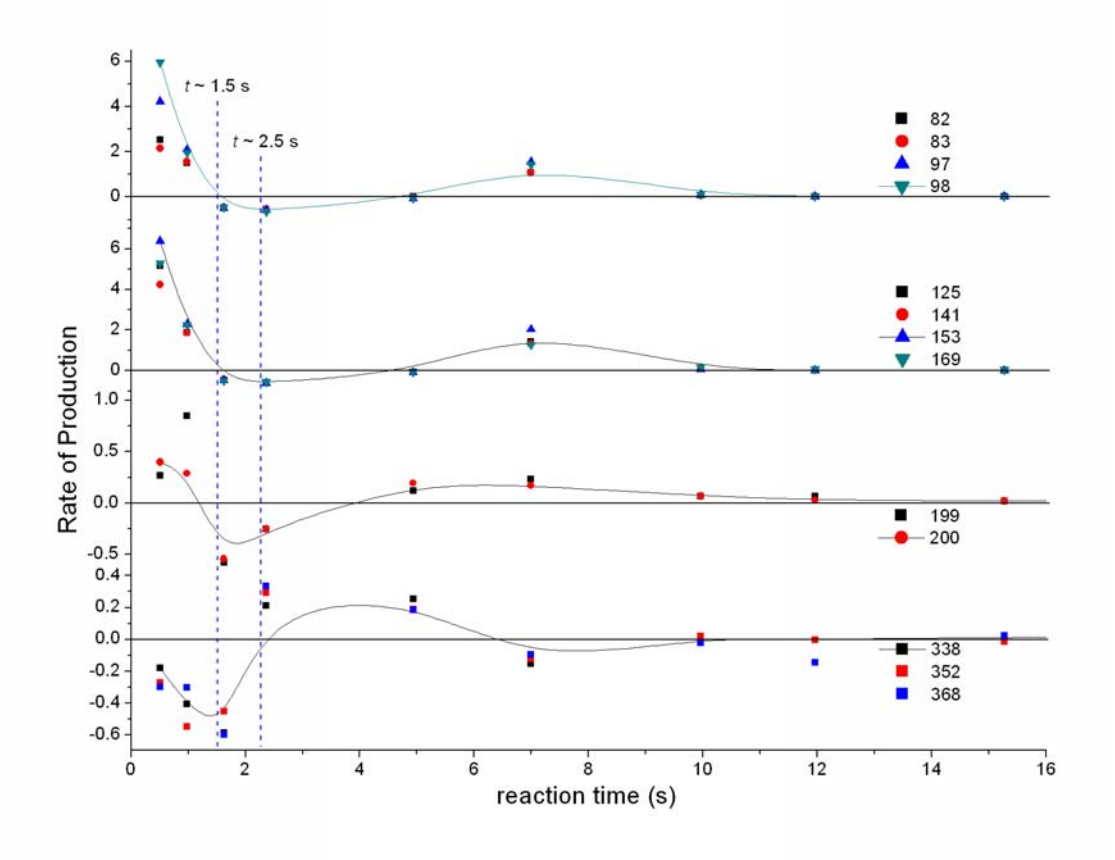

Figure 3.7. Relative rate of product formation. The lines are not fitted; they are merely guides.

As shown in Figure 3.7, at 1.5 s reaction time ($t \sim 1.5$ s), the smallest ions (i.e. *m/z* 71, 82, 83, 97, and 98) and the mid-range ions (i.e. *m/z* 125, 141, 153, 169, 199, and 200), which we assume are markers for smaller and mid-range sized molecules, outpace the production of the large molecular weight species (i.e. *m/z* 338, 352, 368). On the other hand, the small molecules cannot condense unless there are nuclei consisting of high molecular weight (MW) species. That is, even though the smaller species may be produced initially in the reaction, they will remain in the gas phase until there is a particle surface available for condensation. Evidently, the nuclei formation takes place at times less than 1 second. Indeed, the relative rate of production of the high MW molecules in Figure 3.7 shows that its yield is poised to go positive at times less than 1 second. But, this takes place at times too short for us to

measure. What is interesting is that the large molecules necessary for particle formation are very rapidly overwhelmed by the high quantities of the smaller species that partition into the particle.

At longer reaction times the relative rates reverse direction so that at 2.5 s the growth rate of the larger *m/z* ions outpaces those of the lower mass species. The highest rate of production of the high mass ions (*m/z* 338, 352, 368…) and the lowest rate of production of the lower mass species (*m/z* < 169) occurs, in fact, at $t \sim 2.5$ s. This reversal in the relative rates of production of the smaller and higher *m/z* ions (Figure 3.7) likely produces molecules rather than radicals because of the predominance of even *m/z* numbers in this high *m/z* range, i.e. 322, 338, 352, 366, 368, 384, 390, 392, 394, 398, 400 and 402. There are several explanations for the observed results. It is possible that during this phase of the reaction, the species represented by the smaller *m/z* ions undergo heterogeneous reaction with the pre-existing particles, which results in increased production of high MW species. In fact this observation may be a confirmation of the proposal by Jang and Kamens[43] who predicted that their observed increase in SOA yield is caused by heterogeneous reactions between gas-phase species such as glyoxal and polycarbonyl compounds with liquid phase species. Others have also found growth of aerosol particles due to reactive uptake of gas-phase glyoxal by species already in the particle phase,[21,44] stressing the importance of heterogeneous chemistry in the gas-to-particle transition. Photoionization MS experiments comparable to the one presented in this manuscript were performed by Johnston and co-workers[30] and led them to postulate alternative routes of formation of high *m/z* products. They suggested that nucleation species were formed via the SCI channel and involved the addition and/or subtraction of small oxygenated species:

$$SCI + H_2O - H_2O_2 \longrightarrow \text{pinonaldehyde} \quad (\text{product MW} = 168) \qquad (R1a)$$

$$SCI + \text{pinonaldehyde} \longrightarrow \text{secondary ozonide} \quad (\text{product MW} = 352) \qquad (R1b)$$

$$SCI + SCI + H_2O \quad (\text{product MW} = 386) \qquad (R2)$$

These predictions are entirely consistent with our observations (Figure 3.7) of small *m/z* ions being adsorbed/absorbed into the particle once a nucleus of high mass products is formed. Kamens and Lee predict similar routes based on SCI scavenger experiments, vapor pressure estimations, and model simulations. They implicate the SCI (MW = 186) in the nucleation process, suggesting that it reacts with pinonaldehyde and *cis*-pinonic acid to produce nucleating agents, see R1 and R3.[13]

$$SCI + \text{pinonic acid} \quad (\text{product MW} = 368) \qquad (R3)$$

Alternatively, our results may be evidence of polymerization mechanisms that would increase quantities of the larger molecules in the 300+ *m/z* range. Polymerization reactions would likely be dimerization via aldol condensation or *gem*-diol formation. Such dimerization reaction schemes involving pinonaldehyde (MW = 168) (Scheme 3.1):

$$\text{pionaldehyde} + \text{pinonaldehyde} \longrightarrow \text{dimer} \quad (\text{product MW} = 336) \qquad (R4)$$

or 10-hydroxy-pinonaldehyde (MW = 184) have been suggested by numerous ESI and MALDI studies[26,27,45] and hypothesized based on increased oligomeric formation in the presence of acidic seed particles or acidic environments.[27,46,47]

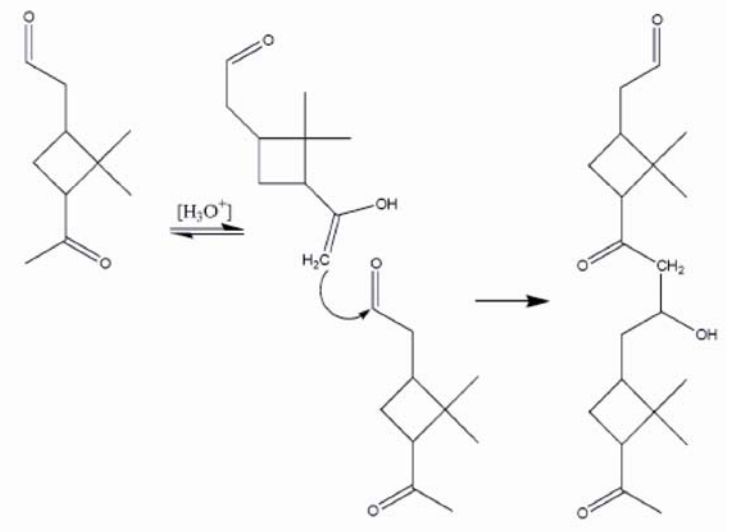

Scheme 3.1. Dimerization of pinonaldehyde (MW = 168 g mol^{-1}) by aldol condensation reaction to produce MW = 336.

Routes leading to nucleating species may instead involve the hydroperoxide channel, in which case the nucleating species would be peroxidic oligomers that have been measured in laboratory studies[32,33,45] and predicted in modeling studies.[23] In this case, larger involatile hydroperoxides formed from consecutive HO_2-RO_2 and RO_2-RO_2 reactions heterogeneously react with aldehydes to form large MW peroxyhemiacetals in the 300-400 *m/z* range. [29] Aldehydes are predicted to readily undergo reaction with hydroperoxide products, for example, $C_{10}H_{16}O_4$, predicted by modeling studies[23]:

$$\text{pinonaldehyde} + \text{HOO-}C_{10}H_{15}O_2 \quad (\text{product MW} = 368) \qquad \text{(R5)}$$

Such reactions yield products in the molecular weight range of *m/z* 300-400. It is possible that once products of such reactions are formed, they may undergo a Bayer Villiger type rearrangement[48] to form an alcohol and ester (from ketones) and a carboxylic acid and alcohol (from aldehydes) (Scheme 3.2). Owing to the uncertainty of the timescale of the rearrangement, it is unclear if large mass products formed from hydroperoxide and aldehyde or acid reaction will be detected in our set-up.

Finally, our results in Figure 3.7 demonstrate that after the first 10 s of reaction time, the relative rate of production of all molecules goes to zero, which means that all products grow at the same rate.

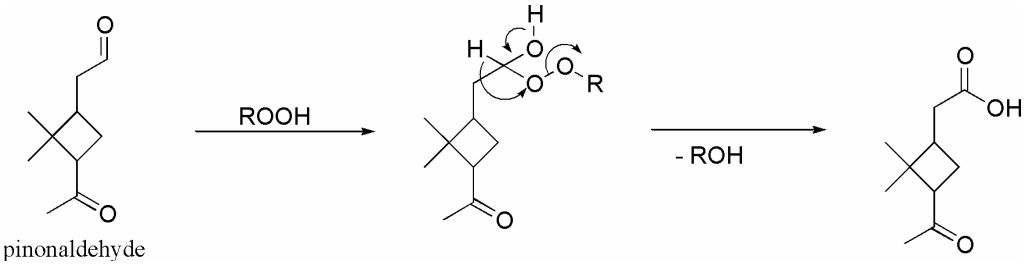

Scheme 3.2. Baeyer Villiger oxidation of an aldehyde.

3.3.1.3. Effect of SCI scavenger

The SCI channel has been proposed based on the reduction of particle number by water and other low-molecular weight compounds.[13,24,31,49] In the current study, the impact of water vapor was examined with respect to change in composition and change in particle number and size. Figure 3.8 shows distinct evidence that the presence of water vapor (RH ~ 45 %) decreased the induction time for particle nucleation. Furthermore, the mass spectral data showed greater total ion current at shorter induction times with higher RH conditions. Since water vapor only effects the SCI channel, and considering the faster nucleation with increased water vapor, it seems that SCIs and water must play a crucial role in new particle formation. Therefore, although 30 nm particles formed in wet or dry conditions are compositionally identical, the reaction time required to make them is shorter in the presence of more water vapor.

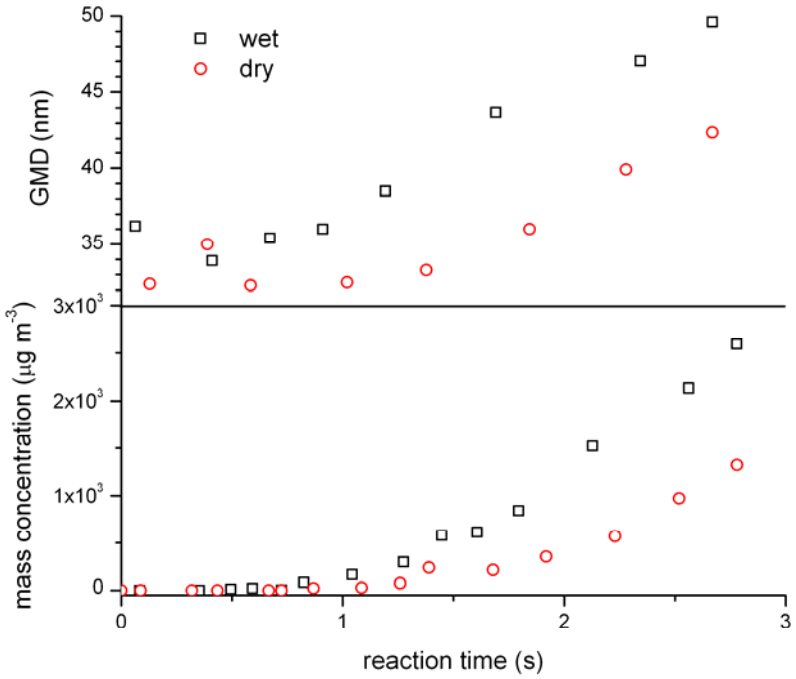

Figure 3.8. Mass concentration and GMD during the first three seconds of reaction. Notice profiles/slopes look same for wet and dry, but everything is shifted towards a shorter induction period with increased RH; (■)wet RH < 5 % (●) dry RH ~ 45 %.

A possible explanation for these observations is that water is involved by end-capping the exposed radicals after a self-reaction of the SCI to form a linear peroxidic species or a cyclic dimer, 1,2,4,5-tetraoxane (Scheme 3.3).[30,50,51] Recent work by Rimmer and coworkers[50,51] has shown clear evidence for the formation of both cyclic and linear oligomerization (up to 19 units) from alkene ozonolysis. Additionally, they determined that the main product depended on the amount of water vapor available for reaction; cyclic oligomers dominated in anhydrous conditions and open chain linear oligomers under wetter conditions. This observation confirmed that chain termination of propagating open chain polymers can occur through reaction with either water or hydrogen peroxide.[51] Interestingly, a similar mechanism in our reaction would yield an SCI dimer terminated with hydrogen

peroxide (MW 402 g mol^{-1}) (Scheme 3.3), which is the highest resolved peak in our spectra. Likewise, end capping with water would result in a product with MW 386 g mol^{-1}, with elimination of hydrogen peroxide producing a compound with MW 352 g mol^{-1}. Both of these ions are present in the mass spectra, though definitive peak identification remains uncertain.

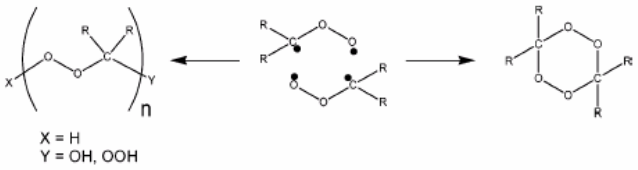

Scheme 3.3. Self reaction of the SCI to form a linear peroxidic species capped by the addition of water or hydrogen peroxide.

In contrast, at longer reaction timescales, RH does not affect the aerosol mass yield and both particle profiles seem to track one another quite closely (Figure 3.9). Additionally, mass spectral analysis shows that at longer reaction times, the high and low RH products are compositionally identical (Figure 3.10).

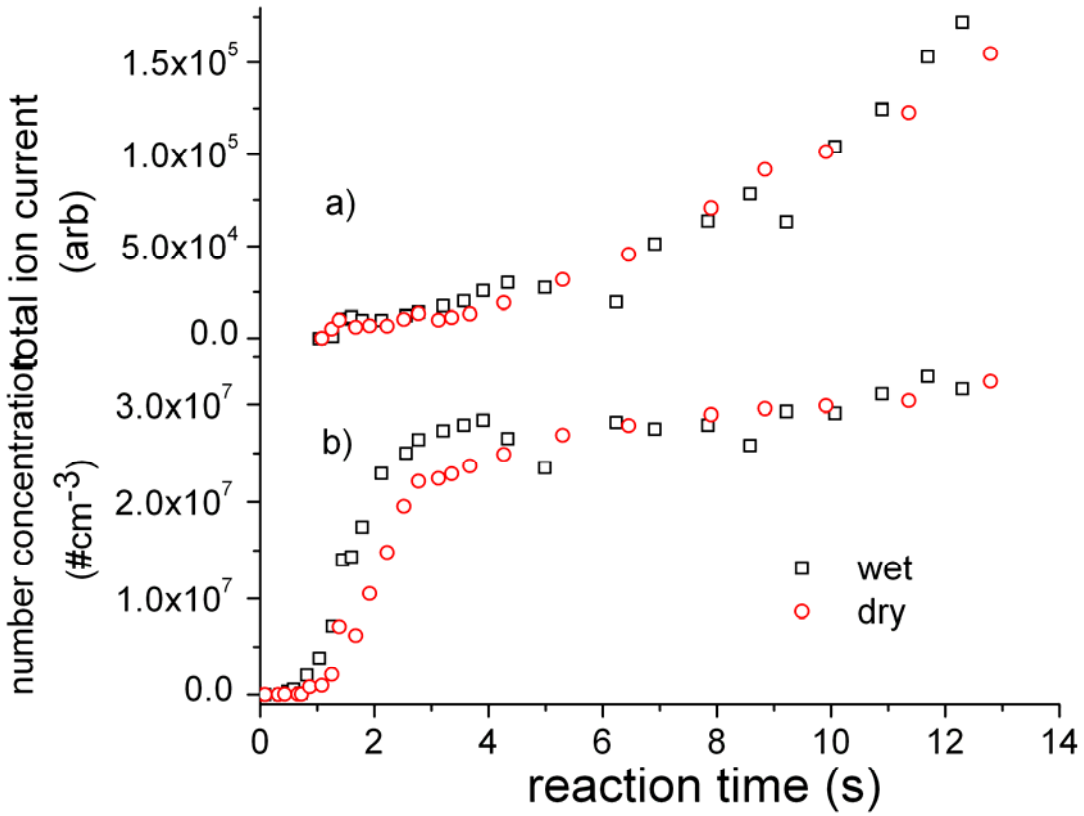

Figure 3.9. Total ion current as a function of reaction time; (□)wet RH < 5 % (○) dry RH ~ 45 %.

Once nucleation has occurred, the pathways that lead to aerosol mass accumulation are likely more numerous. It is somewhat more straightforward to obtain compositional and mechanistic information about the bulk aerosol on a longer timescale because particles have grown substantially in size. As mentioned previously, acids and aldehydes such as *cis*-pinonic acid and pinonaldehyde have been suspected of participating in new particle formation through either the hydroperoxide channel [23,29,32,33] or through the SCI channel.[13,24,30,31] In order to investigate potential pathways to aerosol formation, the spectra of bulk aerosol (t_{rxn} ~10s) were analyzed (Figure 3.3) and fragmentation patterns were investigated.

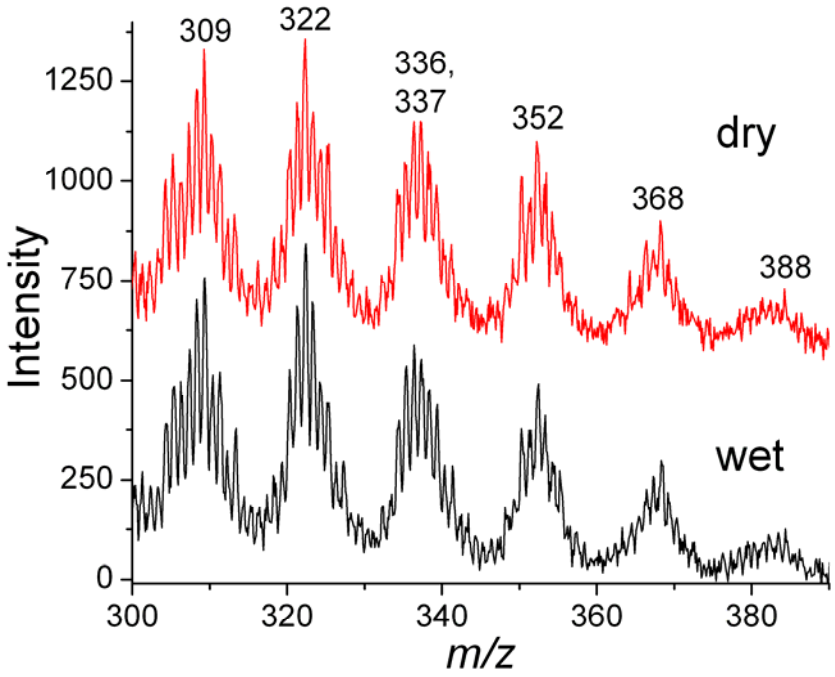

Figure 3.10. VUV-AMS of a-pinene ozonolysis under all of the same experimental conditions except RH. Most of the ions detected are strikingly similar; however, there are discrete differences in the relative intensities of some peaks.

The presence of high intensity odd *m/z* ions not only suggests that fragmentation occurs in the ionization step, but also that a large fraction of the SOA product mass represented in the low mass region is not comprised of organic acids. Organic acids are expected to fragment to form even mass fragments as in the cases of the two standards, *cis*-pinonic acid (*m/z* 166, 114, 98) and pinic acid (*m/z* 168, 140, 114, 100). On the other hand, aldehyde species are known to fragment into predominantly odd *m/z* ions upon ionization.[42] Two examples of aldehydes resulting from α-pinene ozonolysis, pinonaldehyde MW 168 g mol^{-1}, which dissociates into ions with *m/z* 55, 69, 83, 97, 98, 109, 125, and 153, and 10-hydroxy-pinonaldehyde MW 184g mol^{-1} which fragments into ions with *m/z* 55, 69, 83, 97, 109, 125, 153, and 169.[52] The dominant odd *m/z* ions suggest that the majority of the products of this reaction, especially those below *m/z* 200, most likely correspond to products

other than acids. Similar results were found in a comparable experiment preformed by Johnston and co-workers, who proposed this as evidence for secondary ozonide formation involving aldehydes.[30]

Although aldehydes are usually abundant, the ones produced in the featured reaction should not appear in the MS due to their high volatility. Pinonaldehyde, the largest aldehyde formed in α-pinene ozonolysis, has a high vapor pressure and is only expected to be in the gas-phase.[13] On the other hand, it is feasible that aldehydes undergo reactions leading to lower volatility adducts, for example R1b [13,24,30] R4,[27] and R5.[23,29]

In light of these three possibilities, we analyzed our spectra for clues to what products were formed. Reactions of SCI with aldehydes have formed secondary ozonides,[32] and SCI-pinonaldehyde has been suggested by Kamens and co-workers [13,24] to be a potential nucleating agent (R1b) MW = 352. Considering the aldehydes available for reaction with SCI, pinonaldehyde would likely be the only candidate capable of forming a secondary ozonide with low enough volatility to be present in the particle phase. We do observe a rather prominent ion peak at *m/z* 352 as well as fragments expected from ring cleavage (*m/z* 168 and 184). However, we do not observe other prominent ion peaks expected from this secondary ozonide,[32] which would be loss of OH (*m/z* 335), and loss of HO_2 (*m/z* 319). We base our PI fragmentation pattern predictions on EI spectra[32] as fragmentation patterns of both processes are similar. Without knowing the precise fragmentation pattern of this secondary ozonide in our instrument and without higher mass resolution to distinguish isobars, we cannot definitely rule out the presence of secondary ozonides from reaction R1b. It is evident, however, that this ozonide is not a principle component of the SOA.

Secondly, investigation of SCI addition to acidic species such as *cis*-pinonic acid and norpinonic acid is considered. The *cis*-pinonic acid-SCI adduct has been suggested as a likely nucleating agent based on its predicted vapor pressure, which is two orders of magnitude lower than the pinonaldehyde-SCI adduct.[13] In addition, the SCI-*cis*-pinonic acid product would yield a product with MW 368 g mol^{-1}, and expected fragments[32] at *m/z* 201, 185, and 167, all of which are prominent ions in the product spectra (Figure 3.3). The addition of H_2O scavenges SCI and shuts off other reactions involving the SCI (R1a). The necessary concentration of H_2O to sequester > 95 % of the SCI was determined by a method suggested by Ziemann et al.[29]. The ratio of reaction rates of SCI with the scavenger relative to a competing reactant (R_{SCI}) are described by the following equation:

$$R_{SCI} = \frac{k_{SCI,S}[S]}{k_{SCI,C}[C]}$$

where $k_{SCI,S}/\ k_{SCI,C}$ represents the rate-constant ratio for reactions between SCI and the scavenger, S, relative to the competing reactant, C. Values for $k_{SCI,S}/\ k_{SCI,C}$ were assumed to be the same as in the reaction of C13-SCI formed from 1-tetradecene ozonolysis. The two principle competing reactants for reaction with SCI are likely pinonaldehyde and *cis*-pinonic acid, whose yields have been measured to be between 6-51%[10,15,53-55] and ~2-3%,[15,29] respectively. The ratio of concentrations [S]/[C] is determined by measurement or yield prediction and is approximately 10^4 in both cases. Assuming that $k_{SCI,S}/\ k_{SCI,C}$ = 1/2700 for pinonaldehyde (which is the ratio for C13-SCI reactions with water/formaldehyde)[56] and is 1/17000 (which is the ratio for C13-SCI reactions with water/heptanoic acid),[56] then $R_{SCI} \sim 4$ for pinonaldehyde and ~10 for *cis*-pinonic acid. This result indicates that reaction between SCI and H_2O is four and ten times faster than reaction between the SCI and aldehyde or acid, respectively. Under typical atmospheric conditions, SCI and H_2O form α- hydroperoxy

alcohol that will rapidly decompose into H_2O_2 and pinonaldehyde (R1a).[19,57-59] Thus more pinonaldehyde should be produced under 45% RH humidity conditions. Under dry conditions, the concentration of H_2O is no longer high enough to counterbalance the much higher reaction rates between SCI-aldehydes and SCI-acids. Our experimental results show that after longer reaction times (< 4 s), the composition of the wet and dry reaction are equivalent in the high *m/z* region that would presumably contain the crucial low volatility species (Figure 3.10). This implies that after reaction times > 4 s and under anhydrous conditions, the chemical composition of the aerosol particles was identical; no new secondary ozonides or SCI-adducts were formed. At longer timescales, the amount of aerosol produced under both RH conditions was equivalent as measured by total ion current with the aerosol MS (Figure 3.9a) and comparable as measured by the SMPS system (Figure 3.9b). In combination with the unchanging compositional data, this result most importantly indicates that the SCI channel does not affect the bulk composition or SOA yield.

Numerous other laboratories have studied the effect of changing RH on aerosol composition and yield of α-pinene ozonolysis,[13,31,39,49,60,61] however, the literature remains inconclusive. Among researchers who have determined that RH decreases particle number formation, some have found an increase whereas others have found no change in SOA mass formation.[13,31] Others have found no effect of RH on either particle or mass formation.[29,60] Most of these experiments were either gas-phase measurements or particle detection by an SMPS. The only other laboratory to examine real-time particle phase composition as a function of RH, as presented here, has been Ziemann et al.[29] who analyzed aerosol from a reaction chamber. Their results are consistent with ours in that after nucleation, there is no effect of RH on the SOA mass. We find that water does not affect composition or SOA

mass, likely indicating that the hydroperoxide rather than the SCI channel is more operative in producing the SOA mass. Water's participation in α-pinene ozonolysis is only crucial in the beginning of the reaction where it facilitates clustering.

3.3.1.4. OH radical scavenger experiments

Although water scavenges the SCI biradicals, it does not react with other radicals such as the OH radical. On the other hand, isopropanol is effective in scavenging both of these free radicals. It has been shown that the yield of OH radicals in the α-pinene ozonolysis is 85%,[62-65] which means that the oxidation of α-pinene by OH radicals is almost as significant as oxidation of α-pinene by O_3. The OH radical reacts with α-pinene with a rate constant of $55*10^{-12}$ cm^3 $molecule^{-1}$ s^{-1},[66] whereas its rate constant with isopropanol is $5.2*10^{-12}$ cm^3 $molecule^{-1}$ s^{-1}.[67] At the concentration of isopropanol used in our experiment, which is in a 100 fold excess over α-pinene, we expect that 99% of the OH radicals will be scavenged.

Removing the SCI and OH radicals from reacting further results in no significant change in aerosol production (Table 3.2) and the mass spectra are similar to the non-scavenged spectra, except in the region around *m/z* 200. As shown in Figure 3.11, the *m/z* 211 ion peak, which Ziemann{Docherty, 2005 #1363} has attributed to the α-isopropoxy peroxyhemiketal molecule that dissociatively photoionizes from *m/z* 244 to 211 via $HO_2^{\bullet}$ loss, becomes more prominent.

Isopropanol (Scavenger)(ppm)	M_{Dp} (nm)	Mass conc ($\mu g\ m^{-3}$)
0	48.6 ± 2.58	3007 ± 578
100	54.8 ± 0.26	3610 ± 26
400	58.4 ± 0.57	2521 ± 397
1000	64.4 ± 0.26	2672 ± 102
1116	65.0	3110
4000	76.2 + 6.25	5590 + 1526
10000	80.25 +0.07	6910 + 57

Table 3.2. Other conditions: RH < 5 %, [α-pinene] = 39 ppm, $[O_3]$ = 2.682 ppm

Loss of HO_2 yields *m/z* 211, the exact pattern seen in the same reaction by Docherty et al.,[29] formed by reaction of isopropanol and SCI. Although this product is likely to have a low volatility and thus to reside in the particle phase, increasing isopropanol concentration from 0 -10^3 ppm does not result in significant SOA mass change. Clearly, the products made from SCI-isopropanol reaction are not responsible for aerosol formation, as aerosol mass is unchanged (Table 3.2). Due to the characteristic fragility of α-isopropoxy peroxyhemiketal (absence of molecular ion), it is probable that this molecule decomposes instead of reacting further.

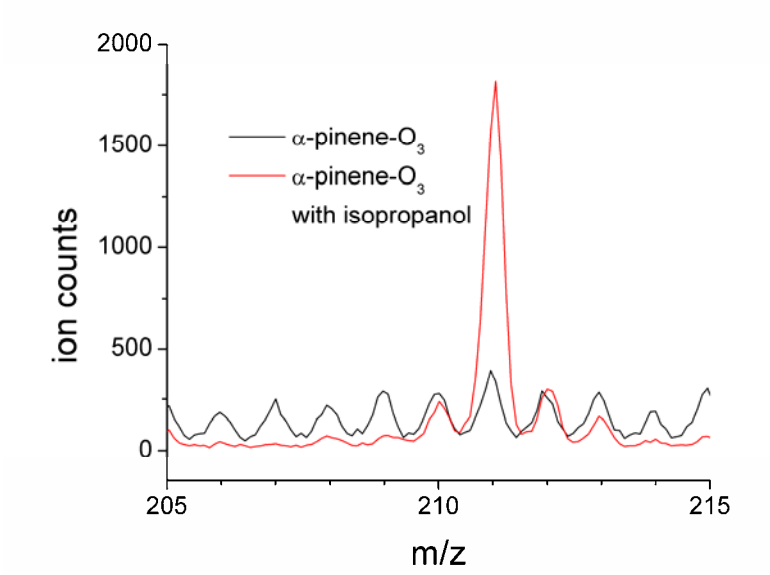

Figure 3.11. Appearance of m/z 211, denotes product formation of α-isopropoxy peroxyhemiketal.

The addition of OH radical scavenger alters the products of the hydroperoxide channel. As suggested by experimental[15,29] and detailed modeling predictions by Jenkin,[23] it appears here that there is a slight change in product formation due to OH radical scavenging thus altering the $[HO_2]/[RO_2]$. In the high mass range, several new peaks separated by 18 mass units appear; *m/z* 328, 346, 364, and 382. The pattern may indicate the presence of alcohols, which typically loose water and can originate from either the SCI of the hydroperoxide channel. Consistent with the $[HO_2]/[RO_2]$ theory, hydroperoxide formation, hence peroxyhemiacetal formation, is apparently enhanced when OH radical scavenger is added to the system. Although this shifting ratio has been predicted, direct evidence has not previously been observed. This delicate SOA analysis technique may give unique perspectives on discrete variations of the high mass peaks that were not successfully detected previously. Changing $[HO_2]/[RO_2]$ has a modest effect on the reaction products as they do not seem to change drastically as the conditions are changed. This issue is somewhat

complicated by the contribution of different molecules that fragment similarly and thus are detected at the same *m/z*.

This chemical modeling study of Jenkin{Jenkin, 2004 #1525} utilized vapor pressure estimations of ~200 probable reaction products to predict aerosol mass yield. However, it was determined that these product species alone could not account for the large amounts of aerosol mass produced.[23] The study suggests the significance of heterogeneous reactions in the aerosol phase, likely involving reactions between carbonyls and hydroperoxides. Products of these reactions were expected to be composed of a variety of involatile and multifunctional peroxyhemiacetals with masses in the 350-400 *m/z* range. It is unclear how many of these peroxyhemiacetals would persist on the timescale of our experiment due to the possibility that the large molecules may decompose into their precursor carbonyl and hydroperoxides. Furthermore, Baeyer Villiger oxidations (Scheme 3.2), which convert an aldehyde to an acid or a ketone to an ester, are potentially operational.

Until recently, larger *m/z* ions in the 300-400 range have not been detected with techniques other than MALDI and ESI. Johnston and co-workers[30] recently detected ions in the same *m/z* range with PIAMS, although not at the high intensity made possible with the VUV-AMS. The highest intensity ions in the high *m/z* range using PIAMS were *m/z* 310,324, 338, 352, 366, 380, and 394, while the most intense peaks detected with VUV-AMS under the same conditions (low RH, no OH scavenger) were *m/z* 322, 337, 352, 368, 384, 390, 392, 394, 398, 400 and 402. Nine of these are previously unreported. An interesting difference in the two spectra (PIAMS and VUV-AMS) is that PIAMS spectra show 14 *m/z* units separation between clumps for the entire mass range, whereas ours are separated by 16 *m/z* units in the high mass range and 14 *m/z* units in the low *m/z*. Separation of 16 *m/z* cannot

occur in the ionization process, meaning that the variety of high *m/z* peaks that we detect is probably due to different amounts of oxygenation or due to addition of H_2O_2 followed by water loss. This speculation could be verified by using a higher resolution analysis method such as an orthogonal RETOF or by MS-MS.

3.4. Summary and conclusions

Conservative estimates from these data suggest that at least 100 products are formed in the ozonolysis of a-pinene. Formation of this complex array of products occurs on a very short timescale. Changes in the relative compositions of molecules during the first few seconds of reaction suggest a mechanism that is initiated with larger MW species. The particles appear to rapidly incorporate smaller species into condensed phase, possibly indicative of condensed phase association reactions between the various partitioning products, generating species in the ~300 > *m/z* > 400 range. For example, association reactions of carbonyls can produce dimer species or heterogeneous uptake of small oxygenated MW species can form large molecular mass species. In addition, carbonyl addition reactions of hydroperoxides may occur to form the corresponding peroxyhemiacetals.

Introduction of elevated levels of water vapor appears to decrease the induction time for particle nucleation to occur. A linear SCI adduct capped with water or H_2O_2 is a potential nucleation precursor. Although the SCI channel may be responsible for producing nucleation species, it is reasonable that the majority of SOA mass is produced by a variety of mechanisms and not principally through the SCI channel considering high number of compounds produced. Our compositional results are consistent with modeling and

experimental results on the a-pinene $–O_3$ system that predict hydroperoxides and peroxides to be a significant component of SOA mass from a-pinene ozonolysis. Although enhancing RH does have a discrete effect on initial particle formation, there are no compositional changes in the particles once they are mature enough to detect, nor are there differences in the total SOA mass produced. In addition, secondary ozonides and SCI adducts, which may well be important in a-pinene ozonolysis particle formation, do not appear to contribute to SOA mass.

The effects of increasing OH scavenger (isopropanol) concentrations suggest that the hydroperoxide channel may be more operative in SOA mass production, and in addition, appears to slightly alter the $[HO_2]/[RO_2]$. These results are consistent with modeling and experimental results on the α-pinene ozonolysis system, stating that hydroperoxides and peroxides are major components of SOA from a-pinene ozonolysis.[23,29] Observable high mass species in the 300-400 *m/z* range are likely to be highly unstable peroxyhemiacetals resulting from heterogeneous reactions of a variety of multifunctional carbonyls and hydroperoxides. Such peroxyhemiacetals are typically present in equilibrium with their precursor molecules and can potentially reversibly dissociate into their original species. Alternatively, these peroxyhemiacetals can undergo Baeyer Villager type rearrangements resulting in an alcohol and ester (from ketones) and a carboxylic acid and alcohol (from aldehydes). Regardless of the pathway to dissociation, these subsequent transformations would result in ion peaks in the $\sim 100 > m/z > 200$ range. This *m/z* range in the present study is characterized not only by its combination of even and odd ions, but also by its large relative peak intensity. Below this range the intensity drops off precipitously, indicating that dissociation of 300-400 *m/z* molecules into smaller species is expected to occur through a

combination of dissociative ionization and decomposition of peroxyhemiacetals in particle phase. Finally, it is evident that the mechanism that initiates particle nucleation is not the same or only mechanism responsible for SOA accumulation and mass growth.

REFERENCES

1. Singh, H. B.; Salas, L.; Viezee, W.; Sitton, B.; Ferek, R. *Atmospheric Environment, Part A: General Topics* **1992**, *26A*, 2929-2946.

2. Guenther, A.; Hewitt, C. N.; Erickson, D.; Fall, R.; Geron, C.; Graedel, T.; Harley, P.; Klinger, L.; Lerdau, M.; et al. *Journal of Geophysical Research, [Atmospheres]* **1995**, *100*, 8873-8892.

3. Griffin, R. J.; Cocker, D. R., III; Seinfeld, J. H.; Dabdub, D. *Geophysical Research Letters* **1999**, *26*, 2721-2724.

4. Guenther, A.; Zimmerman, P.; Wildermuth, M. *Atmospheric Environment* **1994**, *28*, 1197-1210.

5. Kanakidou, M.; Tsigaridis, K.; Dentener, F. J.; Crutzen, P. J. *Journal of Geophysical Research, [Atmospheres]* **2000**, *105*, 9243-9254.

6. Atkinson, R.; Arey, J. *Atmospheric Environment* **2003**, *37*, S197-S219.

7. Atkinson, R. *J. Phys. Chem. Ref. Data* **1997**, *26*, 215-290.

8. Larsen, B. R.; Di Bella, D.; Glasius, M.; Winterhalter, R.; Jensen, N. R.; Hjorth, J. *Journal of Atmospheric Chemistry* **2001**, *38*, 231-276.

9. Fuentes JD, L. M., Atkinson R, Baldocchi D, Bottenheim JW, Ciccioli P, Lamb B, Geron C, Gu L, Guenther A, Sharkey TD, Stockwell W *Bulletin of the American Meteorological Society* **2000**, *81*, 1537-1575.

10. Hatakeyama, S.; Izumi, K.; Fukuyama, T.; Akimoto, H. *Journal of Geophysical Research* **1989**, *94*, 13013-13024.

11. Hakola, H.; Arey, J.; Aschmann, S. M.; Atkinson, R. *Journal of Atmospheric Chemistry* **1994**, *18*, 75-102.

12. Christoffersen, T. S.; Hjorth, J.; Horie, O.; Jensen, N. R.; Kotzias, D.; Molander, L. L.; Neeb, P.; Ruppert, L.; Winterhalter, R.; Virkkula, A.; Wirtz, K.; Larsen, B. R. *Atmospheric Environment* **1998**, *32*, 1657-1661.

13. Lee, S.; Kamens, R. M. *Atmospheric Environment* **2005**, *39*, 6822-6832.

14. Jang, M.; Kamens, R. M. *Atmospheric Environment* **1999**, *33*, 459-474.

15. Yu, J.; Cocker, D. R., III; Griffin, R. J.; Flagan, R. C.; Seinfeld, J. H. *Journal of Atmospheric Chemistry* **1999**, *34*, 207-258.

16. Jaoui, M.; Kamens, R. M. *Journal of Atmospheric Chemistry* **2003**, *44*, 259-297.

17. Koch, S.; Winterhalter, R.; Uherek, E.; Kolloff, A.; Neeb, P.; Moortgat, G. K. *Atmospheric Environment* **2000**, *34*, 4031-4042.

18. Winterhalter, R.; Van Dingenen, R.; Larsen, B. R.; Jensen, N. R.; Hjorth, J. *Atmos. Chem. Phys. Discuss.* **2003**, *3*, 1-39.

19. Winterhalter, R.; Neeb, P.; Grossmann, D.; Kolloff, A.; Horie, O.; Moortgat, G. *Journal of Atmospheric Chemistry* **2000**, *35*, 165-197.

20. Dalton Christine, N.; Jaoui, M.; Kamens Richard, M.; Glish Gary, L. *Analytical chemistry* **2005**, *77*, 3156-3163.

21. Kroll, J. H.; Ng, N. L.; Murphy, S. M.; Varutbangkul, V.; Flagan, R. C.; Seinfeld, J. H. *Journal of Geophysical Research, [Atmospheres]* **2005**, *110*, D23207/23201-D23207/23210.

22. Jenkin, M. E.; Shallcross, D. E.; Harvey, J. N. *Atmospheric Environment* **2000**, *34*, 2837-2850.

23. Jenkin, M. E. *Atmospheric Chemistry and Physics* **2004**, *4*, 1741-1757.

24. Kamens, R.; Jang, M.; Chien, C.-J.; Leach, K. *Environmental Science and Technology* **1999**, *33*, 1430-1438.

25. Seinfeld, J. H.; Asher, W. E.; Erdakos, G. B.; Pankow, J. F. *Environmental Science and Technology* **2001**, *35*, 1806-1817.

26. Gao, S.; Keywood, M.; Ng, N. L.; Surratt, J.; Varutbangkul, V.; Bahreini, R.; Flagan, R. C.; Seinfeld, J. H. *Journal of Physical Chemistry A* **2004**, *108*, 10147-10164.

27. Tolocka, M. P.; Jang, M.; Ginter, J. M.; Cox, F. J.; Kamens, R.; Johnston, M. V. *Environmental Science and Technology* **2004**, *38*, 1428-1434.

28. Iinuma, Y.; Boge, O.; Gnauk, T.; Herrmann, H. *Atmospheric Environment* **2004**, *38*, 761-773.

29. Docherty, K. S.; Wu, W.; Lim, Y. B.; Ziemann, P. J. *Environ Sci Technol* **2005**, *39*, 4049-4059.

30. Tolocka, M. P.; Heaton, K. J.; Dreyfus, M. A.; Wang, S.; Zordan, C. A.; Saul, T. D.; Johnston, M. V. *Environ Sci Technol* **2006**, *40*, 1843-1848.

31. Bonn, B.; Schuster, G.; Moortgat, G. K. *Journal of Physical Chemistry A* **2002**, *106*, 2869-2881.

32. Tobias, H. J.; Docherty, K. S.; Beving, D. E.; Ziemann, P. J. *Environmental Science and Technology* **2000**, *34*, 2116-2125.

33. Tobias, H. J.; Ziemann, P. J. *Environmental Science and Technology* **2000**, *34*, 2105-2115.

34. Shu, J.; Wilson, K. R.; Ahmed, M.; Leone, S. R. *Review of Scientific Instruments* **2006**, *77*, 043106/043101-043106/043110.

35. Mysak, E. R.; Wilson, K. R.; Jimenez-Cruz, M.; Ahmed, M.; Baer, T. *Analytical Chemistry* **2005**, *77*, 5953-5960.

36. Oktem, B.; Tolocka, M. P.; Johnston, M. V. *Analytical Chemistry* **2004**, *76*, 253-261.

37. Woods, E.; Smith, G. D.; Dessiarterik, Y.; Baer, T.; Miller, R. E. *Analytical Chemistry* **2001**, *73*, 2317-2322.

38. Nash, D. G.; Liu, X. F.; Mysak, E. R.; Baer, T. *International Journal of Mass Spectrometry* **2005**, *241*, 89-97.

39. Rohr, A. C.; Weschler, C. J.; Koutrakis, P.; Spengler, J. D. *Aerosol Science and Technology* **2003**, *37*, 65-78.

40. Liu, B. Y. H.; Ziemann, P. J.; Kittleson, D. B.; McMurry, P. H. *Aerosol Science and Technology* **1995**, *22*, 293-313.

41. Liu, B. Y. H.; Ziemann, P. J.; Kittleson, D. B.; McMurry, P. H. *Aerosol Science and Technology* **1995**, *22*, 314-324.

42. WebBook, N. C. In, 2005.

43. Jang, M.; Kamens, R. *Environmental Science and Technology* **2001**, *35*, 3626-3639.

44. Liggio, J.; Li, S.-M.; Mclaren, R. *Environ Sci Technol* **2005**, *39*, 1532-1541.

45. Dreyfus, M. A.; Tolocka, M. P.; Dodds, S.; Dykins, J.; Johnston, M. V. *Journal of Physical Chemistry A* **2005**, *109*, 6242-6248.

46. Jang, M.; Czoschke, N. M.; Lee, S.; Kamens, R. M. *Science* **2002**, *298*, 814-817.

47. Czoschke, N. M.; Jang, M.; Kamens, R. M. *Atmospheric Environment* **2003**, *37*, 4287-4299.

48. Grein, F.; Chen, A. C.; Edwards, D.; Crudden, C. M. *J. Org. Chem.* **2006**, *71*, 861-872.

49. Bonn, B.; Moortgat, G. K. *Atmospheric Chemistry and Physics [online computer file]* **2002**, *2*, 183-196.

50. Barton, M.; Ebdon, J. R.; Foster, A. B.; Rimmer, S. *Organic & Biomolecular Chemistry* **2005**, *3*, 1323-1329.

51. Barton, M.; Ebdon John, R.; Foster Andrew, B.; Rimmer, S. *The Journal of Organic Chemistry* **2004**, *69*, 6967.

52. Jang, M.; Carroll, B.; Chandramouli, B.; Kamens, R. M. *Environ Sci Technol* **2003**, *37*, 3828-3837.

53. Baker, J.; Aschmann, S. M.; Arey, J.; Atkinson, R. *International Journal of Chemical Kinetics* **2002**, *34*, 73-85.

54. Ruppert, L.; Becker, K. H.; Noziere, B.; Spittler, M. *Proceedings of EUROTRAC Symposium '98: Transport and Chemical Transformation in the Troposphere, Garmisch-Partenkirchen, Germany, Mar. 23-27, 1998* **1999**, *1*, 63-68.

55. Alvarado, A.; Tuazon, E. C.; Aschmann, S. M.; Atkinson, R.; Arey, J. *Journal of Geophysical Research* **1998**, *103*, 25,541-525,552.

56. Tobias, H. J.; Ziemann, P. J. *Journal of Physical Chemistry A* **2001**, *105*, 6129-6135.

57. Creheut, R.; Anglada, J. M.; Bofill, J. M. *Chem. Eur. J.* **2001**, *7*, 2227-2235.

58. Hasson, A. S.; Chung, M.; Kuwata, K.; Converse, A. D.; Krohn, D.; Paulson, S. E. *Journal of Physical Chemistry A* **2003**, *107*, 6176-6182.

59. Anglada, J. M.; Aplincourt, P.; Bofill, J. M.; Cremer, D. *ChemPhysChem* **2002**, *3*, 215-221.

60. Fick, J.; Pommer, L.; Nilsson, C.; Andersson, B. *Atmospheric Environment* **2003**, *37*, 4087-4096.

61. Cocker III, D. R.; Clegg, S. L.; Flagan, R. C.; Seinfeld, J. H. *Atmospheric Environment* **2001**, *35*, 6049-6072.

62. Siese, M.; Becker, K. H.; Brockmann, K. J.; Geiger, H.; Hofzumahaus, A.; Holland, F.; Mihelcic, D.; Wirtz, K. *Environmental science & technology FIELD Publication Date:2001*, *35*, 4660-4667. FIELD Reference Number: FIELD Journal Code:0213155 FIELD Call Number:.

63. Rickard, A. R.; Johnson, D.; McGill, C. D.; Marston, G. *Journal of Physical Chemistry A* **1999**, *103*, 7656-7664.

64. Chew, A. A.; Atkinson, R. *Journal of Geophysical Research* **1996**, *101*, 28,649-628,653.

65. Atkinson, R.; Aschmann, S. M.; Arey, J.; Shorees, B. *Journal of Geophysical Research, [Atmospheres]* **1992**, *97*, 6065-6073.

66. Atkinson, R.; Aschmann, S. M.; Pitts, J. N., Jr. *International Journal of Chemical Kinetics* **1986**, *18*, 287-299.

67. Yujing, M.; Mellouki, A. *Chemical Physics Letters* **2001**, *333*, 63-68.

CHAPTER 4:
Design of a Timing Circuit for Random Laser Triggering on Aerosol Particles

4.1 Introduction

The timing of laser pulses with respect to one another and/or with respect to pulsed molecular beams is a familiar issue in spectroscopic and dynamical experiments. The overwhelming majority of these experiments operate at fixed frequencies, which are determined by the experimenter and initiated by a pulse generator. However, there are classes of experiments for which the sample arrives at random times, making it necessary to trigger the lasers at irregular intervals.[1-3] This mode of operation presents certain challenges, particularly when using Nd:YAG lasers, an obvious one being associated with the repetition rate. While excimer lasers can be triggered at any frequency up to their maximum, most Nd:YAG lasers can only be triggered at or near their specified frequency, (generally 10 or 30 Hz) so that a constant heat load is maintained on the rods. In addition, excimer, TEA CO_2, and Nd:YAG lasers require trigger pulses approximately 1, 5, and 200 μs prior to the laser output, respectively. Although pre-triggering is straightforward in constant frequency experiments, it is quite challenging for experiments where the laser is fired on random events.

A number of single particle aerosol mass spectrometers designed to analyze randomly arriving particles have been developed.[4-12] The particles are introduced into the mass spectrometer by expansion through a nozzle that accelerates the particles to a

velocity related to their size. Some instruments employ a single continuous wave laser for light scattering close to an excimer laser crossing. Because the excimer laser can be triggered within a microsecond, advanced warning of the aerosol particle arrival is not necessary. This technique is capable of firing on any particle large enough to scatter light, but only rough estimates of particle size can be made from the intensity of the light scattering signal.[4;5] It is also possible to move the light scattering laser some distance away from the ionization region and trigger the ionization laser at a constant time delay from the scattered light signal. Particle size is then limited to those particles having the correct velocity[6] to arrive promptly in the ionization spot.

A more versatile approach employs two light scattering stations, which permits information about the velocity, and therefore aerodynamic size to be stored. This light scattering technique for timing particles was pioneered in 1973 by Dahneke[13] and is currently used by single particle aerosol instruments in the labs of Prather and co-workers [10;14;15] and Baer and co-workers. [11;12;16;17] The particle timing circuit used by Prather et al. consists of two counters, one that is triggered to count up as a particle passes the first light scattering station and one that is triggered to count down as the particle passes the second light scattering station. Their design requires the distance between the two light scattering stations to be twice as long as the distance between the second light scattering station and the laser interaction region to ensure that the Nd:YAG can be triggered 200 μs prior to the particle arriving in the ionization region. However, this approach does not permit the Nd:YAG laser flashlamps to be fired at its specified frequency of 10Hz, and compromises accuracy by increasing the distance between the second light scattering station and the interaction region.

The particular application of the timing circuit described here is to the vaporization and ionization of aerosol particles in order to achieve time-of-flight (TOF) mass analysis. The particles (0.3 – 5 μm in diameter) are focused by an aerodynamic lens system[18;19] and are accelerated to their terminal velocity by expansion through an aperture into vacuum; yielding speeds ranging from approximately 40 - 400 m/s. Particles travel in the vacuum chamber through two continuous diode laser beams separated by 10 cm (see Figure 4.1). The time elapsed between the two light scattering pulses ranges between 250 - 2500 μs. The ionization region is located 10 cm from the second diode laser, thereby providing 250 - 2500 μs to trigger the TEA CO_2 laser used to vaporize the particles, as well as the flashlamps and Q-switch of the Nd:YAG laser used to ionize the resulting vapor plume.

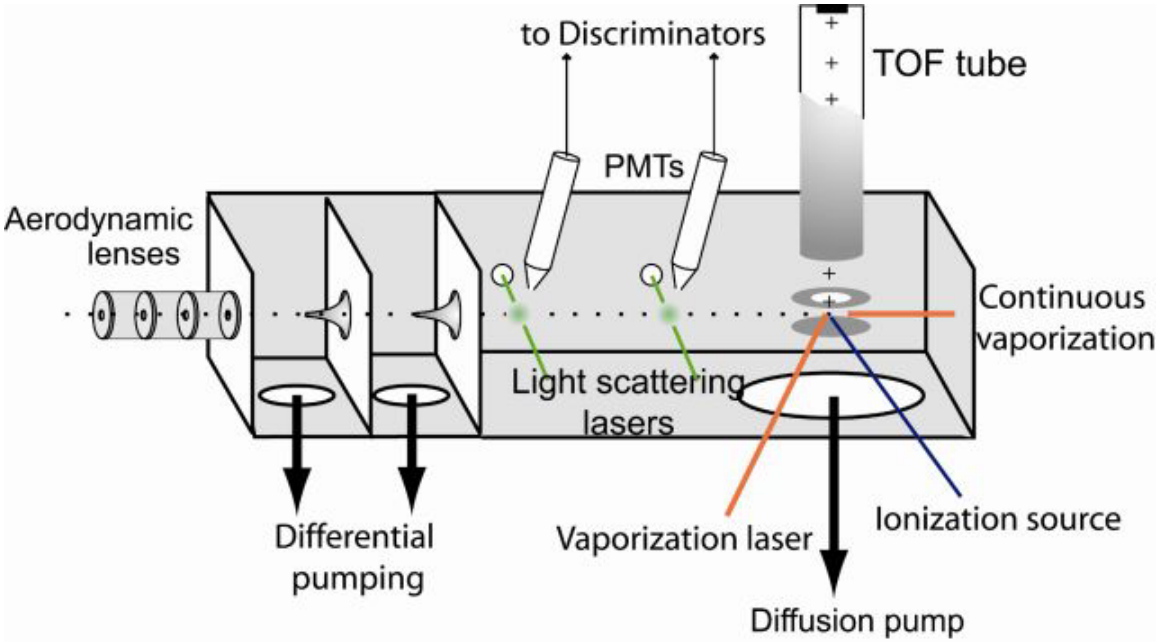

Figure 4.1. A typical single particle aerosol time-of-flight mass spectrometer with light scattering for particle timing.

The aerosol particles can alternatively be vaporized by a heater and the resulting plume ionized by a continuous source, including electron impact or chemical ionization, photoionization using a rare gas resonance lamp, or even synchrotron radiation. In these cases, the timing requirement is not as complex as that discussed for laser evaporation, since neither advanced laser triggering nor steady firing of the laser is required. Nevertheless, if single particle ion mass analysis is carried out by TOF, it is still necessary to extract the ions when they arrive in the ionization region. Consequently, a simplified version of the timing circuit can be used.

4.2 Description of the Circuit

The circuit used in the instrumental set-up including the pulsed lasers is illustrated in a block diagram in Figure 4.2. This circuit is shown in detail in Figure 4.3, and a detailed circuit diagram used for continuous ablation/ionization is found in Figure 4.4. The circuit in Figure 4.3 is more complex because it includes the components that satisfy the triggering requirements of the Nd:YAG laser. For ease of presentation, Figure 4.4 will be used to explain circuit details common to both circuits.

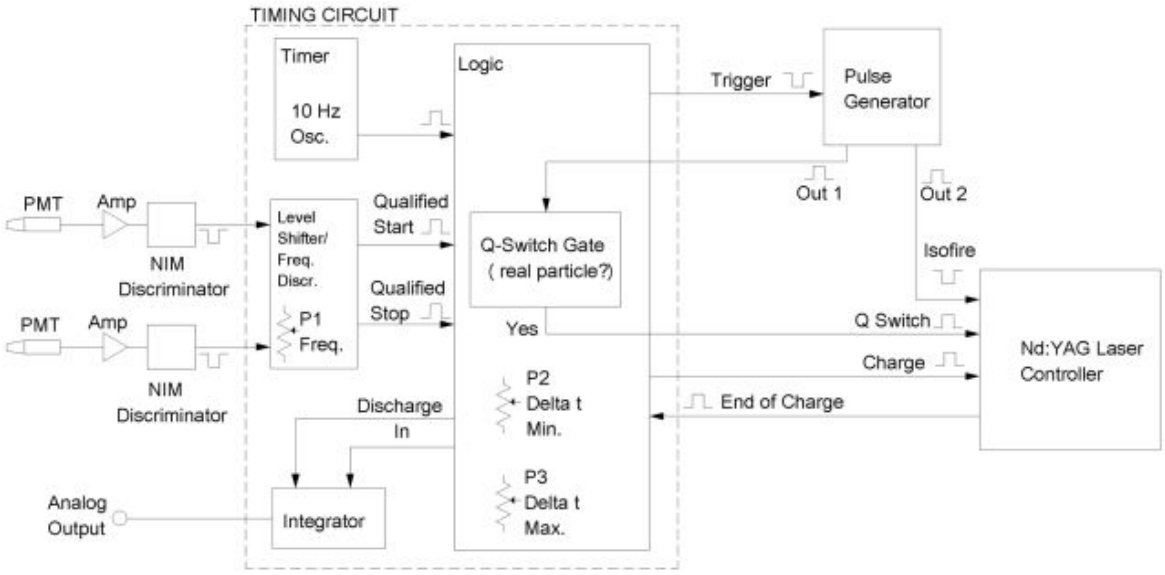

Figure 4.2. Block diagram of particle timing circuit designed to incorporate a Nd:YAG laser into the instrumental set-up.

Once an aerosol particle has reached its terminal velocity, it enters the light scattering region of the instrument (Figure 4.1). As a particle crosses the first light scattering station, the photons are collected by a photomultiplier tube (PMT). The corresponding signal is sent to a discriminator that converts single photon events into a series of negative logic pulses (Figure 4.2). This pulse packet is fed into the timing circuit and serves as the 'start' signal (BNC 1 in Figure 4.4a). Similarly, the signal from the second PMT is sent to input BNC 2. These two sets of negative pulses are sent through a pulse-frequency discriminator, which is designed to accept these inputs if their frequency exceeds the acceptable level set by P_1 (Figures 4.2 and 4.4a). This frequency threshold is typically 2MHz averaged over 2 μs, i.e. at least four pulses in 2 μs. If the incoming signals have a photon frequency above threshold, the pulses are converted into single 5 V pulses and are passed through to the next portion of the timing circuit (Figures 4.2 and 4.4b).

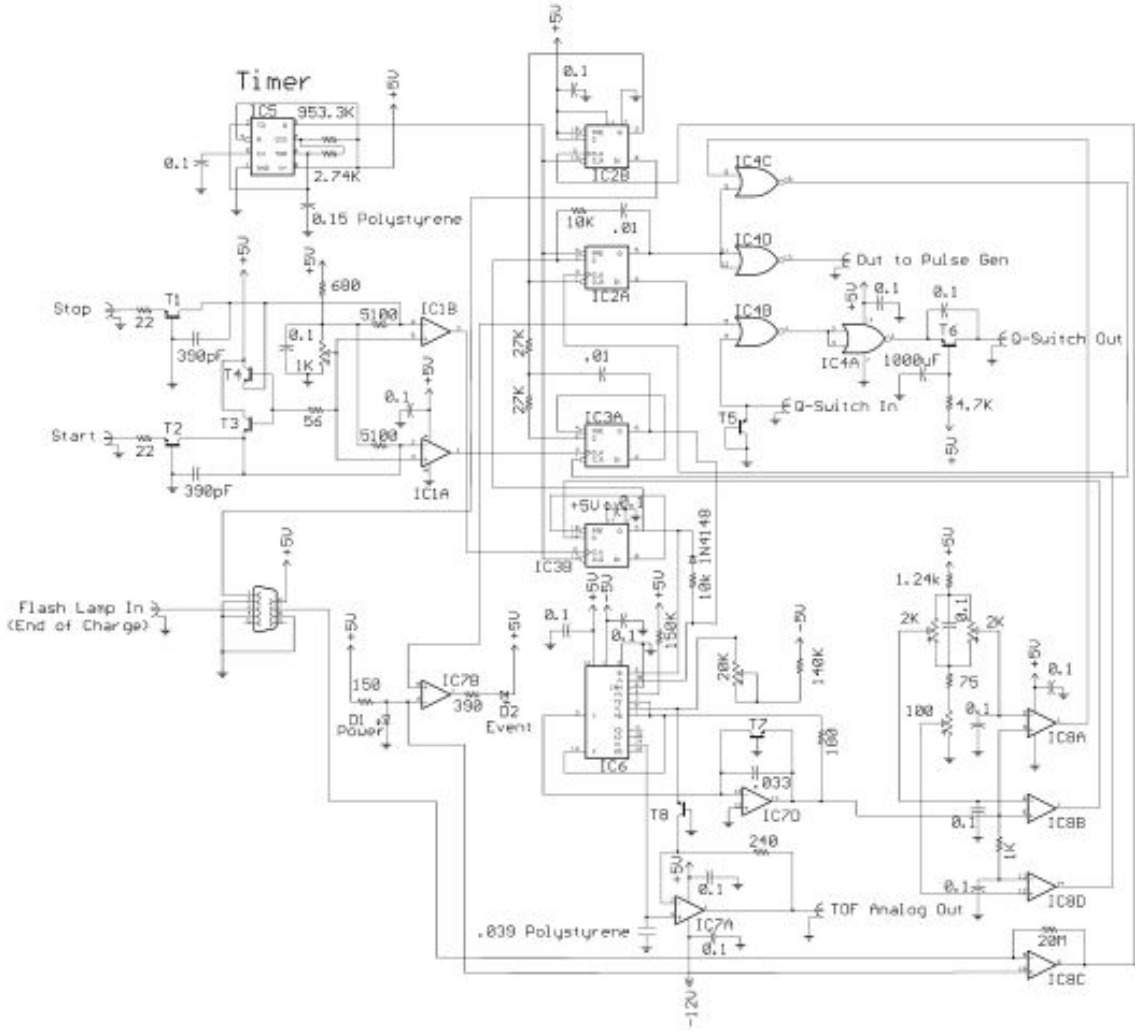

Figure 4.3. Particle timing circuit for instrumental set-up requiring use of a Nd:YAG laser.

SYMBOL	CHIP
T1,T2	2N2369
T3-T8	2N4401
IC1	MAX907CPA
IC2,IC3	74HC74
IC4	74HCT02
IC5	LM555N
IC6	74HCT4052
IC7	LT1058
IC8	MAX908

Table 4.1. Component key for Figure 4.3.

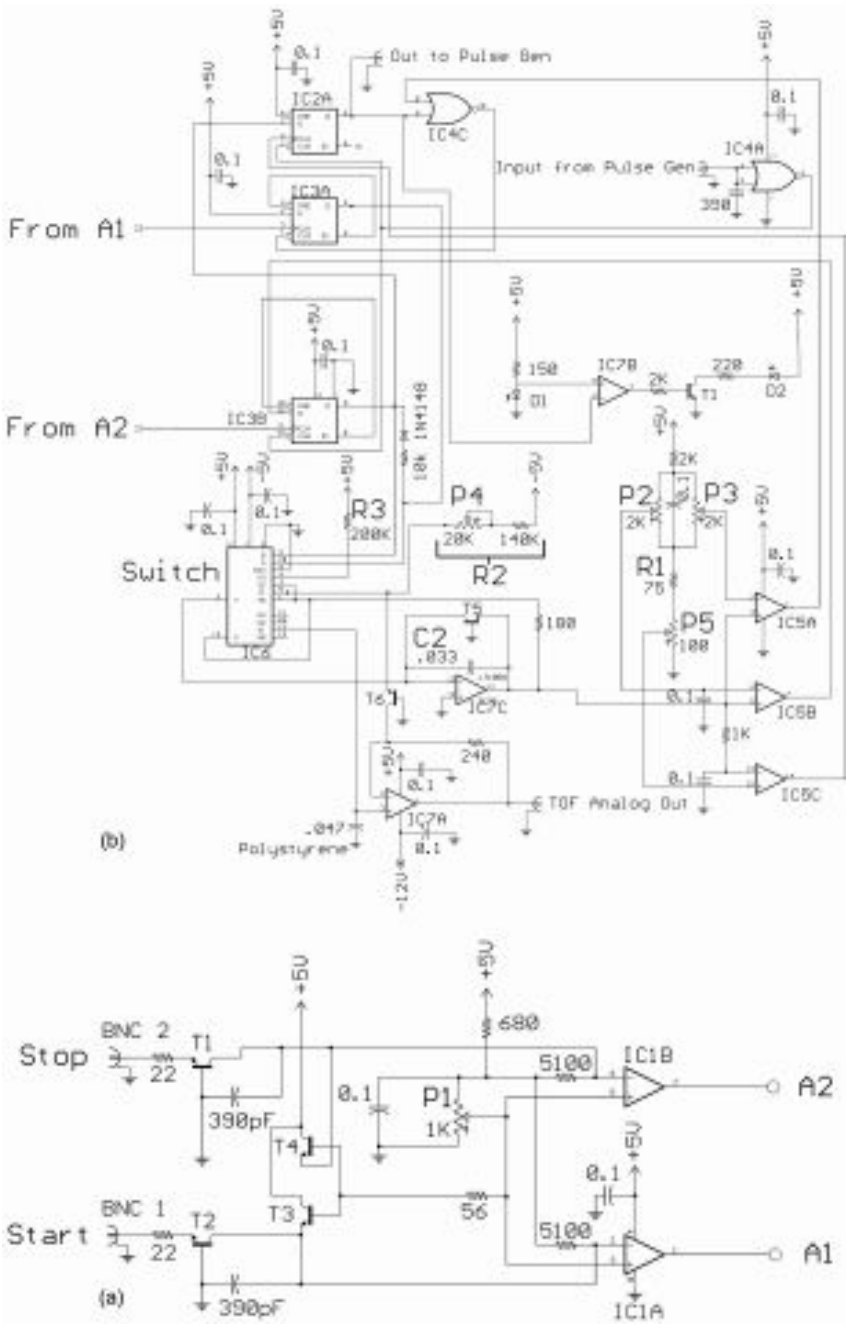

Figure 4.4a. Preamplifier for the particle light scattering signals. Acceptable inputs for start and stop signals are converted into two single 5 V pulses. **Figure 4.4b.** Particle timing circuit used in an apparatus employing continuous vaporization and ionization sources.

SYMBOL	CHIP
T1,T2	2N2369
T3,T4	2N4401
IC1	MAX907CPA

Table 4.2. Component key for Figure 4.4a.

SYMBOL	CHIP
IC2,IC3	74HC74
IC4	74HCT02
IC5	MAX908
IC6	74HCT4052
T5,T6	2N4401
T9	2N2222
IC7	LT1058
D1	U57X32
D2	CMD264

Table 4.3. Component key for Figure 4.4b.

Figure 4.5 shows a timing profile for a particle passing through both light scattering stations. The timing circuit will accept any pair of start/stop input pulses if $t_A = (t_1 - t_0)$ falls within a preset time window, Δt, as illustrated in Figure 4.5. Δt is determined by two sets of maximum and minimum controls, one internal and one external. The internal control, which is a voltage divider indicated by R_1 (Figure 4.4b), determines the absolute maximum and minimum values of the acceptable particle travel time between the two light scattering stations, which in our set-up is 250 - 2500 μs. The external control of Δt, determined by potentiometers P_2 and P_3 (Figures 4.2 and 4.4b), allows the user to set Δt to any value within the internal maximum and minimum values. Changing Δt permits selection of particles in a particular range of velocities and, therefore, sizes.

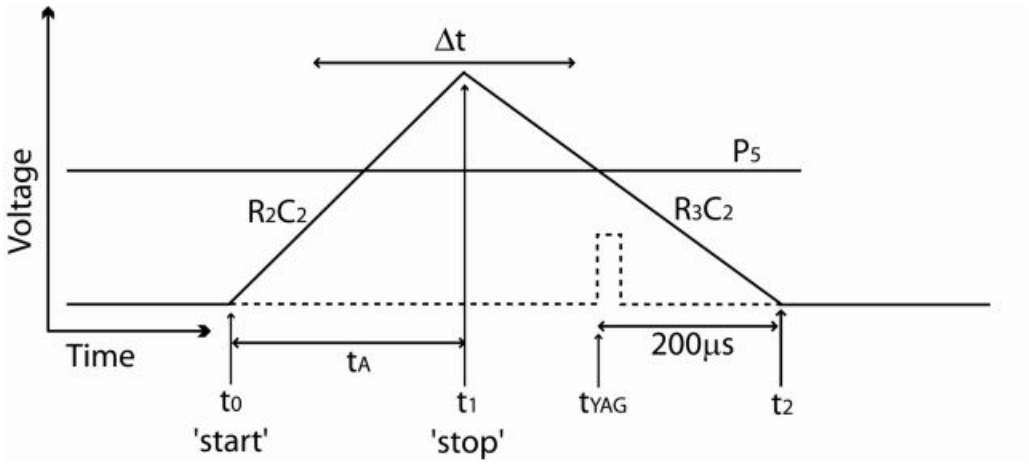

Figure 4.5. Voltage versus time profile for charging and discharging of capacitor C_2. Charging and discharging of C_2 is controlled by two light scattering signals; charging begins when a particle passes the first light scattering station at t_0, and discharging begins as it passes the second light scattering station at t_1. The particle velocity is determined by t_A, which is used to calculate t_2, the particle's arrival time in the ionization region. At t_{YAG}, 200 μs before t_2, the flashlamps of the Nd:YAG laser are triggered so that they will have a maximum output when the Q-switch is fired at t_2. A particle within the acceptable TOF range has a t_1 within Δt.

In the case that the stop pulse, t_1, does not occur within the pre-set Δt, the unit waits to detect the next pair of input pulses. If the stop pulse is within the acceptable Δt, and if no previous pair of acceptable pulses arrived within the previous 100 ms (to maintain no more than 10 laser shots per second), the timing unit sends the appropriate outputs to the various lasers.

One of the challenges of coupling the Nd:YAG laser to random particle sampling is the flashlamp firing frequency requirement. The fixed frequency allows the flashlamp rods to maintain a constant temperature, thereby ensuring shot-to-shot consistency. A 10 Hz (τ = 100 ms) timer inside the circuit serves as a clock (Timer in Figures 4.2 and 4.3) that ensures that the flashlamps fire, on average, at their required frequency. This internal clock's time constant is set to meet the needs of a specific laser at the time of circuit construction. Every 100 ms, a new Nd:YAG flashlamp firing cycle begins as the clock triggers the flashlamp capacitors to charge. When they are fully charged, the

Nd:YAG laser sends an end-of-charge signal back to the particle timing circuit through a 9-pin connector. When this end-of-charge signal is received, the circuit begins to accept particle input signals.

In the absence of particles, the clock triggers the flashlamps at a constant 10 Hz. However, because the Q-switch in the Nd:YAG laser does not have a fixed firing frequency requirement, the Q-switch is not fired unless it is triggered on a particle. Q-switch suppression is achieved by using a gate inside the circuit (Figure 4.2). Each time the flashlamps are fired, a pulse is sent to the Q-switch gate element; however, the signal will only propagate through to fire the Q-switch if the flashlamps are fired on a real particle event.

The laser is triggered if a particle is detected in the light scattering region before the laser clock timeout (100 ms) and after the Nd:YAG flashlamps capacitors have finished charging. To ensure that the laser fires at the correct time, the timing unit calculates t_2, the particle's arrival time in the ionization region (Figure 4.5). This is done by sending the 5 V start pulse to a switch (Switch in Figure 4.4b) that begins charging a capacitor, C_2 (Figure 4.4b), with time constant R_2C_2 beginning at t_0 (Figure 4.5). When an acceptable 'stop' signal is detected, the same capacitor is discharged through use of the switch with time constant R_3C_2 beginning at t_1. The time constants R_2C_2 and R_3C_2 are chosen at the time of circuit construction to correspond to the ratio of the distances between the two light scattering stations and between the second light scattering station and the ionization region. These distances have a ratio of 3:4 in the instrumental set-up of the circuit in Figure 4.4. The circuit uses the same capacitor for both charging and discharging processes, so that the resistors in our case are $4R_2 \approx 3R_3$. A potentiometer P_4

is used as part of R_2 so that fine adjustment can be made to account for uncertainty in the two distances. Figure 4.6 shows the voltage versus time profiles for large and small particles. This figure illustrates that for different particle aerodynamic diameters, the time constants determined by R_2C_2 and R_3C_2 remain the same. Nevertheless, t_A, the particle flight time between two scattering stations and t_B, the particle flight time between the second station and the ionization region, do change. However, for all particle sizes, the ratio of t_A/t_B remains constant.

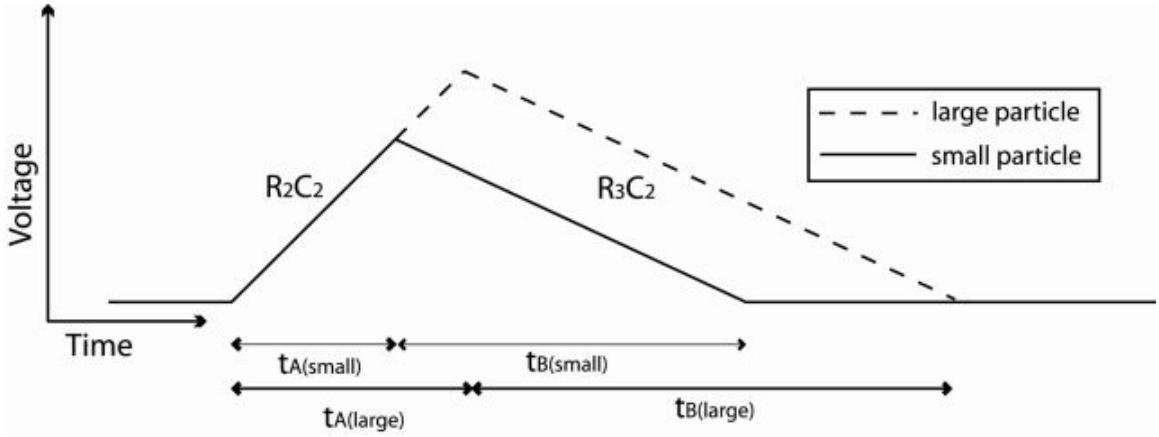

Figure 4.6. Voltage versus time profile for a small versus large particle. $t_{A(small)}$ and $t_{A(large)}$ vary for different sized particles, however, $t_{A(small)}/t_{B(small)} = t_{A(large)}/t_{B(large)}$.

The second major challenge in using a Nd:YAG laser to analyze randomly arriving particles is the pre-triggering requirement. In our set-up, we trigger the Nd:YAG flashlamps at t_{YAG}, which is 200 μs prior to Q-switch firing and laser output at t_2 (Figure 4.5). This delay can be adjusted, and adjustment is necessary if we want to change the power of the laser by offsetting the Q-switch from the maximum flashlamp output voltage, or if another laser (such as an excimer or a CO_2 laser) is used in the instrumental set-up. The internal potentiometer P_5 (Figure 4.4b) is used to regulate this delay.

The circuit sends a pulse out 200 μs prior to t_2 (t_{YAG}) so that the flashlamps can be triggered at an optimal time prior to Q-switch firing. The 200 μs time period is determined by comparing the voltage profile of C_2 (illustrated in Figure 4.5) to a reference voltage set by P_5. The pre-trigger fires when the two voltages being compared are equal. Because the time constant of the discharge of C_2 is independent of particle size, the pre-trigger is always sent 200 μs prior to t_2. At t_{YAG}, the timing unit triggers an external delay generator that sends a delayed (200 μs) pulse back into the timing unit and through its Q-switch gate (Figure 4.2). The Q-switch gate, enabled by detection of an acceptable particle, passes the pulse through to the Nd:YAG Q-switch and causes it to fire. After the Q-switch is fired, the quiescent state of the timing circuit persists until the end of the 100 ms laser clock cycle. This feature blocks particles from being detected by the timing unit before the laser flashlamps are recharged and ready to fire again. This guarantees evenly spaced laser pulses in the limit of high particle counts.

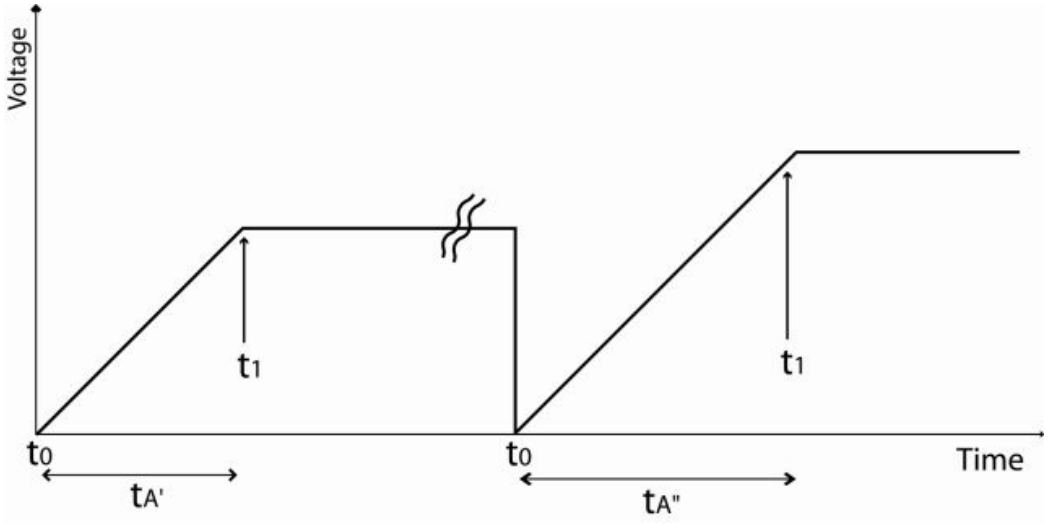

Figure 4.7. Voltage versus time profile for particle time-of-flight (TOF) between two light scattering stations. Particle aerodynamic diameter is proportional to t_A, and is calculated from the voltage value reached after time t_A has passed. Particle TOF between the two stations is less for a smaller particle, thus a smaller voltage is read after $t_{A(small)}$ than for $t_{A(large)}$.

The same switch (Switch in Figure 4.4b) is used within the timing unit to correlate the mass spectrum with the particle TOF between the diode lasers and hence particle aerodynamic diameter. The switch feeds a voltage integrator that outputs an analog voltage, which can be used to determine particle diameter (Figure 4.7). At t_0, a capacitor is grounded and immediately begins to charge until t_1. The final voltage is externally read (Analog Output in Figure 4.2) and converted to particle diameter and is held until the timing circuit detects a new particle and is thus reset.

REFERENCES

1. Bunn, T. L.; Richard, A. M.; Baer, T. *J.Chem.Phys.* **1986,** *84*, 1424-31.

2. Bunn, T. L.; Baer, T. *J.Chem.Phys.* **1986,** *85*, 6361-67.

3. Noble, C. A.; Nordmeyer, T.; Salt, K.; Morrical, B.; Prather, K. A. *Trends Anal. Chem.* **1994,** *13*, 218-22.

4. McKeown, P. J.; Johnston, M. V.; Murphy, D. M. *Anal.Chem.* **1991,** *63*, 2069-73.

5. Murphy, D. M.; Thomson, D. S. *Aerosol Sci.Technol.* **1995,** *22*, 237-49.

6. Hinz, K. P.; Kaufmann, R.; Spengler, B. *Anal.Chem.* **1994,** *66*, 2071-76.

7. Carson, P. G.; Neubauer, K. R.; Johnston, M. V.; Wexler, A. S. *J.Aerosol Sci.* **1995,** *26*, 535-45.

8. Dale, M. J.; Yang, M.; Whitten, W. B.; Ramsey, J. M. *Anal.Chem.* **1994,** *66*, 3431 - 35.

9. Tan, P. V.; Evans, G. J.; Tsai, J.; Owega, S.; Fila, M. S.; Malpica, O. *Environ.Sci.Technol.* **2002,** *36*, 3512-18.

10. Prather, K. A.; Nordmeyer, T.; Salt, K. *Anal.Chem.* **1994,** *66*, 1403-07.

11. Zelenyuk, A.; Cabalo, J.; Baer, T.; Miller, R. E. *Anal.Chem.* **1999,** *71*, 1802-08.

12. Woods III, E.; Smith, G. D.; Dessiaterik, Y.; Baer, T.; Miller, R. E. *Anal.Chem.* **2001,** *73*, 2317-22.

13. Dahneke, B. *Nature, Physical Science* **1973,** *244*, 54-55.

14. Nordmeyer, T.; Prather, K. A. *Anal.Chem.* **1994,** *66*, 3540-42.

15. Gard, E.; Mayer, J. E.; Morrical, B. D.; Dienes, T.; Fergenson, D. P.; Prather, K. A. *Anal.Chem.* **1997,** *69*, 4083-91.

16. Woods III, E.; Smith, G. D.; Miller, R. E.; Baer, T. *Anal.Chem.* **2002,** *74*, 1642-49.

17. Woods III, E.; Miller, R. E.; Baer, T. *J.Phys.Chem.A* **2003,** *107*, 2119-25.

18. Liu, P.; Ziemann, P. J.; Kittelson, D. B.; McMurry, P. H. *Aerosol Sci.Technol.* **1995,** *22*, 314-24.

19. Liu, P.; Ziemann, P. J.; Kittelson, D. B.; McMurry, P. H. *Aerosol Sci.Technol.* **1995,** *22*, 293-313.

CHAPTER 5

Conclusions and future directions

Throughout the current research, ultrafine organic aerosols have been examined with a novel instrument that combines gentle thermal vaporization and photoionization. The effects of both vaporization temperature and ionization energy on the fragmentation patterns of various organic species were investigated. The experimental approach combined a cartridge heater with a synchrotron source that provided tunable, coherent, quasi-continuous VUV radiation. Single component as well as multicomponents aerosols were analyzed. Finally, a timing circuit with application to single particle mass spectrometry, was described.

Soft VUV radiation is optimally suited for analyzing delicate organic constituents and is increasingly the focus of several research groups utilizing aerosol mass spectrometry. As evidenced in Chapter 2, the photoionization energy can be tuned just above the ionization energy of organic molecule, thus minimizing complications due to excess fragmentation and, in some cases, producing a fragment free mass spectrum. While photoionization of aerosols by VUV light has been pursued in the laboratory environment for many years, increased recognition of the utility of reduced fragmentation by VUV has spawned current interest in portable VUV sources. One such option is a resonance lamp, which has interchangeable bulbs containing either Ar (11.6 eV), Kr (10.0 and 10.6 eV), or Xe (8.4 eV). Portable rare gas resonance lamps are produced in a compact format (Syagen Inc.) and provide up to 10^{15} photons per second. Previously, we attempted to couple a VUV lamp to our Chapel Hill

instrument, however, the flux of the current design was neither high nor direct enough to produce adequate signal from a low frequency of large particles. Instead, a continuous stream of ultrafine particles was reasoned to be better suited for analysis by a VUV continuous source. In the last two years, researchers working on the commercial electron impact field based instrument, the AMS (Aerodyne), have begun to explore using VUV in combination to their EI source. While neither laboratory nor field data have been reported in the literature to date, it remains an active area of research.

The simplified mass spectral data obtained with a single component aerosol with the VUV-AMS prompted research on the more complex system α-pinene ozonolysis. For these experiments, a flowtube system was designed and constructed so that the reaction could be examined on short timescales during the very early stages of nucleation. Although the sample introduction portion of the instrument prevented sampling of the freshly nucleated species (2-25nm), valuable insights into the reaction were gained. For particles larger than 25 nm, particle growth (with an SMPS) and compositional change (with the VUV-AMS) was monitored as a function of reaction time. It is shown through relative humidity studies that water vapor acids nucleation and that multiple mechanisms are likely responsible for subsequent particle mass growth.

This is the first study to examine on-line time-resolved particle morphology and compositional change of newly formed SOAs. Several possible future studies can be envisioned from this initial SOA work. For example, particles formed in the very initial stages of SOA nucleation are currently out of the detectable size range as particles below 25 nm are not efficiently transmitted through the aerodynamic lens system. However, to circumvent this problem, inert seed particles may be used to act as nucleating surfaces.

For example, a 2 nm coating of α-pinene ozonolysis products coating a 100 nm seed particle would efficiently pass through the aerodynamic lens and into the analysis portion of the MS. It is possible to produce high concentrations of 100nm seed particles with piezo-electric nebulizers, and size select the polydisperse size with a DMA. These high fluxes of 100nm particles would be ideal for analysis with the synchrotron based VUV-AMS. Another noteworthy option is to utilize seed particles that can participate in condensable product formation, such as acidic seeds. Questions that have plagued researchers for a decade concerning the compounds responsible for nucleation and the mechanism of SOA formation may be investigated and potentially identified with soft ionization. Furthermore, our results have demonstrated that in order to interpret the complex product ion distributions formed in SOA reactions, higher resolution MS techniques are necessary. One solution would be to give the gentle photoionization instrument described here MS-MS capabilities or to increase its resolution with an orthogonal RETOF capable of distinguishing between isobars. Lastly, the diverse VUV-AMS instrument coupled to the flowtube apparatus and SMPS system designed and developed in this work can be employed to examine multiple SOA and heterogeneous reactions crucial to understanding atmospheric processes.